HIGH-PRECISION MASS MEASUREMENT OF ^{32}Si AND DEVELOPMENTS AT THE LEBIT FACILITY

By

Anna A. Kwiatkowski

A DISSERTATION

Submitted to
Michigan State University
in partial fulfillment of the requirements
for the degree of

DOCTOR OF PHILOSOPHY

Physics and Astronomy

2011

ABSTRACT

HIGH-PRECISION MASS MEASUREMENT OF ^{32}Si AND DEVELOPMENTS AT THE LEBIT FACILITY

By

Anna A. Kwiatkowski

The mass of an atom, a fundamental property, serves as a unique identifier of the nucleus like a fingerprint and represents, through the binding energy, the sum of all atomic and nuclear interactions. Precise mass values are essential in many disciplines including nuclear structure and fundamental symmetries. The highest precision mass measurements are obtained with Penning trap mass spectrometers; of those, only the Low Energy Beam and Ion Trap (LEBIT) facility has been able to measure rare isotopes produced by projectile fragmentation. In this work, the high precision mass measurement of unstable ^{32}Si, $\delta m/m = 1 \times 10^{-8}$, is presented and found to deviate from the literature value by four standard deviations. The measurement is combined with the mass values for the A = 32, T = 2 quintet to provide the most stringent test of the isobaric multiplet mass equation (IMME) to date. The experimental results indicate a dramatic breakdown of the quadratic form of IMME and require a large cubic term. In addition, the masses of ^{33}Si, ^{31}P, ^{34}P, and ^{32}S were measured, which agree with earlier experimental data.

Beam purity is critical to high-precision Penning trap mass spectrometry. This dissertation documents the development of in-trap cleaning of stored ion samples based on stored waveform inverse Fourier transform (SWIFT). The technique can eliminate isobaric contaminants without the need to identify individual contaminants unlike the method used in the present work. SWIFT cleaning minimizes possible systematic errors in mass determination and will increase LEBIT's measurement efficiency.

For my parents

ACKNOWLEDGMENTS

My advisor, Georg Bollen, has encouraged and assisted me throughout my graduate career. Georg instructed me in the lab, sent me to several conferences and summer schools, and provided many interesting research projects. During my first few years in LEBIT, Stefan Schwarz played a pivotal role in my training, from soldering lessons to data analysis. In the lab, Stefan was my mentor and answered my every question. In the latter years, Ryan Ringle oversaw the recommissioning of LEBIT, pushed forward testing of SWIFT cleaning, and proofed my thesis as quickly as I could write. Josh Savory facilitated my joining of the group; we often spent weeks working side-by-side in the lab. To the rest of the LEBIT team, both past and present, I also express my gratitude. Many thanks to the gas cell team, led by Dave Morrissey who frequently acted as a second advisor to me. I credit the wonderful scientists and staff of the NSCL for enhancing my graduate studies. In particular, Dan Morris deserves recognition for his help in achieving SWIFT beam purification. Dan lent me his spectrum analyzer for extended periods, explained RF mixers, and advised me on many technical aspects.

Rhiannon Meharchand and I co-founded a student group, WaMPS, and her skill sets complemented mine. As our faculty advisor, Filomena Nunes counseled and nurtured the group. From its inception, Wolfgang Bauer and Michael Thoennesson have generously provided financial support from the PA Department and the NSCL respectively. I am gratified to see WaMPS' success and the unexpected popularity of my "little" mentoring program.

I would also like to thank the many friends I have made here. With three in particular, I weathered class work, subject exams, experiments, the highs and lows of research, and graduate student life: Carol Guess, Dan Olds, and Megan Romanowich. Last, I thank my family for unwavering support and constant encouragement.

Contents

List of Tables

List of Figures

Chapter 1

Introduction

In the ideal high precision experiment, the scientist probes a pure sample in an isolated environment with precise tools. While the ideal laboratory has yet to be achieved, ion traps offer nearly ideal conditions: confinement in a small volume, well-controlled electromagnetic fields, long observation times, and single-ion sensitivity. These parameters make it a tool of choice for precision measurements and versatile enough to serve areas of science that range from forensics to nuclear physics.

The most important ion traps are the Paul (or radiofrequency) and Penning traps. The former has been deployed for laser and radiofrequency spectroscopy [1–3], the realization of a frequency standard [2,3], and manipulation of rare isotope beams [4,5]. In the field of mass spectrometry, the precision of Paul traps is limited to $\approx 10^{-6}$ by the stability of the electric field [6]. In comparison, Penning traps are renowned for the high precision achieved in many types of measurements. Even the earliest experiments with a Penning trap, measurements of the free g-factor of the electron by Hans G. Dehmelt in 1986 [7], yielded a precision of 4×10^{-12}. "For the development of the ion trap technique," Dehmelt and Wolfgang Paul, inventor of the Paul trap, were awarded the 1989 Nobel Prize in Physics [8]. (It was shared with Norman F. Ramsey "for the invention of the separated oscillatory fields method and its use in the hydrogen maser and other atomic clocks [8].) Penning traps lend themselves to

Application	$\delta m/m$
Nuclear structure	$\leq 10^{-6}$
Nuclear models and formulae	$\leq 10^{-7}$
Nuclear astrophysics	$\leq 10^{-7}$
Weak interaction	$\leq 10^{-8}$
Fundamental constants	$\leq 10^{-9}$
CPT Violation	$\leq 10^{-10}$
QED	$\leq 10^{-11}$
Neutrino physics	$\leq 10^{-11}$

Table 1.1: Applications which utilize precise mass measurements and the typical precision $\delta m/m$ required to probe the associated physics.

other high precision measurements such as verification of CPT (charge, parity, time reversal) symmetry [9], tests of the Standard Model [10], decay studies [11], and mass spectrometry, which is the subject of this thesis.

Mass is a fundamental and unique characteristic of an atom. The atomic and nuclear binding energy (by way of the atomic mass) represents the sum of all atomic and nuclear interactions. Mass spectrometry, then, is a powerful probe used in many areas of physics, some of which are listed in Table 1.1 with the typical precision $\delta m/m$ needed [6]. The focus of the present work lies in nuclear physics, where broadly speaking there are four applications: fundamental symmetries, nuclear structure, nuclear astrophysics, and nuclear models.

1.1 Examples of the Importance of Precise Mass Values in Nuclear Physics

1.1.1 Fundamental Interactions and Tests of the Standard Model

Several tests of the Standard Model were featured on the cover of *Discover Magazine* in 2002 as part of the eleven greatest physics mysteries [12]; number four, "do

neutrinos have mass?" In the Standard Model, the mass of the neutrino is zero. The observation of zero-neutrino, double beta decay [13] would contradict the assumption that the neutrino is massless and demonstrate that the neutrino is its own anti-particle. Accurate and precise knowledge of the masses of the mother and daughter nuclei facilitates calculation of the decay rate and narrow the energy window of the double beta decay spectrum. Another test of the Standard Model is the unitarity of the Cabibbo-Kobayashi-Maskawa (CKM) quark-mixing matrix [14]. The up-down quark matrix element V_{ud} can be extracted from the ft-values of superallowed beta emitters, a measure of the decay strength. Three quantities are needed to calculate the ft value: the half life, the branching ratio, and the Q value or mass difference between the mother and daughter nuclei.

1.1.2 Nuclear Structure

The nucleus has been found to have a higher binding energy, colloquially to be more stable, at certain numbers of protons and neutrons, the so-called "magic numbers" (2, 8, 20, 28, 50, ...), which provided the impetus for the nuclear shell model. Shell structure can be easily seen in double mass differences, i.e. two-neutron (two-proton) separation energy S_{2n} (S_{2p}). In general, the S_{2n} decreases smoothly as one moves away from the valley of stability; deviations from this trend indicate microscopic nuclear structure effects such as a shell closure or nuclear deformation [15]. Far from stability, the well known magic numbers may vanish and new ones emerge [15]. Another interesting class of interaction that can be studied with masses is the interaction of the valence neutron(s) and proton(s). The binding energy is enhanced along the N = Z line because of the isospin T = 0 interaction [16,17]; that is when a valence neutron and proton occupy the same orbital, they have nearly identical wavefunctions and interact more strongly than valence nucleons in N $\neq$ Z nuclei. For extremely loosely bound nuclei, a neutron or proton "halo" may occur [18], one or two valence nucleons orbiting a tightly bound core. The extent of the halo is related to the neu-

tron separation energy (the mass difference between neighboring isotopes). The first experimental evidence for halo nuclei was seen in ^{11}Be [19].

1.1.3 Nuclear Astrophysics

Also on the list of greatest physics mysteries [12] is the origin of elements heavier than iron. Three main processes are thought to contribute: The slow neutron capture (s-) process is believed to be responsible for the creation of nuclei close to the valley of stability. The rapid neutron capture (r-) process, expected to be the source of over half the abundance of heavy nuclei, is postulated to occur in supernovae. The rapid proton capture (rp-) process powers type I x-ray bursts and is thought to supply nuclei close to the proton dripline. The path these processes follow depends on the neutron and proton separation energies and on other environmental factors, e.g. the neutron density and the temperature. The mass values are crucial for calculations of final abundances and luminosity [20,21]. As the r-process involves many masses which are inaccessible by mass spectrometry, astrophysicists are forced to rely on nuclear mass models.

1.1.4 Nuclear Models and Mass Formulae

The nucleus is a many-body quantum system under the influence of the electromagnetic, strong, and weak forces. Two problems present themselves: the lack of an exact description of the strong interaction and the complexity of many-body problems. Nuclear mass models have been developed based on microscopic, macroscopic, or both approaches in their description of the nucleus. An early model [22, 23] partly resembles a liquid drop, hence the name the liquid drop model (LDM), and predicts the mass in a macroscopic framework through the volume energy, surface energy, symmetry energy, etc. An example of a microscopic model has already been mentioned, the nuclear shell model, in which each nucleon is bound by a central force calculated

from the average effects of all nucleons [24]. A review of nuclear mass models and formulae [25] showed that the models tend to agree in the region of known masses but diverge in the terra incognita.

In addition to global predictions, there are so-called local models intended to predict an unknown mass close to several known masses [25]. An elegant example and the subject of this dissertation is the isobaric multiplet mass equation (IMME) proposed by Wigner in 1957 [26,27]. To first order, the neutron and proton are identical particles excepting the electric charge of the proton. They can be treated as the different projections of the isospin operator T, where the neutron has isospin up and the proton isospin down. Certain states in different nuclei have the same mass number (A), angular momentum (spin), parity, and isospin; these states have nearly identical wavefunctions and are called isobaric analog states. The small differences in the wavefunctions can be attributed to the Coulomb interaction. As a result, the masses of the multiplet are a quadratic function of the isospin projection T_z = (N-Z)/2:

$$M = a + bT_z + cT_z^2 \tag{1.1}$$

The IMME has been extremely successful [28] and only failed so to speak in light multiplets with an unbound member. Recent high precision measurements have upheld the validity of IMME [29–32] until a remeasurement in the A = 32, T = 2 quintet [33] found a 3 keV shift in the $T_z = 0$ member. The authors of [33] debated whether isospin mixing or an erroneous measurement of the $T_z = 2$ (^{32}Si) member was responsible for the breakdown of the relationship. In the present work the high precision mass measurement of ^{32}Si is presented, and the obtained mass value is used to test IMME.

1.2 Penning Trap Mass Spectrometry of Rare Isotopes

The precision of mass measurement is critical for tests like IMME of isospin symmetry; and, precision is the hallmark of Penning trap mass spectrometry. The technique has proven itself to be highly reliable; no statistically significant disagreements between Penning trap mass measurements have been found. On the other hand, Penning trap mass spectrometry has exposed erroneous mass values determined with other techniques, including β-decay, nuclear reactions, Q-values, and direct mass measurements some of which were well established and highly regarded. Deviations from the accepted mass values of stable isotopes have been observed, such as ^{31}P and ^{32}S, which were measured for this work. These discrepancies have far-reaching consequences: stable nuclei are often used to anchor network calculations and serve as calibrations. Penning trap mass measurements have obtained precisions that range from 10^{-6} to 10^{-11} for stable isotopes [34] and to 10^{-9} for unstable nuclei [30], which matches the range of required $\delta m/m$ listed in Table 1.1. For short-lived isotopes, the precision is typically limited by the half-life; the shortest $T_{1/2}$ of an isotope measured by Penning trap mass spectrometry is on the order of 10 ms [35].

Compared to measurements of stable isotopes, additional challenges are faced when trapping radioactive isotopes. First, the ions have to be created in nuclear reactions; depending on the production mechanism, the beam energy can range from tens of keV to several GeV. The more exotic and more interesting species are generally produced with a small yield, as low as a few ions per hour. Therefore, highly efficient methods are required to manipulate these beams to achieve the beam properties needed for Penning trap mass spectrometry, namely high quality, very low-energy ion bunches. Second, as one approaches the most exotic nuclei at the driplines, the half lives grow shorter, decreasing to the order of tens of milliseconds or less. Consequently, the beam handling and the mass measurement must be executed quickly.

The solutions to these challenges have been tailored to the beam properties, which are largely determined by the production mechanism.

1.2.1 Rare Isotope Production

The three predominant methods to produce rare isotopes are isotope separation on-line (ISOL), fusion-evaporation reactions, and fast projectile fragmentation at higher energies. The ISOL technique impinges a high-energy primary beam of light ions on a thick target of a heavier element; products diffuse out of the target, which is held at a high temperature, and into an ion source. Next they are accelerated to an energy of a few tens of keV, mass separated, and delivered to experiments like the pioneer of rare isotope Penning trap mass spectrometry, ISOLTRAP [36], at ISOLDE at CERN. The related IGISOL technique uses heavy ions which impinge on a thin target; the fragments are thermalized in a small gas volume, swept out, and re-ionized if necessary, and then extracted as low-energy ions; this method is currently being exploited by JYFLTRAP [37]. For fusion and fusion evaporation reactions, low- to medium-energy ions bombard a thin target; the reaction products have significant forward momentum which allows a fraction of them to be mass separated in-flight with magnetic separators. Typical beam energies are 100 keV to a few MeV per nucleon and requires re-thermalization in a low-pressure gas catcher to be coupled to Penning trap mass spectrometers. SHIP at GSI [38] employs this technique to study the heaviest elements, and its resident Penning trap mass spectrometer, SHIPTRAP [39], made the first direct mass measurements in transuranic elements. Fast projectile fragmentation on the other hand relies on accelerating a fast, heavy primary beam that reacts with a thin, light target and in-flight mass separation. Several rare isotope facilities worldwide use of projectile fragmentation and in-flight separation, including SPIRAL at GANIL [40], the FRS at GSI [41], RIPS at RIKEN [42], and the NSCL in the United States [43], where the present work was performed. Statistical in nature and without decay losses, projectile fragmentation can access isotopes far from the valley

of stability on either the proton- or neutron-rich side. However, the beam properties are somewhat opposite to those needed for trapped ion studies. The challenge is to convert a high-energy, high-emittance, continuous, cocktail beam into a low-energy, low-emittance, pulsed, pure beam.

1.2.2 LEBIT

The Low Energy Beam and Ion Trap (LEBIT) facility at the NSCL [44] was the first facility to trap ions produced by fast projectile fragmentation and in the process developed several advanced ion manipulation techniques. A persistent problem of using projectile fragments is beam purity as impurities may shift the measurement or entirely mask the signal in the Penning trap. The beam thermalization process ionizes residual impurities in the buffer gas, creating various stable molecular ions, which are transported out of the gas cell along with the rare isotopes. For his dissertation [45], Pete Schury implemented a multi-stage beam purification system, which filters ions by their mass-to-charge ratio and eliminates all contaminants except isobars (ions with the same mass number, A).

Currently, two techniques are employed to clean isobars. At LEBIT, a dipole excitation [46, 47] drives the ion from the trap but requires an exact identification of each contaminant species, which is a time-consuming and involved process. At ISOLTRAP [36] and JYFLTRAP [37], a buffer-gas filled (preparation) Penning trap accumulates and purifies ions [48–50]. Although the contaminant ions need not be identified, the process is slow and better suited for long-lived species. A faster and more efficient technique was explored, and the results are presented in the second half of this dissertation. Stored waveform inverse Fourier transform (SWIFT) [51] eliminates the need for individual contaminant identification like dipole cleaning and does not require cooling like mass-selective buffer gas cooling.

1.3 Outline

This dissertation describes the LEBIT system and the principles of Penning trap mass spectrometry before presenting the results of mass measurements of ^{32,33}Si, ^{31,34}P, and ^{32}S. The nuclides ^{32}Si and ^{32}S are members of the A = 32, T = 2 quintet, and their mass values were used for the most stringent test of IMME. Next the discussion turns to reducing the systematic uncertainties in such mass measurements due to beam impurities, which posed a significant challenge in the measurement of ^{32}S. The SWIFT cleaning technique is described, its implementation chronicled, and the ultimate test of SWIFT cleaning, separating the carbon monoxide and nitrogen doublet, is presented.

Chapter 2

The LEBIT Facility

Located at the center of the Michigan State University campus is the National Superconducting Cyclotron Laboratory (NSCL), home to the nation's foremost rare isotope facility and the LEBIT Penning trap mass spectrometer. LEBIT was the first and remains the only Penning trap mass spectrometer to study rare isotopes produced by fast beam fragmentation. This chapter presents the facility and the advanced ion manipulation techniques used to convert the relativistic beam into brilliant ion bunches.

Figure 2.1 shows an overview of the LEBIT beamline. Three major components are connected by an electrostatic beam transport system [52]. Rare isotope beams are delivered from the Coupled Cyclotron Facility (CCF) to the gas stopping station [53, 54], where the beam is thermalized in the gas cell and transported by radiofrequency quadrupole (RFQ) ion guides [55]. After being transported out of the high energy vault, the continuous beam is cooled and bunched in the beam cooler and buncher [5, 56], another RFQ device. Finally, the 9.4 T Penning trap mass spectrometer [57, 58] receives the ion pulses for high-precision mass measurements. Beam Observation Boxes (BOB) are situated along the beam line and contain diagnostic equipment such as Faraday cups, microchannel plate (MCP) detectors, and silicon detectors. Subsequent to the present work, the LEBIT facility was decommissioned and moved to a new location in the NSCL. These physical changes and their impact on LEBIT

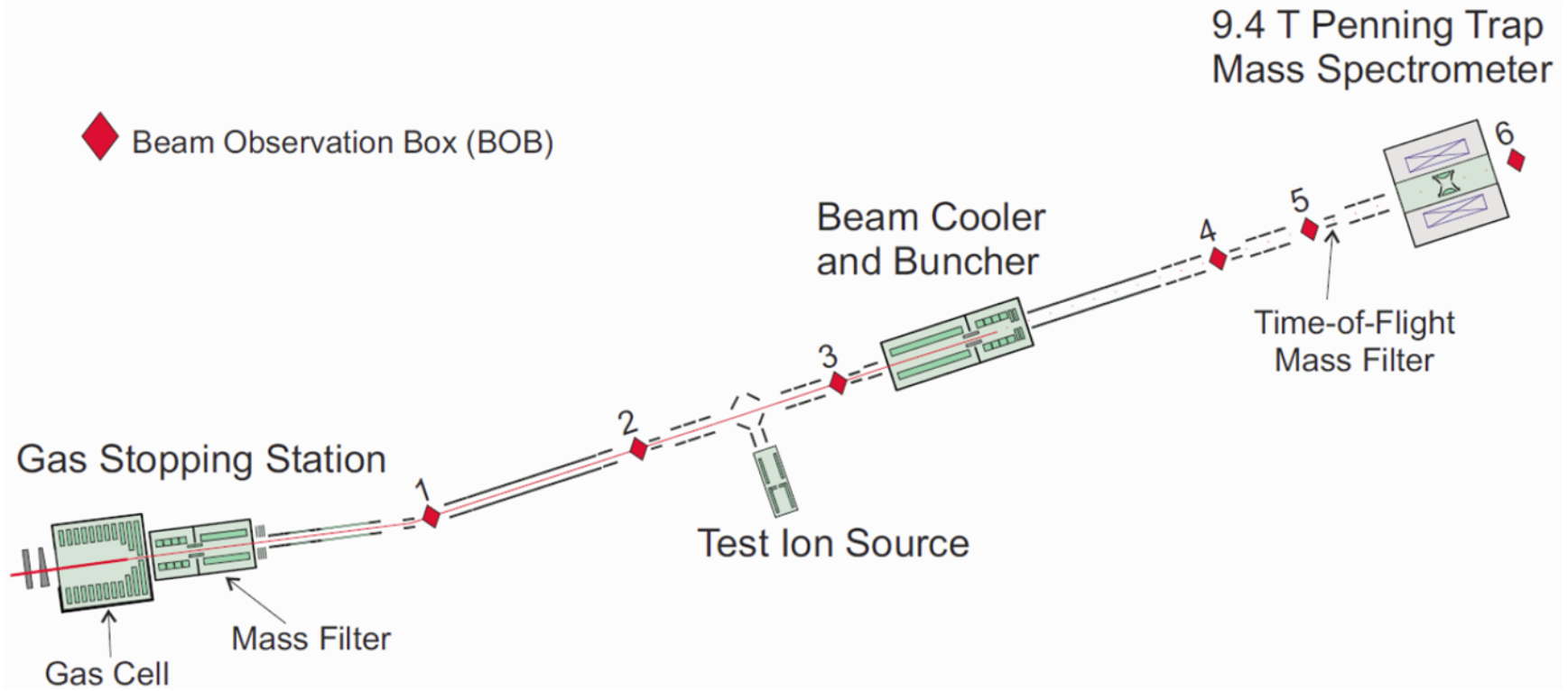

Figure 2.1: Layout of the LEBIT beamline from 2005-2009. For interpretation of the references to color in this and all other figures, the reader is referred to the electronic version of this dissertation.

will be discussed in Chapter 6. The mass measurements described in this thesis were made in the configuration described in this chapter and shown in Figure 2.1.

2.1 Beam Production at the NSCL

The layout of the experimental area at the NSCL at the time of this work is shown in Figure 2.2. An Electron Cyclotron Resonance (ECR) ion source produces a primary ion beam of highly charged stable isotopes, which is injected into the smaller K500 cyclotron, which accelerates the beam to on the order of 14 MeV/u, depending on the ion of interest. The ions are ejected from the K500 and subsequently pass through a stripper foil, which generally removes the remaining electrons, near the center of the K1200. The second cyclotron accelerates the beam to 80-150 MeV/u. When the stable beam impinges on a (thin, hundreds of mg/cm^2) target, fragmentation occurs and rare isotopes are created. The ions of interest are separated in-flight from other fragmentation products in the A1900 fragment separator [43] and then delivered to the different experimental vaults (N2-N5, S1-S3). LEBIT is located in the N4 and N5 vaults. The high energy section of LEBIT, the gas stopping station, is located in the N4 vault while the low energy sections are found in N5, where the beam energy has a few keV.

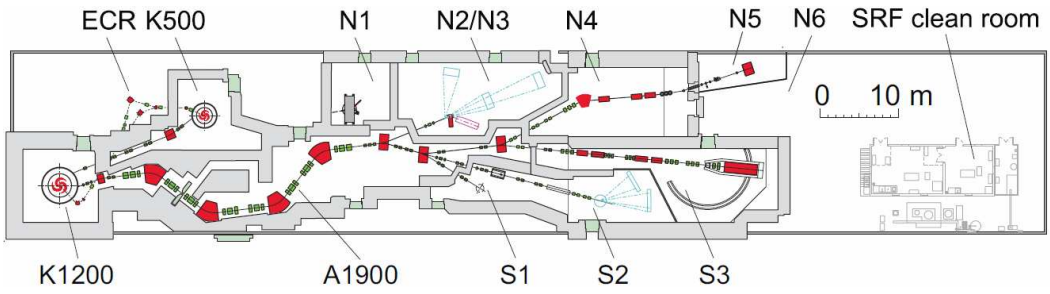

Figure 2.2: Layout of the experimental area at the NSCL from 2007-2009.

2.2 Gas Stopping Station

The A1900 fragment separator delivers the beam to the gas stopping station with an energy of approximately 100 MeV/u. The beam loses most of its energy as it passes through a system of adjustable glass degraders. A pair of plates are rotated to adjust their effective thickness and to control the stopping distribution of the ions in the gas. An aluminum wedge degrader is used to reduce the momentum spread of the secondary beam, thereby minimizing the range distribution of the ions in the gas.

The beams enters the 51 cm-long gas cell through a thin beryllium window. The mechanical design of the gas cell is pictured in Figure 2.3. The chamber is filled with 200-500 mbar of ultra-pure (ppb) helium gas. Since helium has the highest first ionization energy of any atom, the rare isotopes do not neutralize. Collisions with the buffer gas thermalize the incoming ions while charge exchange reactions reduce the charge state to Q = +1 or +2.

Inside the gas cell, a system of ring electrodes creates an electrostatic field to guide the ion towards the extraction region. Four spherical electrodes (called the "flower") are used to approximate the field of a point charge in order to focus the beam into the opening of a supersonic nozzle. Finally, gas flow sweeps the ions into the radiofrequency quadrupole (RFQ) ion guides.

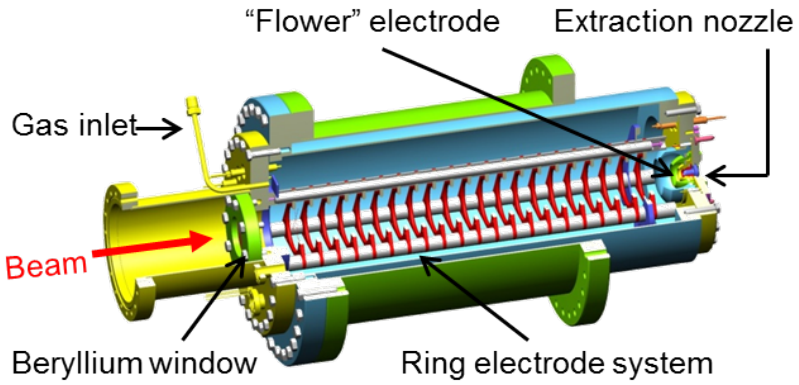

Figure 2.3: Mechanical design of the gas cell. The ring electrodes guide the ion to the extraction region. The "flower" electrode creates a focusing potential. Gas flow through the supersonic jet ejects the ions into the RFQ ion guides.

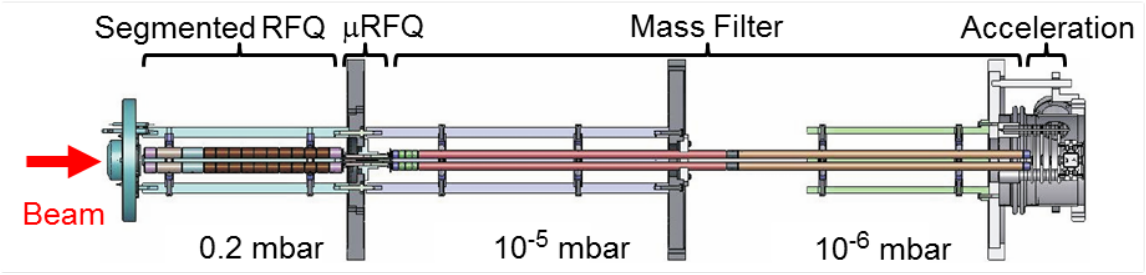

Figure 2.4: Mechanical design of the RFQ ion guides. The three sections are followed by a 5 keV acceleration region and end at BOB1.

RFQ ion guides provide radial confinement with an oscillating voltage applied to four rods, each phase-shifted 180° with respect to their nearest neighbor, as explained in [59,60]. The ion guides were part of the thesis work of Pete Schury [45] and a schematic representation is shown in Figure 2.4. They are housed in three vacuum chambers and can be decomposed into three functional sections. The first section, a segmented RFQ, includes an electrostatic gradient to drag the ions through the residual helium gas as the pressure in the first vacuum chamber can be as high as 0.2 mbar. A small RFQ, called the μRFQ, provides efficient transport through a small diaphragm for differential pumping. The third section can be operated as a mass filter to select the mass-to-charge ratio of the rare isotope and to suppress unwanted contaminants, principally stable molecular ions produced in the gas cell by ionization of residual contamination. Beam purification was essential for this work, and suppression of these contaminants will be explored in Chapters 4 and 5. Radioactive species can be detected by their decay after being stopped in a retractable silicon detector in BOB1. Mass scans are performed by measuring activity as a function of the charge-to-mass ratio transported through the mass filter. In this manner, the form of the radioactive species (e.g. atomic, molecular, charge state) is identified.

After the mass filter, the ions are accelerated to 5 keV·Q and transported through the shielding wall into the low energy area, where steering and focusing elements guide the beam to the beam cooler and buncher. Located between BOB2 and BOB3 is a plasma-type ion source, which can provide stable ion beams for system optimiza-

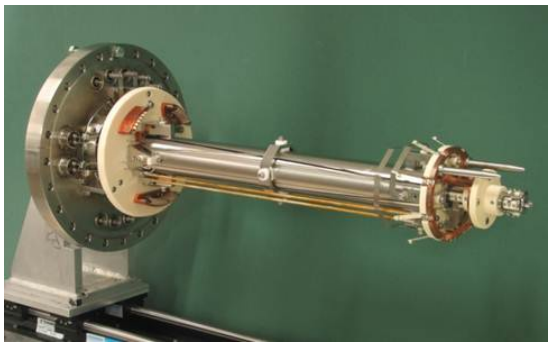

(a) The cooler and μRFQ

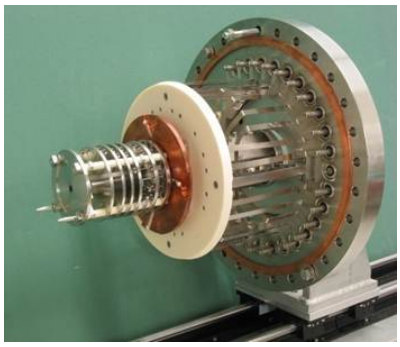

(b) The buncher and ejection optics

Figure 2.5: Photographs of the LEBIT beam cooler and buncher.

tion, magnetic field calibration, and offline tests. Being placed perpendicular to the main beam line, the stable ion beam is merged with the rare ion beam with a 90° electrostatic bender.

2.3 The Beam Cooler and Buncher

The LEBIT beam cooler and buncher accepts the continuous 5 keV·Q beam from the gas cell (or the stable ion source) and converts it into low-energy, low-emittance ion pulses for efficient ion capture in the Penning trap. Photographs of the device are shown in Figure 2.5. It is a two-stage linear RFQ ion trap filled with a low-pressure buffer gas for ion cooling and capture [5, 56]; it was studied extensively in an earlier thesis work [52]. The first stage is a pre-cooler filled with helium or neon at pressures on the order of 2×10^{-2} mbar. Neon is sometimes used to increase the likelihood of collision-induced dissociation (CID) to break up molecular ions. The second stage performs the final cooling, trapping, and bunching. The two are connected by a μRFQ identical to the one in the gas stopping station also for differential pumping.

The ions are electrostatically decelerated to ≈10 eV before entering the pre-cooler, where they are slowed and the transverse emittance is reduced. They are transported through the μRFQ. The linear RFQ trap is operated with helium at

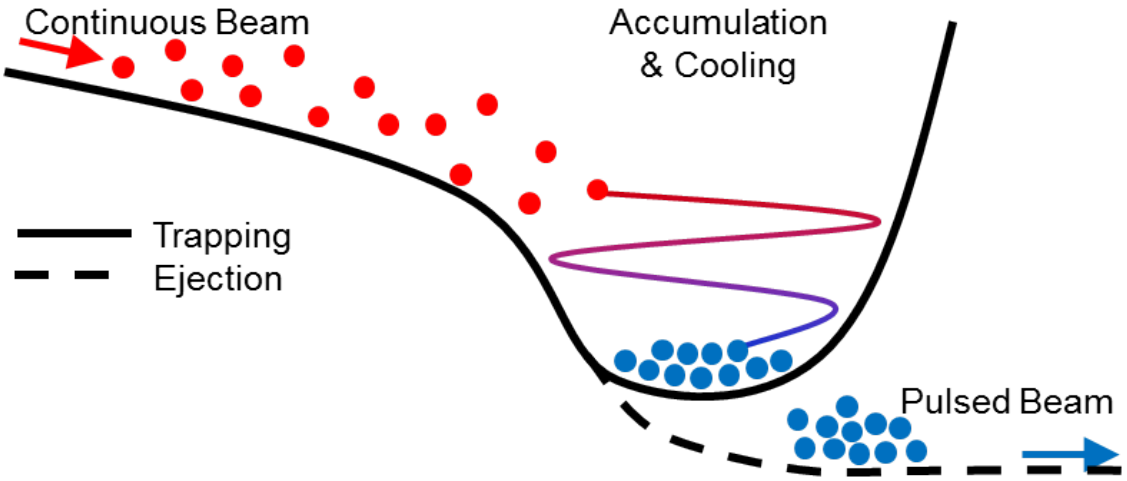

Figure 2.6: Cartoon depicting the principles of the LEBIT beam cooler and buncher. The solid line corresponds to the electrostatic potential used to trap, cool, and accumulate ions while the dashed line is that to eject ions from the buncher. Ions are cooled by collisions with the low pressure buffer gas, typically helium.

pressures $\approx 10^{-4}$ mbar to minimize beam heating via collisions with the buffer gas during extraction. The electrostatic trap is created by applying suitable potentials on cylindrical electrodes surrounding the RFQ structure. Ions are accumulated and cooled for 20-30 ms before they are extracted as an ion pulse with a FWHM $\approx$100 ns. The ejected ion pulse has a reduced transverse emittance. A cartoon of the process is shown in Figure 2.6. The cooler and buncher has a cryogenic heat shield with thermal contacts to the electrodes. Operation of the device at lower temperatures reduces the kinetic energy of the buffer gas and improves the brilliance of the ejected ion pulses. The system cooling also reduces the residual pressure of gases other than the noble gases needed for beam cooling.

A second beam transport system, at -2 kV, connects the beam cooler and buncher to the Penning trap. It includes a drift tube, steering elements, Einzel lenses, and ion detectors. The section is also used as a time-of-flight (TOF) mass filter by quickly switching the potential applied to a deflector in BOB5 as will be described in Section 2.5.

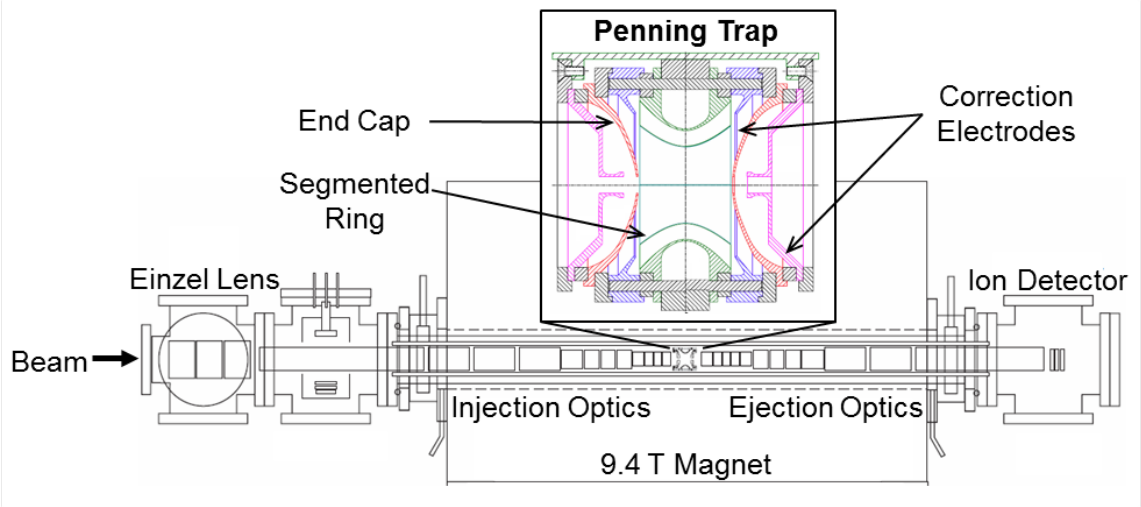

Figure 2.7: Schematic layout of the LEBIT Penning trap mass spectrometer. The inset shows the mechanical design of the Penning trap itself.

2.4 The Penning Trap Mass Spectrometer

Mass measurements are performed in the LEBIT Penning trap mass spectrometer, shown schematically in Figure 2.7. Details on the design and construction of the Penning trap can be found in the dissertation of Ryan Ringle [61]. The main components of a Penning trap are two hyperbolic end caps and a ring electrode placed in a homogenous magnetic field, **B**. A moving ion of mass m and charge q in a magnetic field undergoes cyclotron motion, $\omega_c = q/m \cdot B$. While the magnetic field supplies radial confinement, the axial confinement is provided by the electrostatic quadrupole potential created by a voltage difference between the ring and end cap electrodes. Figure 2.8 shows a cartoon of a Penning trap alongside a photograph of the LEBIT Penning trap.

LEBIT utilizes an actively shielded, persistent, solenoidal, superconducting magnet with a room-temperature horizontal bore and with a field strength of 9.4 T. Gabrielse coils [62] were included to counteract external field changes. A pair of insulated copper wires are wound around the bore tube to permit either baking of the bore tube or compensation of the natural decay of the magnetic field [57, 58]. The pressure of the helium bath is stabilized with a precision barometer and an electro-

magnetic valve controlled by a PID loop; variations in the ambient pressure were found to affect the evaporation of liquid helium that caused non-linear changes in magnetic field strength.

The injection and ejection optics consist of a series of cylindrical electrodes [61]. The electrode directly before the Penning trap is used as a "Lorentz" steerer [61, 63] to position the ions in the trap. The cylinder is quartered and biased to produce an electric dipole field, resulting in a force in an $\mathbf{E} \times \mathbf{B}$ force on the ion and off-axis injection into the Penning trap. The center of each end cap electrode has a 4-mm diameter hole to allow injection and ejection of the ions from the Penning trap. A dynamic capture process where voltages on the end caps are switched allows ions to enter, to be trapped in, and later to be ejected from the trap. Correction ring and tube electrodes minimize deviations from the desired hyperbolic electric field. After ejection from the trap, ions pass through several drift tubes to reach BOB6, where they are detected with an MCP detector in a Daly configuration [64] or directly with a channeltron. In the Daly configuration, a metal plate is biased to a high voltage and mounted parallel to the MCP, both of which are positioned off-axis. Ions strike the

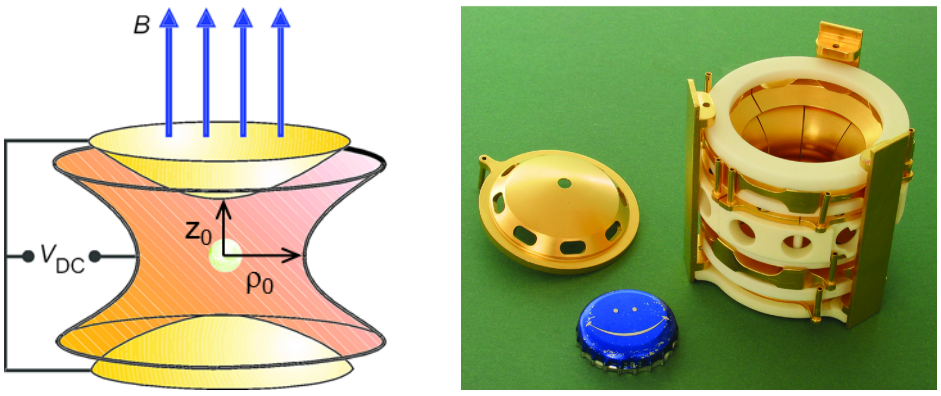

(a) (b)

Figure 2.8: (a) Illustration of a hyperbolic Penning trap. A homogenous magnetic field provides radial confinement while a static electric field provides axial confinement. (b) Photograph of the LEBIT hyperbolic Penning trap. The end cap has been removed to reveal the eight-fold segmented ring electrode. A 4-mm diameter hole in the end caps permits injection and ejection of ions.

plate and release a fusilade of secondary electrons, which are collected on the MCP. The LEBIT Penning trap mass spectrometer was designed for use with the time-of-flight ion-cyclotron-resonance (TOF-ICR) technique [48, 49, 65], which is particularly well suited to mass determination of short-lived rare isotopes. The technique will be described in section 2.4.3 after the basic concepts of Penning traps are explained.

2.4.1 Ion motion in a Penning trap

Detailed discussions on ion motion in a Penning trap can be found in [49, 66]; as such, only a brief overview of the ion trajectory is presented. The applied electrostatic potential modifies the ion motion from pure cyclotron motion into three independent eigenmotions. In the axial direction, the potential can be described in cylindrical coordinates (r, θ, z) by the expression:

$$V(r,z) = \frac{V_{DC}}{4d^2}(2z^2 - r^2). \tag{2.1}$$

where V_{DC} is the electrostatic potential difference between the ring and end cap electrodes and $d = \sqrt{r^2/4 + z_0^2/2}$ is the characteristic size of the trap. The quadrupole trapping fields then are given by:

$$\begin{aligned} E_r &= \frac{V_{DC}}{2d^2}\, r \\ E_z &= -\frac{V_{DC}}{d^2}\, z. \end{aligned} \tag{2.2}$$

In the axial direction, the only force arises from the quadrupole electric field, $F_z = q \cdot E_z$, which causes axial oscillations with a frequency:

$$\omega_z = \sqrt{\frac{qV_{DC}}{md^2}}. \tag{2.3}$$

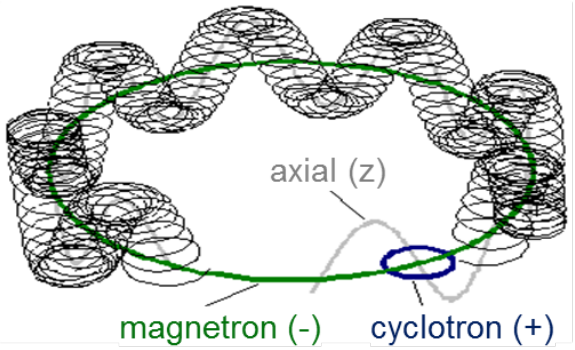

Figure 2.9: Representation of the three independent eigenmotions of an ion in a Penning trap. The two radial motions are the magnetron (-) and the reduced cyclotron (+) oscillations; the third is the axial oscillation (z).

The remaining two eigenmotions, in the radial plane, are a slow magnetron motion ω_- due to the $\mathbf{E} \times \mathbf{B}$ drift ion motion and a reduced cyclotron motion ω_+:

$$\omega_\pm = \frac{\omega_c}{2} \pm \sqrt{\frac{\omega_c^2}{4} - \frac{\omega_z^2}{2}}. \tag{2.4}$$

The trajectory of the ion is made up from the combination of the axial, magnetron, and reduced cyclotron motions; the three eigenmotions and their composite are pictured in Figure 2.9.

For an ion with $m = 100$ u in a Penning trap of size $d = 1$ cm, in a magnetic field $B = 9$ T, with $V_{DC} = 10$ V, the eigenfrequencies are of the order $\omega_-/2\pi \approx 1$ kHz, $\omega_z/2\pi \approx 100$ kHz, and $\omega_+/2\pi \approx 1$ MHz. In general, the eigenfrequencies follow the relation $\omega_- < \omega_z < \omega_+$. There are three other important relations among the frequencies, the first of which is called the Invariance Theorem [67].

$$\omega_c^2 = \omega_+^2 + \omega_-^2 + \omega_z^2 \tag{2.5}$$

$$\omega_c = \omega_+ + \omega_- \tag{2.6}$$

$$\frac{\omega_z^2}{2} = \omega_+ \omega_- \tag{2.7}$$

The Invariance Theorem is true even for small (of order 10^{-3}) misalignments and

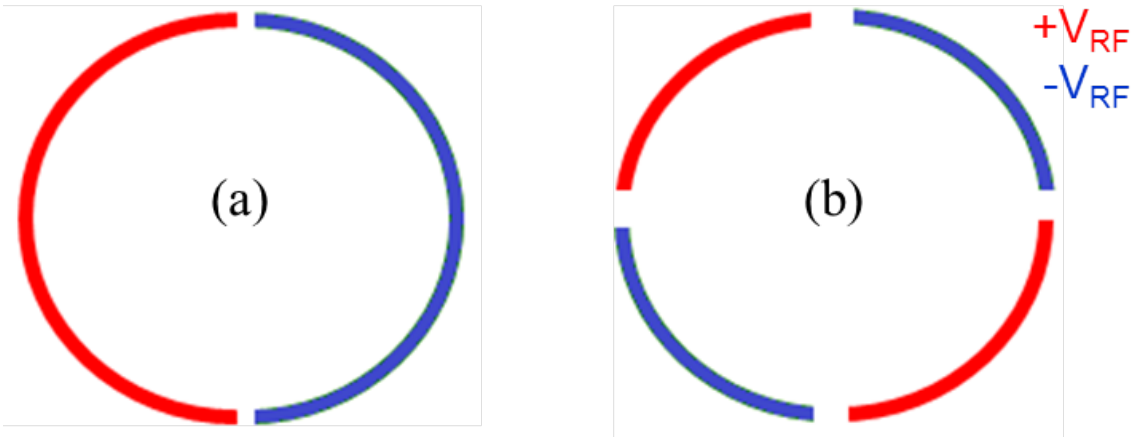

Figure 2.10: Schematic drawing of the segmented ring electrode in a Penning trap. The RF voltage V_{RF} is applied 180° out of phase between the red ($+V_{RF}$) and blue ($-V_{RF}$) segments. (a) Dipolar excitation. (b) Quadrupolar excitation.

distortions of the trapping potential [66, 68]. The effect of trap anharmonicities on the mass determination will be addressed again in Section 2.4.3.

2.4.2 Excitation of ion motion

The trapped ion's radial eigenmotion can be excited by applying multipolar azimuthal RF fields [48] to the trapping electrodes. The most common method to introduce such fields is to segment the ring electrode and to apply RF voltages such that the potentials on adjacent electrodes are 180° out of phase, as illustrated in Figure 2.10. An n-pole field can be generated by 2^n segments and is capable of exciting eigenmotions at frequencies equal to the sum of 2^{n-1} eigenfrequencies. For example, a dipole excitation at $\omega_\pm$ drives either the reduced cyclotron or the magnetron motion and increases the eigenmotion amplitude, $\rho_\pm$, [46, 47]. Two common uses for dipole excitations are to place the ion on a magnetron orbit in preparation for mass determination ($\omega_{RF} = \omega_-$) or to increase the reduced cyclotron radius of a particular species of ion and drive it out of the Penning trap ($\omega_{RF} = \omega_+$). A quadrupole RF field may couple both radial eigenmotions; for mass determination, one applies an RF field at $\omega_+ + \omega_- = \omega_c$, which causes periodic beating between magnetron and

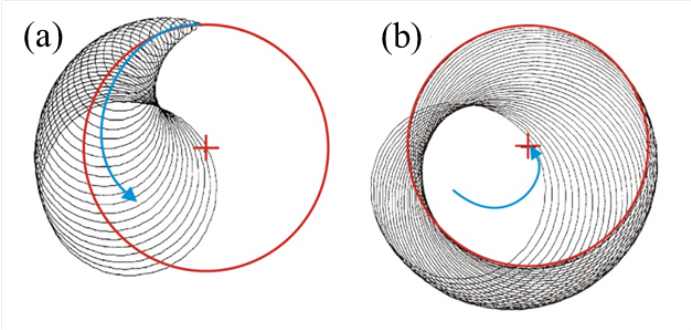

Figure 2.11: (a) The ion begins with pure magnetron motion, indicated by the red circle. When the quadrupole RF field at $\omega_c = \omega_+ + \omega_-$ is turned on, the reduced cyclotron radius grows while the magnetron radius decreases. (b) Full conversion of magnetron to reduced cyclotron motion is shown

reduced cyclotron motion, illustrated in Figure 2.11. Since $\omega_+ > \omega_-$, i.e. the energy associated with the reduced cyclotron motion is greater than that associated with the magnetron motion, the conversion of ρ_- to ρ_+ is accompanied by a significant increase in radial energy, which can be detected by the ion's time-of-flight out of the trap and used to identify the cyclotron frequency. At LEBIT, the ring electrode is divided into eight segments to permit dipolar, quadrupolar, and octupolar excitations, the last excitation offers the potential of increased resolving power and was investigated in an earlier dissertation by Ringle [61].

2.4.3 Mass Determination

At LEBIT, the $\omega_c = \omega_+ + \omega_-$ cyclotron frequency is probed. For a given product of the excitation time and amplitude and $\omega_{RF} = \omega_c$, the initial magnetron motion of the trapped ion is completely converted into cyclotron motion. Since $\omega_+ > \omega_-$, the energy associated with the reduced cyclotron motion is higher than that associated with the magnetron motion, and the ion gains radial energy. Changes in the radial energy are detected with the time-of-flight ion-cyclotron-resonance (TOF-ICR) technique [48, 49, 65]. After ejection from the trap, the ion travels through ejection optics to a detector, where its time of flight (TOF) relative to the ejection pulse is recorded. The magnetic field strength generally decreases along the ion's path. Due to its reduced

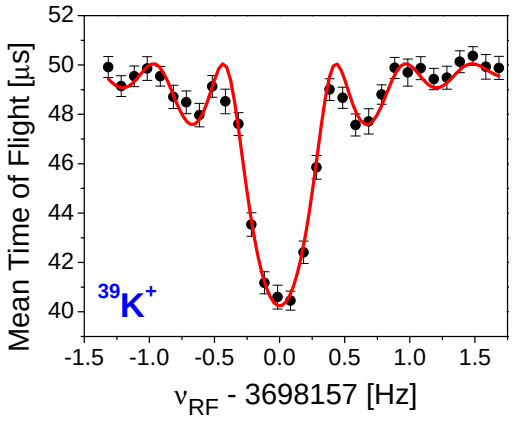

Figure 2.12: Cyclotron resonance curve of $^{39}K^{+}$ ions with an excitation time of $T_{RF} = 500$ ms. The solid curve is a theoretical fit [49] to the data.

cyclotron motion, the moving ion possesses a magnetic moment $\mu = E_r/B\ \hat{z}$ which interacts with the field gradient, and it experiences an axial force, $F = -\mu\frac{\partial B}{\partial z} = -\frac{E_r}{B_0}\cdot\frac{\partial B}{\partial z}$, where B_0 is the maximum field strength. By the time the ion exits the main magnetic field, all of its radial energy has been converted into axial energy and a reduced TOF is measured. The total TOF can be calculated by the expression:

$$TOF(\omega_{RF}) = \int_{z_0}^{z_1} \sqrt{\frac{1}{2}\frac{m}{E_0 - q\,V(z) - \mu(\omega_{RF})\,B(z)}}dz. \tag{2.8}$$

where E_0 is the total initial energy of the ion, q is its charge, and $V(z)$ is the electric potential and $B(z)$ is the magnetic field strength, both functions of the ion trajectory from the trap (z_0) to the detector (z_1).

Using the TOF-ICR method, a cyclotron resonance curve can be obtained as a function of the RF frequency similar to the one shown in Figure 2.12. The resonance is obtained by applying a quadrupolar RF field over a range of frequencies ω_{RF} close to ω_c and calculating the average measured TOF as a function of ω_{RF}. The actual cyclotron frequency can be determined by fitting the theoretical line shape to the data [49].

The magnetic field strength is measured by applying the TOF-ICR technique to

a stable ion with a well known mass m_{ref}. To obtain the highest precision, each measurement of the radioactive ion is interleaved with a measurement of the reference ion, whose mass is well known. The primary experimental result is thus the frequency ratio $\mathrm{R} = \omega_c^i/(\omega_{ref}^{int})^i$, where $(\omega_{ref}^{int})^i$ is linearly interpolated from the reference measurements which bracket the measurement of ω_c^i. The ratio of the cyclotron frequencies yields the mass of the radioactive ion:

$$m = \frac{q}{q_{ref}} \cdot \frac{\omega_{c,ref}}{\omega_c} \cdot m_{ref} \tag{2.9}$$

where q/q_{ref} is the charge ratio of the rare isotope and the reference ion. Higher order multipoles in the electric potential and magnetic field inhomogeneities can lead to frequency shifts in the sideband $\omega_c = \omega_+ + \omega_-$ [68], and a correction must be added to the ratio $\mathrm{R} = \omega_c/\omega_{c,ref}\ (1+\delta)$ [68]. At LEBIT, the contribution to δ from various sources of possible trap anharmonicities has been studied carefully [58]: $5 \times 10^{-11}\ \Delta_{A/Q}$ due to deviations from the quadrupole field and $\leq 1 \times 10^{-10}\ \Delta_{A/Q}$ due to the trap eccentricity, where $\Delta_{A/Q}$ is the difference in the mass-number-to-charge-state ratio of the rare and reference ions. The effect of the magnetic field inhomogeneity shifts the $\Delta\omega_c/\omega_c = \pm 1 \times 10^{-9}$ [58].

This correction [68] depends on the eccentricity of the trapping potential (ϵ) and the misalignment of the trap axis and the magnetic field (θ).

$$\delta = \left(\frac{9}{4}\theta^2 - \frac{1}{2}\epsilon^2\right)\left(\frac{\omega_{+,ref} - \omega_+}{\omega_+}\right)\frac{\omega_-}{\omega_{+,ref}} + \ldots \tag{2.10}$$

At LEBIT, θ and ϵ have not been measured directly; however, a highly conservative estimate is on the order of 10^{-2} for either anharmonicity. The second and third factors in Equation 2.10 are of order 10^{-3} each. A conservative estimate of the shift in the cyclotron frequency ratio then is 10^{-10}, an order of magnitude below the lowest statistical uncertainty of any measurement in this work.

The resolving power, R, achievable with the TOF-ICR technique is given by the

expression:

$$R = \frac{m}{\Delta m} = \frac{\omega_c}{\Delta\omega_{FWHM}} \tag{2.11}$$

where $\Delta\omega_{FWHM}$ is the line-width of the ω_c frequency determination. For a given RF excitation time, T_{RF}, the line-width will be Fourier-limited to $\Delta\omega \approx T_{RF}^{-1}$. The resolving power then goes as $\omega_c \cdot T_{RF}$. The statistical precision can be estimated [69] as:

$$\frac{\delta\omega_c}{\omega_c} = \frac{\delta m}{m} \approx \frac{\gamma}{R\sqrt{N}} \approx \frac{2\pi\gamma}{\omega_c T_{RF}\sqrt{N}} \tag{2.12}$$

where N is the number of detected ions and γ, a system-dependent coefficient, is $\approx$0.3 at LEBIT [58]. γ was determined from high-statistics measurements of the cyclotron frequency of $^{39}K^{+}$ from the stable ion source.

2.5 Beam Purification Techniques

The simultaneous storage of more than one ion species in the Penning trap can lead to systematic errors in the mass determination [70] from the Coulomb interaction of the radioactive ion with the contaminant ions and must be suppressed. Unfortunately, the gas cell which enables Penning trap mass spectrometry at the NSCL is also a large source contaminant ions. Every incoming fast ion produces about one million He^{+}-e^{-} pairs in the gas cell; the ionized helium rapidly charge exchanges with residual impurities in the buffer gas. Or, occasionally the rare isotope itself may ionize an impurity. These contaminant ions will be transported from the gas cell through the beam line. During the course of many mass measurements, about 700 molecular ion species have been unambiguously identified at LEBIT. Consequently, the previous work of Pete Schury [45] included the implementation of a multi-stage beam purification system: the RFQ mass filter, collision-induced dissociation in the cooler, a time-of-flight mass filter, and in-Penning trap cleaning. This system was used in the present work and will be briefly described.

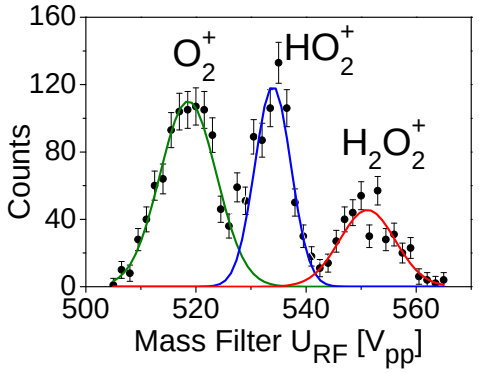

(a) RFQ mass filter

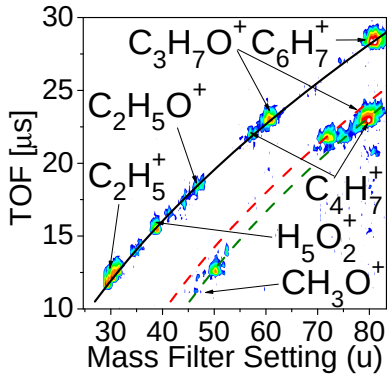

(b) Collision-induced dissociation (CID)

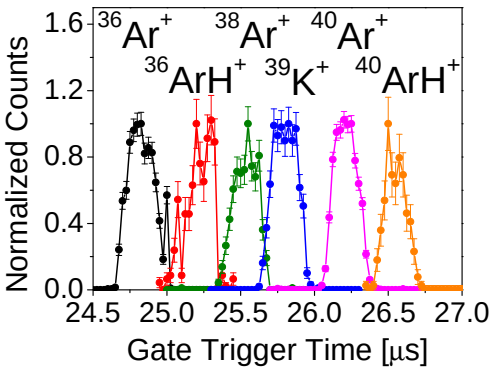

(c) Time-of-flight (TOF) mass filter

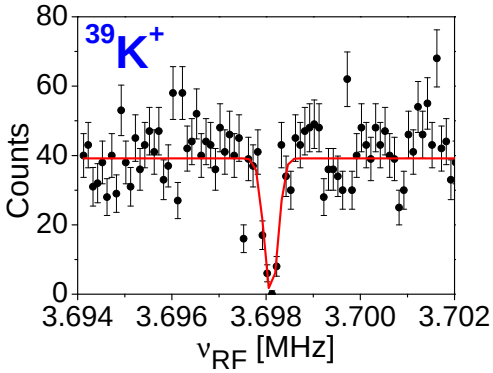

(d) Dipole cleaning in the Penning trap

Figure 2.13: Results from the multi-stage beam purification system of LEBIT. (a) Mass scan at resolving power ≈50 demonstrates the single mass resolution of the RFQ mass filter. The mass peaks were identified unambiguously with the Penning trap mass spectrometer. (b) Time of flight after the cooler and buncher (CID) versus mass scan of the RFQ ion guides. Helium was used as the buffer gas in the ion guides. The solid curve indicates ions which did not dissociate, and the two dashed curves indicate the loss of CH_4 and H_2O by the initial ion. (c) Transmission for several ion species as a function of their TOF from the buncher. A fast kicker prevents unwanted ions from reaching the Penning trap. (d) Counting rate of detected $^{39}K^+$ following a dipole excitation in the Penning trap.

The mass filter, the last section of the RFQ ion guides (Figure 2.4), selects ions by their charge-to-mass ratio m/q. A four-stage Brubaker or delayed DC ramp [71] was applied to the ion guide to maximize the mass filter acceptance and transmission. The resolving power of ≈50 was found to be sufficient for single mass unit separation as can be seen in 2.13a.

The molecular isobaric ions are then delivered to the beam cooler and buncher, where collision-induced dissociation (CID) can occur. In this widely applied process [72–74], a molecular ion collides with the buffer gas and generally emits a neutral molecule. The energy of the collision must be high enough to break the molecular bond (>10 eV) which can be achieved by either a heavy buffer gas or by increasing the incident beam energy. The former risks larger recoil energies and RF heating; however, the latter is easily achieved at LEBIT by increasing all of the gas cell and ion guide voltages by several tens of volts. The effect of CID is easily analyzed using time-of-flight (TOF) mass spectrometry of the ions exiting the cooler and buncher after CID as was performed for another recent experiment [45]. At LEBIT, ion pulses are ejected from the beam cooler and buncher and detected 2.5 m downstream at BOB5. The time of flight is measured and plotted in Figure 2.13b; the upper diagonal line of peaks indicate molecules which did not dissociate while the peaks below represent those which did.

The combination of TOF mass spectroscopy and a fast-switching deflector amounts to a TOF mass filter, which was thoroughly investigated by Josh Savory [75]. The deflector consists of a pair of plates in the horizontal and vertical directions; an applied voltage prevents ions from reaching the Penning trap. When the rare isotopes of interest should pass, a fast switch (≈300 ns) drops the deflector voltage to a near-zero value for optimal transport. The FWHM of the ion pulse is ≈100 ns; the resolving power of this TOF mass filter was found to be in excess of 400. The time of flight separation of masses A = 36 - 41 can be seen in Figure 2.13c.

Any remaining isobaric contaminant can be individually removed from the Penning trap by a dipole excitation of its reduced cyclotron motion [46,47]. For sufficiently large RF amplitudes, the ion is driven to a large orbit, where it neither interacts with the rare isotope nor is extracted from the Penning trap. This highly selective process was exploited in this thesis work but requires the exact identification of the contaminant ion, a somewhat time-consuming process. In Figure 2.13d, the counting rate is

constant except at $\nu_{RF} = \nu_c$, where the counting rate falls to zero.

2.6 Overview of LEBIT Performance

The extraction efficiency of thermalized, rare isotopes from the gas cell was measured during the first commissioning runs of the gas cell to be ≈5% at an implantation rate of ≈40 pps of a ^{38}Ca/^{37}K cocktail beam [54]. Studies of the beam cooler and buncher were performed offline using the plasma-type ion source. Transmission from BOB3 to BOB6 was 70% for currents up to 10 nA in continuous mode [52]. Losses in either the -5 kV and -2 kV beam transport systems or the Penning trap are negligible with optimization of beam transport elements. The total efficiency, including detector efficiency, of rare isotopes from BOB1 through the Penning trap is ≈15%.

Excellent cyclotron resonance curves require on-axis beam, precision injection into the Penning trap, well tuned potentials, and proper ejection from the trap. The precision and accuracy achievable at LEBIT has been studied with stable ions, in particular ^{39}K^{+}, ^{40}Ar$^{1+,2+}$, and several isotopes of Kr^{+}. The measured frequency ratio of ^{23}Na^{+} and ^{40}Ar^{2+}, both known to sub-ppb precision, was found to agree fully with the literature values [76] with a deviation of only $3(5) \times 10^{-9}$. For ion pairs who have a larger mass difference, the effect of mass-dependent systematic effects has been measured to be less than $5(5) \times 10^{-10}/u$ [30].

During the first running phase at LEBIT, from May 2005 to July 2009, the masses of 11 elements and roughly 40 isotopes have been measured; the rare isotopes measured were ^{26,32,33}Si, ^{29,34}P, $^{37-38}$Ca, $^{40-44}$S, $^{63-66}$Fe, $^{63-67}$Co, $^{66-68,80}$As, $^{68-70,81g,81m}$Se, and ^{70,70m}Br. With $T_{1/2}$ = 96 ms, ^{66}As was as the shortest-lived nuclide measured at LEBIT [20]. The mass measurement of ^{37}Ca [77] testifies to the sensitivity at LEBIT, where cyclotron resonance curves were obtained with a total of only ≈50 detected ions. ^{32}Si is a member of the A = 32, T = 2 quintet; and their mass measurements contribute to the test of the isobaric multiplet mass equation and

is the focus of the present work.

Chapter 3

Test of the Isobaric Multiplet Mass Equation with the A = 32, T = 2 Quintet

To first order, the strong interaction is the same for protons and neutrons. To capitalize on this phenomenon, Heisenberg introduced the concept of isospin [78], which considers the proton and the neutron as opposite (spin) projections of the isospin operator T. Although isospin is not an exact quantum number, it is conserved with high precision. Wigner exploited isospin to predict masses with the isobaric multiplet mass equation (IMME) [26, 27]; within an isobaric multiplet (states with the same mass number A, angular momentum, parity, and isospin), the masses of the states follow the parabolic expression:

$$M(T_z) = a + bT_z + cT_z^2. \tag{3.1}$$

where T_z = (N-Z)/2. Higher order terms, $d\mathrm{T}_z^3$ and $e\mathrm{T}_z^4$, require second order Coulomb effects, charge-dependent nucleon-nucleon interaction, or many body forces [79–82]. Numerous studies of isospin multiplets have confirmed the validity of the quadratic

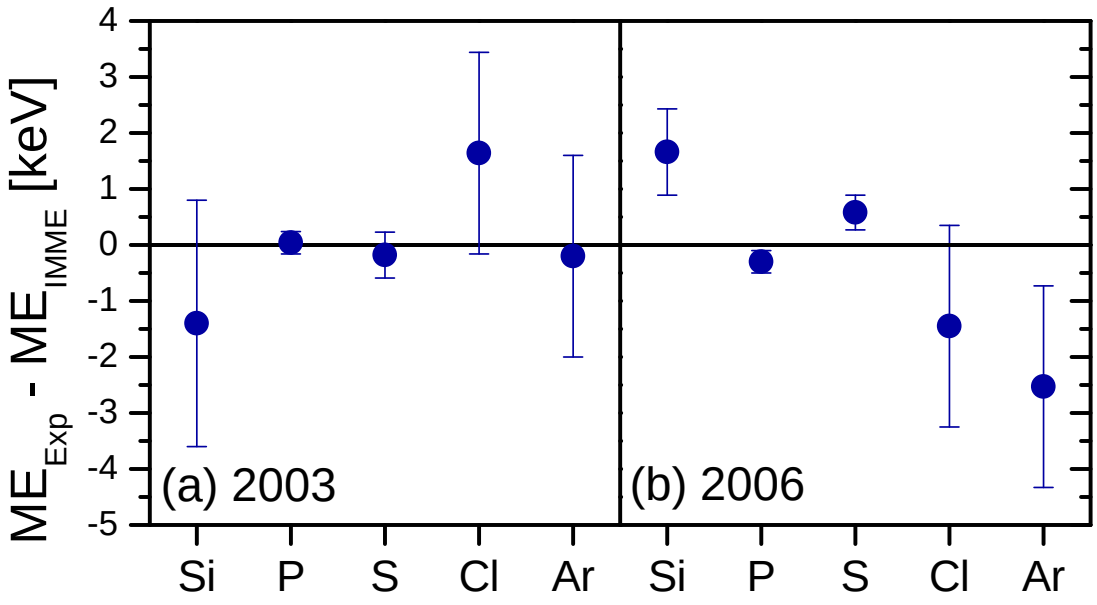

Figure 3.1: The difference between experimental and IMME-predicted mass excesses for A = 32. (a) The validation of the quadratic form of IMME in 2003 with the Penning trap mass measurement of ^{32}Ar [29]. (b) A remeasurement of the excitation energy of the first T = 2 state in ^{32}S [33] revealed a breakdown of the quadratic form. A quartic term $e = 0.53(15)$ keV was required to restore the fit to data.

form of IMME [28], and significant deviations have only been found for in light multiplets with unbound states (such as A = 9, T = 3/2). In addition to the fundamental importance of isospin symmetry, IMME is employed to predict unmeasured (or insufficiently precise) masses for e.g. mapping the proton-dripline for the rp-process [83] and to assist in the assignment of nuclear spin [84]. Providing the most precise test of IMME [28], the A = 32, T = 2 quintet has been the subject of considerable interest for the past decade. In 1999, IMME was applied to reduce the mass uncertainty of ^{32}Ar and enable a search of scalar currents [85]. Four years later, ISOLTRAP validated IMME and its prediction with a Penning trap mass measurement of ^{32}Ar; the residuals of the quadratic fit are displayed in Figure 3.1a. Shortly thereafter, a remeasurement of the energy of the first T = 2 excited state of ^{32}S [33] disagreed by 3 keV with the previously accepted value [86, 87]. This deviation led to a violation of the quadratic form of IMME (see Figure 3.1b) and required a quartic term

$e = 0.53(15)$ keV. The authors speculated on the importance of isospin mixing in ^{32}S or an erroneous ^{32}Si mass. An analysis of the data indicated that if ^{32}Si were more bound by 3 keV then the quadratic form would be restored. To clarify the value of the mass of ^{32}Si and to investigate the possible re-validation of IMME was the goal of the present mass measurement at LEBIT. In addition the masses of ^{33}Si, ^{31,34}P, and ^{32}S were measured at the same time.

3.1 Experimental Procedure

To produce the radioactive isotopes, a primary beam of ^{40}Ar at 140 MeV/u was reacted with a beryllium target. The A1900 fragment separator [43] separated out ^{32,33}Si and ^{34}P ions, and the resulting 94.5 MeV/u secondary beam was delivered to the gas stopping station. The gas cell was operated at 600 mbar with ultra high-purity (≈1 ppb) helium gas. Recall that the incident ions in the gas cell may charge exchange with residual impurities, thereby changing the final chemical form.

To determine what, if any, chemistry had occurred with the radioactive isotope, the

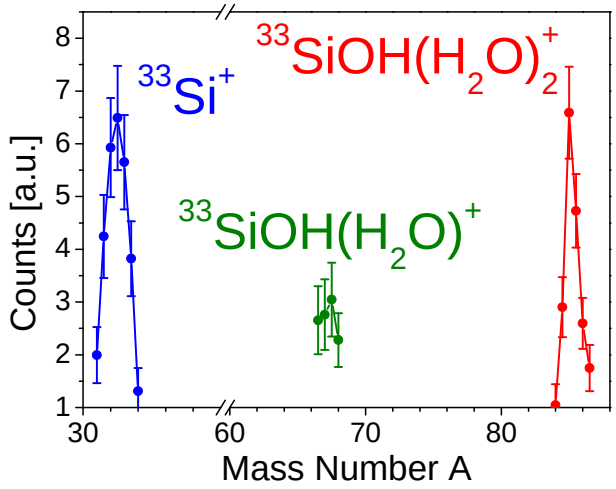

Figure 3.2: Measured β-activity of ^{33}Si ($T_{1/2} = 6$ s) after the RFQ ion guides. The chemistry for ^{32}Si was assumed to be identical but not measured due to its long half life, $T_{1/2} = 132$ yr.

extracted activity was measured with a silicon detector after the RFQ ion guides [55] as a function of the mass-to-charge state ratio, A/Q. As ^{32}Si possesses a long half life, $T_{1/2} = 132$ years, the chemistry of the silicon isotopes was measured only with $^{33}Si^+$ ions ($T_{1/2} = 6$ s), which was found to come as bare, singly charged ions. For $^{32}Si^+$, there was a strong beam of the isobaric contaminant O_2^+ at $A/Q = 32$, enough to reduce the signal strength in the Penning trap if not wholly hide it. Accordingly, a small quantity of water vapor was introduced into the gas cell to create radiomolecular ions. The remeasurement of the activity of ^{33}Si after the introduction of water is shown in Figure 3.2; peaks were seen at $A/Q = 33$, 68, 86 consistent with $^{33}Si^+$ and $^{33}SiOH(H_2O)_n^+$, n= 1, 2. For the best yield, $^{33}SiOH(H_2O)_2^+$ was selected. As ^{34}P was measured after the silicon isotopes and encountered residual water vapor in the gas cell, it was found to form a water adduct, too, $^{34}P(H_2O)_2^+$.

As an accuracy check, two stable masses were measured as well: ^{32}S and ^{31}P. ^{32}S is the $T_z = 0$ member of the A = 32, T = 2 quintet. Both masses had been previously measured with Penning trap mass spectrometry at Florida State University (FSU) with relative uncertainties below 10^{-9} [34, 88]. ^{32}S was found as an impurity in the helium gas and ionized by an RF discharge in the gas cell. In the presence of water, it formed HSO_2; after the water was depleted, its molecular form was SO_2. The ^{31}P ions were produced in the test ion source, operated in plasma-mode. A small reservoir was loaded with a solution of $^{31}P_2O_5$ and heated. $^{31}P^+$, $^{31}P_2^+$, and $H^{31}PO_2^+$ were identified in the Penning trap. Since O_2^+ was created as well and could be used as a reference ion to calibrate the magnetic field (see Section 2.4.3), $^{31}P^+$ was chosen as the chemical form with the closest A/Q to O_2^+.

After the ion guides, or the test ion source for the ^{31}P ions, the beam was directed to the beam cooler and buncher [5]. During the beam time, the cooler was filled with a neon buffer gas at about 1×10^{-2} mbar, which facilitated collision-induced dissociation (CID) of the radioactive molecular ions. One water molecule was stripped from the $SiOH(H_2O)_2^+$ and $^{34}P(H_2O)_2^+$, resulting in $SiOH(H_2O)^+$ and $^{34}P(H_2O)^+$

which were accumulated and bunched in the buncher, which was operated as usual with a helium buffer gas. The stable ions, on the other hand, were cooled with helium buffer gas in the cooler, and therefore CID was not used for the stable molecular ions. Next, the beam pulses were ejected from the buncher and sent to the Penning trap system [57, 58].

The time-of-flight mass filter and the dynamic capture process in the Penning trap ensured only the ion of interest and molecular isobars were trapped. All identified isobaric contaminant species were removed with a dipole excitation at their reduced cyclotron frequency to prevent shifts in the measured cyclotron frequency. Additionally, measurements were performed with a very small number of stored ions, on average less than one detected ion per cycle with the exception of the $^{31}P^+$ and O_2^+ measurements. The average number of detected $^{31}P^+$ and O_2^+ ions were five and six ions per cycle, respectively.

3.2 Results

The cyclotron frequency $2\pi\nu_c = q/m \cdot B$ and the statistical uncertainty were determined by fitting the resonance curve with the theoretical line shape [49], as shown for $^{32}SiOH(H_2O)^+$ in Figure 3.3. Other sources of systematic uncertainty will be discussed later. The first resonance for the silicon isotopes was taken with $T_{RF} = 500$ ms, and subsequent resonances were performed with $T_{RF} = 1$ s. Measurements for $^{34}P(H_2O)^+$ and $^{31}P^+$ were obtained with $T_{RF} = 500$ ms. Resonances of HSO_2^+ and SO_2^+ used a combination of $T_{RF} = 500$ ms and 1 s.

As discussed in Section 2.4.3, the primary experimental result is the ratio $R = \nu_c/\nu_{c,ref}$, where ν_c is the cyclotron frequency of the ion of interest and $\nu_{c,ref}$ that of the reference ion, linearly interpolated to the time of the measurement of ν_c. The reference ions were contaminant ions formed in the gas cell and extracted with the ion of interest for the radioactive and ^{32}S ions. For ^{31}P, the calibration ion, O_2^+, was a byproduct

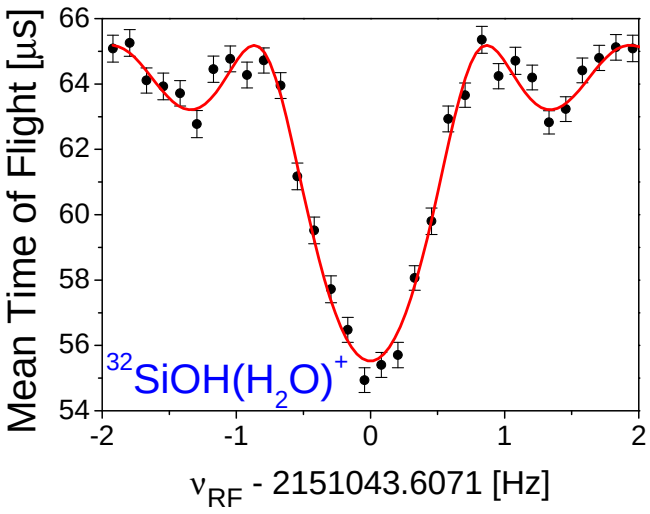

Figure 3.3: The mean time-of-flight as a function of the applied RF frequency in the Penning trap, ν_{RF}. The excitation time was $T_{RF} = 1$ s. The solid curve represents the result from fitting the theoretical line shape [49] to the data.

of the molecular dissociation of $^{31}P_2O_5$. The reference ions and the weighted average $\bar{R}$ of the individual frequencies are tabulated in Table 3.1.

3.2.1 Systematic Error Analysis

The experimental data was examined for evidence of systematic errors associated with nonlinear magnetic field effects, trapping field imperfections, relativistic effects, and frequency shifts arising from ion-ion interactions.

Magnetic field strength calibration: The magnetic field strength must be known to great accuracy and precision; nonlinear changes in the magnetic field are unaccounted for in the linear interpolation used to calculate the B at the time of the measurement of the ion of interest. The decay of the magnetic field and the impact of nonlinear effects on the cyclotron frequency have been thoroughly investigated [61]; so long as the time between reference measurements is less than 1.5 hours, the uncertainty in the measured cyclotron frequency was found to be $\Delta\nu_c/\nu_c = 2(1) \times 10^{-10}$. The statistical uncertainties of all measurements were one to two orders of

Isotope	Molecular Ion	A	Reference Ion	A_{ref}	N	$\bar{R}$	$\delta\bar{R}/\bar{R}$
^{32}Si	$^{32}SiOH(H_2O)^+$	67	$C_5H_7^+$	67	13	1.001 004 962 8(48)	4.8×10^{-9}
^{33}Si	$^{33}SiOH(H_2O)^+$	68	$^{13}C^{12}C_4H_7^+$	68	7	1.000 983 204(11)	1.1×10^{-8}
^{31}P	$^{31}P^+$	31	O_2^+	32	3	1.032 804 708 2(32)	3.1×10^{-9}
^{34}P	$^{34}P(H_2O)^+$	52	$C_4H_5^+$	53	5	1.020 293 195(17)	1.7×10^{-8}
^{32}S	$^{32}SO_2H^+$	65	CF_3^+	69	8	1.061 959 895 0(55)	5.2×10^{-9}
	$^{32}SO_2H^+$	65	$H_2CO_2F^+$	65	7	1.000 525 733 9(88)	8.8×10^{-9}
	$^{32}SO_2^+$	64	CF_3^+	69	3	1.078 692 991(10)	9.3×10^{-9}

Table 3.1: For each mass measured, the isotope is listed with its mass number, its molecular ion, the molecular ion's mass number, its reference ion and its mass number, the number of measurements N, the mean frequency ratio $\bar{R}$, and the relative uncertainty. The uncertainty includes both statistical and systematic uncertainties. The charge state of all ions was Q = 1, and so A/Q = A.

magnitude higher than this. In addition, the reference measurements were typically spaced less than an hour apart. Therefore, non-linear changes in the magnetic field were considered to be negligible.

Mass-dependent effects: Residual imperfections of the trapping field affect ion motion and may shift the measured cyclotron frequency. If the ion of interest and its reference are a mass doublet and undergo the same injection into the Penning trap, then their motion in the trap will be identical, and the effects cancel in the determination of the frequency ratio R. The reference ions should be chosen to have A/Q as close to that of the ion of interest as possible even though earlier studies have shown that mass-dependent effects at LEBIT affect the ratio less than $5(5) \times 10^{-10}/u$ [30]. Reference ions were chosen from the contaminants with A/Q as close as possible to that of the ion of interest although mass doublets could only be achieved for the silicon isotopes. The largest difference was between the $^{32}SO_2^+$ and CF_3^+, $\Delta A/Q = 5$ u. For all ratios measured, the uncertainty due to field imperfections were more than an order of magnitude less than the statistical uncertainty.

Relativistic effects: Relativistic mass shifts always occur and affect lighter masses, like $^{31}P^+$, more than heavier masses like $^{32}SiOH(H_2O)^+$. The cyclotron frequency should written as $2\pi\nu_c = q/\gamma m \cdot B$, where $\gamma = 1/\sqrt{1 - v^2/c^2}$ and m is the rest mass. The velocity v is proportional to the initial magnetron radius ρ_-^0. If the ion of interest and its reference are a mass doublet and have the same ρ_-^0, the Lorentz factor γ cancels in the calculation of the frequency ratio. The initial magnetron radius ρ_-^0 is a parameter in the theoretical line shape fit to the resonance data. Using the average value of ρ_-^0 for each ion, the relativistic shift was calculated for each ratio. The largest relativistic shift was found for the ratio of $^{31}P^+$ to O_2 ($\Delta A/Q = 1$ u). The average value of ρ_-^0 obtained was 1.047(14) mm for $^{31}P^+$ and 1.089(14) mm for O_2^+. The effect on the ratio was of order 2×10^{-10}, which was again insignificant compared to the statistical uncertainty.

Ion-ion interactions: To account for unidentified impurities, a so-called counting

rate analysis was performed. The cyclotron frequency was measured as a function of the number of stored ions; the observed cyclotron frequency was then linearly extrapolated to the value for one trapped ion. Significant frequency shifts were observed for the stable isotopes and for $^{33}SiOH(H_2O)^+$. The maximum ratio shift observed was 2.2×10^{-9} for the frequency ratio of $^{32}SO_2^+$ to CF_3^+. These measurements also suffered most from contamination, and for ^{32}S not all of which were identified during the measurement.

3.2.2 Comparison of Measured Mass Excesses to Literature Values

The ratios and uncertainties listed in Table 3.1 include the statistical and applicable systematic uncertainties. The masses of $^{32,33}Si$ and $^{31,34}P$ were determined from these ratios and the reference mass values taken from AME'03 [76]. The mass of ^{32}S was determined by another procedure since the measurement of HSO_2^+ was performed with two references ions simultaneously. That is, the measurement with CF_3^+ as the reference ion was not independent of the measurement with $H_2CO_2F^+$ as the reference ion. Instead of the normal procedure, the mass of ^{32}S was extracted from the individual ratios, and then the weighted mean was taken. Its mass excess, ME = Am_u - M, and the other mass excesses determined in this thesis are given in Table 3.2 and compared to mass values compiled in AME'03.

For the stable masses ^{32}S and ^{31}P, there is a deviation between LEBIT and AME'03 of order 1.0σ and 1.8σ respectively. However, since the publication of AME'03, more recent data has been published by the Florida State University (FSU) Penning trap mass spectrometry collaboration. The LEBIT mass values are in excellent agreement with the FSU values [34,88] (see Table 3.3), which were performed with a single ion technique, in which the cyclotron frequency was determined by measuring the signal induced by the ion motion, and achieved a precision of $\lesssim$1 eV. The authors of

Isotope	ME_{LEBIT} keV	$ME_{AME'03}$ keV	ΔME keV
^{32}Si	-24077.68(30)	-24080.86(77)[a]	3.18(83)
^{33}Si	-20514.30(70)	-20493(16)	-21(16)
^{31}P	-24440.53(09)	-24440.88(18)	0.35(20)
^{34}P	-24548.71(81)	-24558(5)	9(5)
^{32}S	-26015.34(32)	-26015.70(14)	0.36(35)

[a] Based solely on [89], ME(^{32}Si) = -24080.81(05) keV; authors later republished the value listed above [90]

Table 3.2: Experimentally determined mass excesses and a comparison to literature values. $\Delta ME = ME_{LEBIT}$ - $ME_{AME'03}$ is the difference between the LEBIT and AME'03 values.

Isotope	ME_{LEBIT} keV	ME_{FSU} keV	ΔME keV
^{31}P	-24440.53(09)	-24440.541(1)	0.01(09)
^{32}S	-26015.34(32)	-26015.534(1)	0.19(32)

Table 3.3: Experimentally determined mass excesses and a comparison to mass values obtained by Penning trap mass spectrometry at Florida State University (FSU) [34, 88]. $\Delta ME = ME_{LEBIT}$ - ME_{FSU} is the difference between the LEBIT and FSU values. N.B. $ME_{FSU} \neq ME_{AME}$

AME'03, in preparation for the Atomic Mass Evaluation of 2013, released a preview earlier this year (called AME'11 hereafter) [91], which includes the Penning trap mass measurements.

Among the radioactive isotopes measured here, the AME'03 and the LEBIT values agree on the masses of ^{33}Si and ^{34}P. Previously, the mass of ^{33}Si had been determined by the transfer reactions ^{34}S(^{14}C,^{17}O) [92] and ^{36}S(^{11}B,^{14}N) [93] and by delayed β-γ coincidence techniques [94]. Both techniques result in uncertainties in the tens of keV, while the present uncertainty is more than 20 times smaller. In the case of ^{34}P, a (d,α) reaction was used to determine the mass value with an uncertainty of a few keV [76]; the LEBIT measurement reduces the uncertainty by a factor of six. The measurements of this work essentially determine the value compiled in AME'11 [91]: ME(^{33}Si) = -20514.326(699) keV and ME(^{34}P) = -24548.699(810) keV.

The only significant discrepancy between LEBIT and literature mass values is for ^{32}Si. Originally the mass value of -24080.81(05) keV was based upon the AVOGADRO mass measurement, a series of (n,γ) reactions starting with ^{28}Si and ending at ^{32}Si [89]. The authors themselves later published another value with a larger uncertainty -24080.86(77) [90] without clarification. The AVOGADRO neutron separation energies, S_n, and mass values were recalculated using the FSU mass excess value for ^{28}Si [88] and the AME'11 value for the neutron [91] (see Appendix A). The recalculated mass excess of ^{32}Si is -24080.87(77) keV, where the undocumented uncertainty in [90] is kept; the 3 keV discrepancy persists. The AVOGADRO S_n values for ^{30}Si and ^{31}Si agree with the AME'11 compilation; however, there is significant disagreement for the values of ^{29}Si and ^{32}Si. The latter results from the adoption of the LEBIT mass value by the authors of AME'11. Given that the chain of masses is now anchored by direct mass measurements at ^{28}Si [88] and ^{32}Si (this work), there must be an erroneous value for a neutron separation energy in the chain from $^{29-32}$Si. The LEBIT measurement agrees with an older (t,p) study published only as a conference abstract, ME = -24078.0(1.3) keV [95].

Nuc.	T_z	ME_{gs} [keV]	$E_x(T=2)$ [keV]	$ME_{T=2}$ [keV]
^{32}Si	2	-24077.68(30)[a] -24080.87(77)[b]	0	-24077.68(30) -24080.87(77)
^{32}P	1	-24304.874(40)[c]	5072.44(06)[d]	-19232.43(07)
^{32}S	0	-26015.534(1)[c]	12047.98(08)[e]	-13967.55(08)
^{32}Cl	-1	-13334.6(6)[f] -13335.115(939)[c]	5046.3(4)[g]	-8288.3(7) -8288.8(1.0)
^{32}Ar	-2	-2200.37(1.77)[c]	0	-2200.37(1.77)

[a] This work
[b] ME of ^{28}Si from [91] and the S_n of $^{29-32}$Si from [90]
[c] [91]
[d] [87]
[e] Weighted average of [33, 96]
[f] Weighted average of [97, 98]
[g] [99]

Table 3.4: The mass excesses used to fit IMME: the ground state mass excess, the excited energy of the first T = 2 state, and the mass excess of the first T = 2 state.

3.3 Impact of the present ^{32}Si mass measurement on IMME

To test the quadratic form of IMME, a parabola was fit to the experimentally determined mass excesses of the A = 32, T = 2 quintet given in Table 3.4. Penning trap mass measurements supplied the ground state energy values for ^{32}S and ^{32}Ar. The ground state mass of ^{32}P was determined by the weighted average of the Penning trap mass measurements of ^{31}P from this work and [88] and the neutron separation energy of ^{32}P in [100]. Values for the excitation energies of the first T = 2 state in ^{32}P, ^{32}S, and ^{32}Cl were taken from the most recent and most precise values [33, 87, 99]. Two values are listed for the mass of ^{32}Si: one from this work and the other from combining the AVOGADRO neutron separation energies [90] with the mass of ^{28}Si [91]. Two values are also provided for the ground state mass of ^{32}Cl: the weighted mean of two recent and mutually consistent measurements [97, 98] and AME'11. As a result,

	Data Set			
	a	b	c	d
ME(^{32}Si) [keV]	-24077.68(30)[a]	-24077.68(30)[a]	-24080.87(77)[b]	-24080.87(77)[b]
ME(^{32}Cl) [keV]	-13334.6(6)[c]	-13335.115(939)[d]	-13334.6(6)[c]	-13335.115(939)[d]

[a] This work
[b] ME of ^{28}Si from [91] and the S_n of $^{29-32}$Si from [90]
[c] Weighted average of [97, 98]
[d] [91]

Table 3.5: The four data sets a, b, c, and d used to test IMME: two values were taken each for the ground state energies of ^{32}Si and ^{32}Cl. Mass excesses are given in keV.

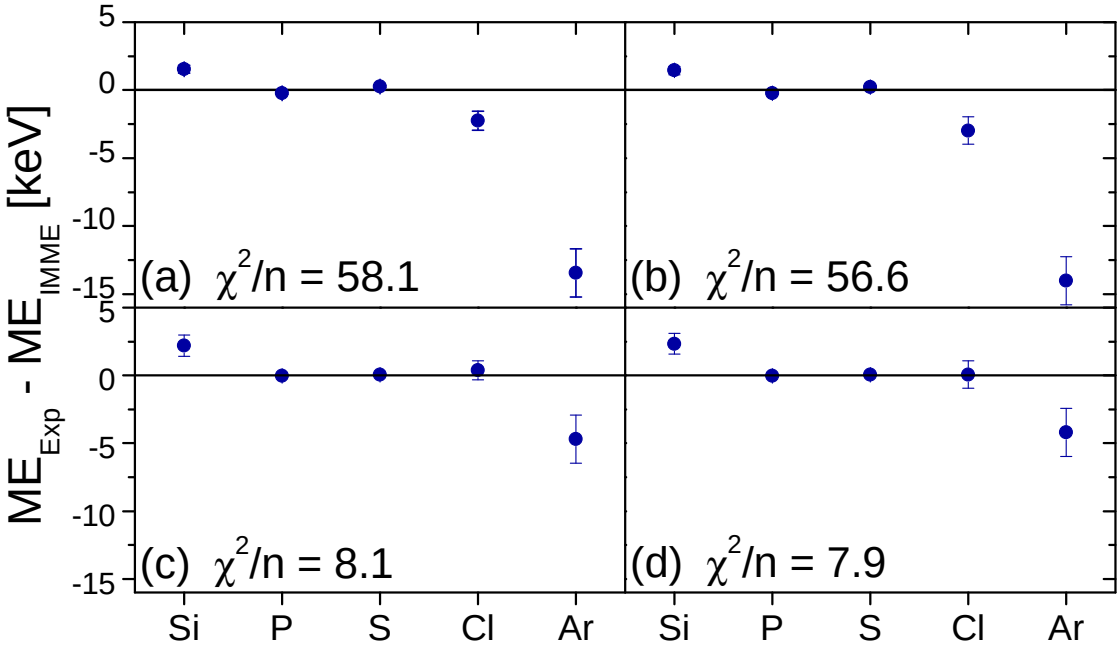

Figure 3.4: Fit of the quadratic form of IMME to data with the four different data sets indicated in Table 3.4. Rows result from different mass values of ^{32}Si, columns from different mass values of ^{32}Cl.

four data sets, described in Table 3.5 were fit with IMME. Appendix A reviews the experimental data in greater detail.

Residuals from the parabolic fit of IMME to the four data sets can be seen in Figure 3.4. Table 3.6 provides the coefficients and the χ^2/n for each fit. The 3 keV reduction in binding energy in ^{32}Si, as measured at LEBIT, exacerbates the breakdown of the quadratic form of IMME, $\chi^2/n > 56$, where n is the degrees of freedom (data sets (a) and (b) in Figures 3.4a,b); the shift in fact goes in the opposite direction needed for

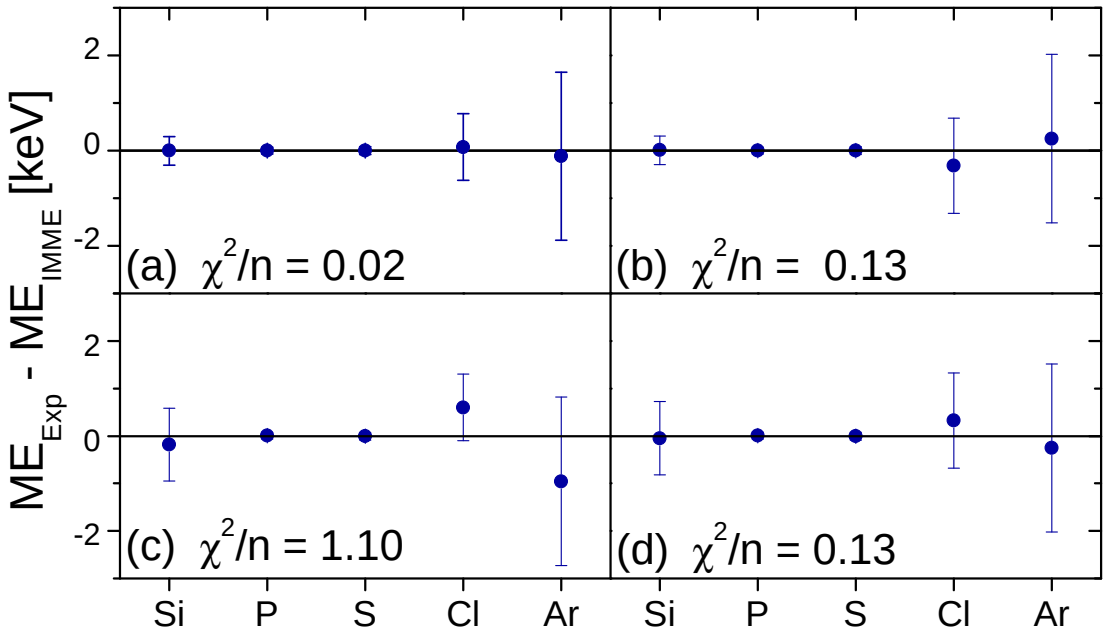

Figure 3.5: Fit of the cubic form of IMME to data with the four different data sets indicated in Table 3.4. Rows result from different mass values of ^{32}Si, columns from different mass values of ^{32}Cl.

a quadratic IMME. The quadratic fits to data sets with the AVOGADRO mass value of ^{32}Si (data sets (c) and (d) in Figures 3.4c,d) are not as bad, having $\chi^2/n \approx 8$. The different mass values for ^{32}Cl do not make an appreciable difference in the fitting of a quadratic IMME to the data. None of the data sets can be fitted with a parabola, indicating a departure from the quadratic IMME, and all require a significant cubic coefficient. Figure 3.5 presents the residuals from a cubic fit to data; the coefficients and χ^2/n are listed in Table 3.6. The χ^2/n is of order 1 or smaller, indicating an excellent fit; indeed, the smallest χ^2/n is found for data set (a), $\chi^2/n = 0.02$. Again, there is no significant difference between either value for the ground state energy of ^{32}Cl. On the other hand, the mass value of ^{32}Si has an appreciable effect on the size of the cubic term. Data sets (a) and (b), which relied on the direct mass measurement of this work, results in $d = 0.89(1)$ and $0.90(3)$ keV respectively. Fits to data sets (c) and (d) produces a cubic coefficient a factor of two smaller, $0.48(13)$ and $0.49(05)$ keV respectively. An earlier discussion [98] had demonstrated that a 300 eV shift in

the binding energy of ^{32}P substantially impacts the quality of the fit and the size of the cubic term. In contrast, the 500 eV difference of the two mass values for ^{32}Cl considered here has a negligible effect.

3.3.1 Possible Reasons for a Non-zero d Coefficient

The constant term in IMME corresponds to the isoscalar Coulomb intraction, the linear term to the isovector interaction, and the quadratic term to the isotensor interaction. I prefer more intuitive arguments in [82] based on an inert core with four valence nucleons. The a coefficient corresponds to the energy associated with the core. The b coefficient is related to the average interaction between a valence nucleon and the core. The c coefficient reflects the interaction between the valence nucleons. The isospin lowering operator converts a neutron to a proton. The newly charged nucleon experiences a Coulomb interaction with the core; since the interaction between the core and any valence proton is the same to first order, the energy associated with this interaction is constant across the multiplet. As the number of protons increases, the electric repulsion between the valence protons increases.

A non-zero cubic (or quartic) term may indicate higher-order Coulomb effects, charge-dependent nuclear interactions, many-body interactions, or isospin mixing of the isobaric analog state with neighboring states. Several authors have noted that the higher-order perturbations from the Coulomb interaction should be mostly absorbed by the a, b, and c coefficients [79–82]; however, here a and b coefficients do not change substantially between the quadratic and cubic fits. For data sets (a), (b), and (c), the c coefficient changes on the order of 1.5 keV between the quadratic and cubic fits. For data set (d), the change in c is insignificant. Studies with a simple, non-perturbative model [79] and a second-order perturbation calculation [80] indicate that a non-zero cubic term arises from isospin mixing of the lowest T = 2 state with neighboring T = 1 states for interior members of the quintet: ^{32}P, ^{32}S, and ^{32}Cl. Indeed, from the estimates in [79], one expects that IMME should hold to $d \approx 1$ keV, in accordance

Data Set	set a_{quad}	set a_{cubic}	set b_{quad}	set b_{cubic}	set c_{quad}	set c_{cubic}	set d_{quad}	set d_{cubic}
a	-13967.80(58)	-13967.55(1)	-13967.78(58)	-13967.55(3)	-13967.59(22)	-13967.54(8)	-13967.60(22)	-13967.55(3)
b	-5473.07(1.4)	-5472.92(2)	-5473.19(1.4)	-5472.88(7)	-5471.85(60)	-5472.25(25)	-5471.75(64)	-5472.15(9)
c	208.68(99)	207.15(2)	208.76(1.0)	207.10(7)	207.06(56)	206.87(21)	206.98(60)	206.77(8)
d		0.89(1)		0.90(3)		0.48(13)		0.49(5)
χ^2/n	58.15	0.02	56.56	0.13	8.09	1.10	7.86	0.13

Table 3.6: The coefficients and the χ^2/n of the quadratic and cubic forms of IMME to the A = 32, T = 2 quintet for different values of the ground state energies of ^{32}Si and ^{32}Cl (see Table 3.4).

with experiment. Unfortunately, the isospins of too few states in ^{32}P, ^{32}S, or ^{32}Cl have been determined empirically for a fruitful discussion on which states contribute and to what degree.

Recently, the first detailed calculation for isospin mixing in the A = 32, T = 2 quintet were performed using the USDB (universal *sd*-shell) interaction [101]; they included charge-dependent and charge-symmetry-breaking interactions. According to these calculations, a J^π, $T = 0^+$, 1 state in ^{32}Cl just below the state of interest is largely responsible for the deviation from the quadratic form of IMME. To a lesser extent, two T = 1 states in ^{32}P mix with its T = 2 state and also contribute to the non-zero cubic coefficient. The sum of these effects is $d = 0.28$ keV, far smaller than observed in experiment. The authors also predict that isospin mixing of the T = 2 and T = 1 states in ^{32}Cl results in the isospin-forbidden proton decay to T = 1/2 states in ^{31}S and the isospin correction $\delta_c = 1.8\%$ for the ft value of the superallowed β-decay of ^{32}Ar.

The last possibility considered here is that of an erroneous mass value. The masses of three members of the A = 32, T = 2 quintet have been measured with high precision Penning trap mass spectrometry: ^{32}Si (this work), ^{32}S (this work and [34], and ^{32}Ar [29]. These measurements are largely responsible for making the A = 32, T = 2 quintet the most precisely known isobaric multiplet [28], and each deviated from the previously accepted mass value. The mass of the ground state of the other two members, ^{32}P and ^{32}Cl, have been measured indirectly. ^{32}P was determined by adding the neutron separation energy to to the mass value of ^{31}P, which was measured here and at FSU [88] by Penning trap mass spectrometry. ^{32}Cl was similarly determined from the proton separation energy and the mass value of ^{31}S. Nonetheless, as this work demonstrates, neutron separation energies may be wrong. An erroneous mass value may explain why the χ^2/n values for the cubic fits of data sets (a), (b), and (d) are 0.13 or smaller. It is imperative to measure the masses of ^{32}P and ^{32}Cl directly to confirm the neutron and proton separation energies, the breakdown of the

quadratic form of IMME, and the size of the cubic term.

Chapter 4

Motivation for and Foundation of Stored Waveform Inverse Fourier Transform

During the mass measurement of ^{32}S, several contaminant species were trapped simultaneously with the ^{32}S ions, and their presence shifted the measured cyclotron frequency due to ion-ion interactions [70]. Nearly a day of running time cumulatively was spent on identifying the contaminant species one by one. The identified ions were each removed by dipolar excitation [46, 47] at their reduced cyclotron frequencies (Equation 2.4); however, two other contaminants were detected but were present at too low a level for timely identification. Thus significant time was lost to contaminant "hunting" which would otherwise been spent on the mass measurements. Furthermore, the chemistry and therefore the contaminants depend on the beam intensity and the purity of the helium gas and in principle could change over time. A more optimal use of beam time would be to specify mass bands around the radioactive ion to be ejected from the Penning trap and, hence, eliminate the need to identify each contaminant.

The question becomes how best to generate a signal which can be applied with a waveform generator for an arbitrary excitation in frequency space. The solution is

the Stored Waveform Inverse Fourier Transform (SWIFT) technique [51, 102–105]. SWIFT was designed for frequency-selective excitations used in Fourier transform ion cyclotron resonance (FT-ICR) [106] and Fourier transform nuclear magnetic resonance (FT-NMR) spectrometry [51]. FT-NMR is the selection and manipulation of the nuclear spin by its Larmor frequency. FT-ICR requires moving an ion from its initial radius and/or phase to a final radius and/or phase using its cyclotron frequency. For dipole excitations, the final radius and phase are linearly related to the excitation strength, thus the inverse Fourier transform is the appropriate tool to transform the excitation from the frequency domain into the time domain. (A brief overview of the mathematical properties of Fourier transforms is presented in Appendix B, in particular those important for SWIFT.)

4.1 Broadband excitation

At first glance, SWIFT appears simple to implement: define the desired excitation spectrum and take the inverse Fourier transform. Let's take for example a simultaneous uniform excitation of a frequency band, which by application of Equation 2.4 corresponds to a mass band. The discrete rectangular amplitude spectrum in frequency space F_k shown in Figure 4.1a was generated for $N = 1028$ points as follows

$$F_k = \begin{cases} 0 & \text{if } 0 \leq k < \frac{N}{8} \\ 1 & \text{if } \frac{N}{8} \leq k < \frac{7N}{8} \\ 0 & \text{if } \frac{7N}{8} \leq k < N \end{cases} \tag{4.1}$$

The real part of the inverse Fourier transform of Equation 4.1 is shown in Figure 4.1b.

Two drawbacks arise for this time-domain signal. First, the large difference between the highest and lowest non-zero amplitudes, i.e. the dynamic range, may result in distortion of the lower-amplitude section of the signal when digitized for use with a

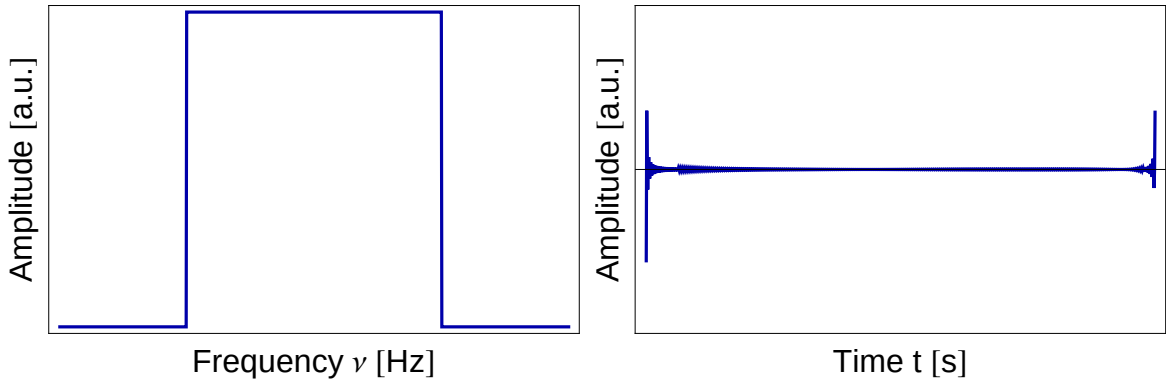

(a) In the frequency domain (b) In the time domain

Figure 4.1: (4.1a): A rectangular or uniform amplitude spectrum in frequency space created with 1028 points. (4.1b) Its inverse Fourier transform, a sharply peaked high amplitude sinc envelope.

programmable waveform generator. Second, the power is concentrated at the beginning and end of the excitation time and is near zero otherwise. Phase modulation is the key to a power distribution which is well suited for the programmable waveform generator.

4.2 Optimal phase modulation

The time-domain signal in Figure 4.1 results from the phase coherence of the frequency signal $F(\nu)$. Cosine functions, the real part of the Fourier transform, with constant phase add constructively near time $t = 0$ and destructively at larger t. The effect, illustrated in Figure 4.2, is exacerbated as the frequency signal is broadened. Phase modulation of the frequency signal $F(k)$ destroys the phase coherence and achieves a more optimal time-domain signal, in which the power is distributed evenly over the excitation time.

While the simplest modulation, a linear phase modulation only serves to shift the SWIFT signal in time without altering the signal shape (see the translation property B.7); Figure 4.3, top, illustrates the shift. Any nonlinear phase modulation reduces the dynamic range of the time-domain signal as was first noted in [102]. It was later

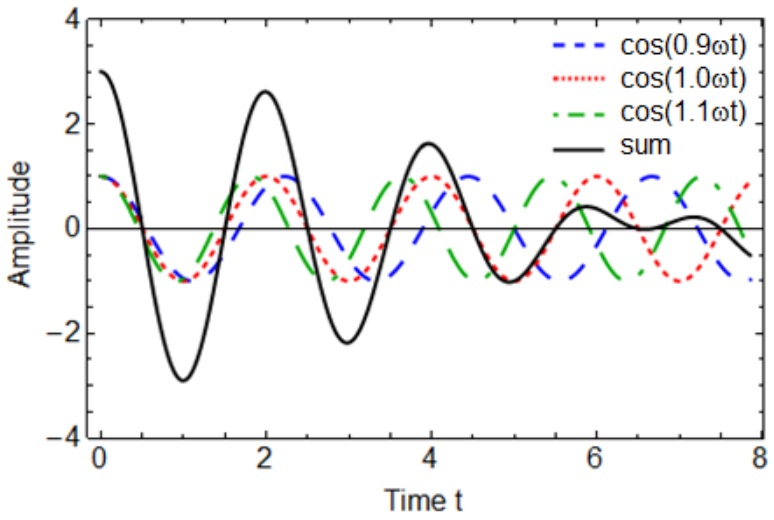

Figure 4.2: Red (dotted), blue (short dashed), and green (long dashed) curves are cosine functions with similar frequencies (ν, 0.9ν, and 1.1ν respectively) and the same phase. The sum of the colored curves is the black (solid) curve. Near $t = 0$, the functions add constructively, leading to a large amplitude. At larger t, the functions are no longer in phase and destructively interfere.

developed into a general algorithm for determining optimal phase modulation in [103].

The argument for the phase modulation scheme in [103, 107] is based on the translation property of Fourier transforms. A time-domain waveform constructed from a frequency signal whose phase depends linearly on frequency can be thought of as a "wave packet"; its power is concentrated in a time interval whose center is determined by the slope of the phase function. If the frequency spectrum is divided into two segments, whose power spectra (square of the magnitude) is equal but whose phase spectral slope differs, then the time-domain waveform is the superposition of two wave packets separated in time. Should the slopes be sufficiently different, the wave packets do not overlap, and the maximum time-domain amplitude is reduced by a factor of two. Pursuing this argument, one may divide the frequency spectrum into many segments of equal power spectral area and appropriately choose the phase spectral slope for successive segments such that the successive wave packets just overlap. In this manner, a uniform distribution of power across the excitation time is achieved. For rectangular excitation profiles, such as SWIFT, the optimal phase modulation

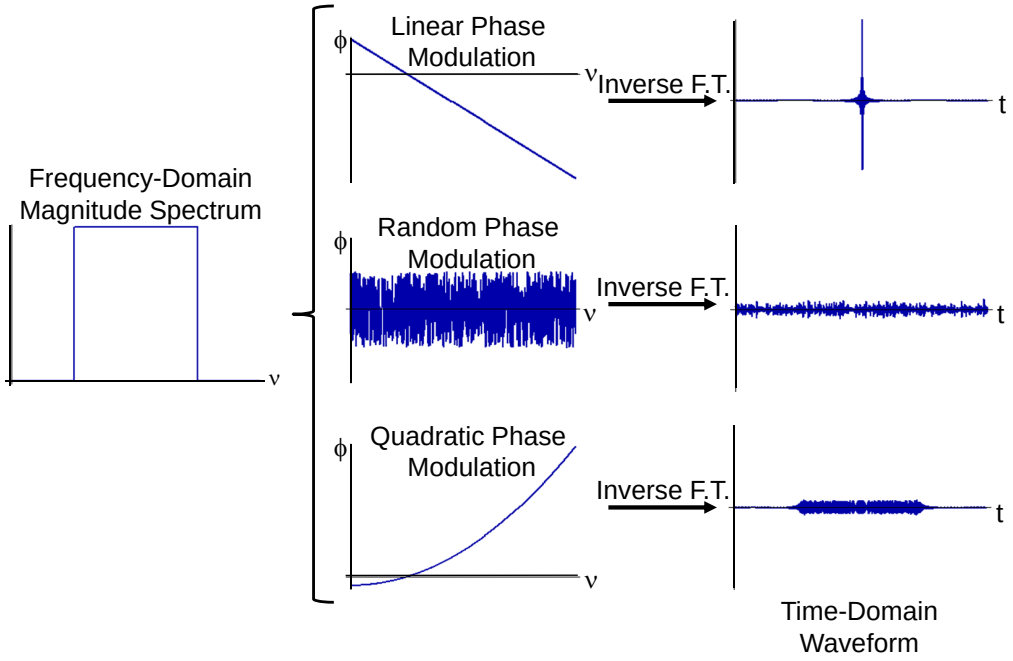

Figure 4.3: Comparison of three choices of the phase function ϕ_k (middle column). The corresponding SWIFT time-domain waveforms (right column) were calculated from the phase function and the rectangular frequency amplitude spectrum (left column). A linear phase function (top row) temporally shifts power to the center of the SWIFT waveform. A random phase function (center row) evenly distributes power over the excitation period. A quadratic phase function (bottom row) centers and distributes the time-domain power; the dynamic range is reduced; and, the time-domain amplitude is near zero at the beginning and end of the SWIFT waveform which reduces distortion.

reduces to a quadratic phase function. As the quadratic term is increased, the power spreads out.

The quadratic phase function may be written as

$$\phi_k = A(k - k_i) + \frac{B}{2}(k - k_i)^2 \text{ for } 0 \leq k < N \tag{4.2}$$

where k_i is the first frequency-domain point for which the excitation amplitude is nonzero. In this work, the parameters A and B were taken from [102], $A = \pi/2$ and $B = -\pi/(k_f - k_i)$, where k_f is the last frequency-domain point for which the excitation

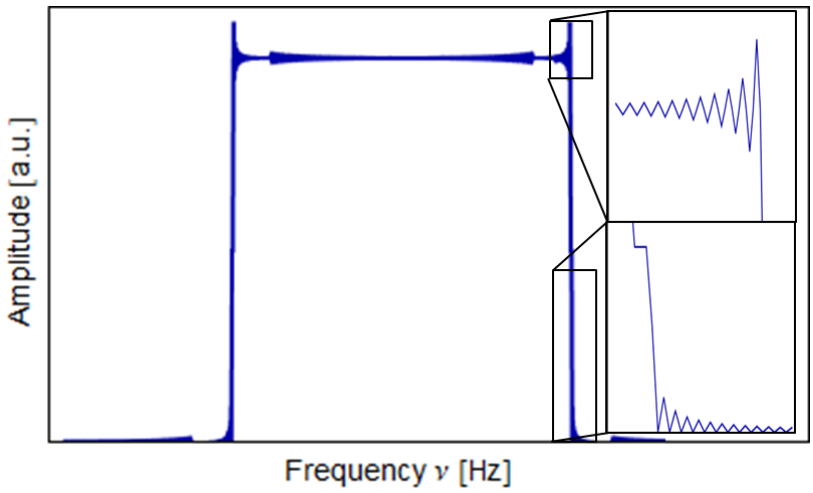

Figure 4.4: The details of the frequency-space signal are obtained by zero-filling the time-domain excitation and performing a forward Fourier transform. Gibb's oscillations and power leakage occur at discontinuities in the user-defined signal. Power leakage can undesirably excite ions outside of the defined mass band.

amplitude is nonzero. The power was concentrated over half the excitation time T, centered at $T/2$, and reduced in magnitude compared to a constant or linear phase modulation. The quadratic phase function is compared to a linear and a random phase functions in Figure 4.3. A phase spectrum which alternates randomly between $\pi/2$ and $-\pi/2$ was found to reduce the dynamic range by several orders of magnitude compared to constant or linear phase modulation [108]; however, the phase discontinuities and the truncation of the time-domain waveform can cause significant distortion.

4.3 Signal distortion

To examine the frequency spectrum of a particular excitation scheme, one "zero fills" the time-domain signal before performing the Fourier transform [107]. The typical zero fill doubles the number of points in a signal by adding $N/2$ zeroes to the beginning and end of the signal. By doubling the frequency resolution, it permits examination of the frequency signal not only at the originally defined points but also in between them. The result is shown in Figure 4.4. Two types of distortion can be seen: "wiggles" and magnitude "leakage" from high to zero amplitude segments. At discontinuities

in the original signal, the observed signal over- and undershoots, a phenomenon first explained by J. Willard Gibbs (see pp. 73-74 in [109]). A sharp corner or jump cannot be perfectly reproduced by a finite Fourier series. For a piecewise continuous function, its Fourier series converges to the function at every point except at a discontinuity. There, Dirichlet's theorem [109] states that the limit converges to the average of the values of the function on either side of the jump. Where the maximum overshoot occurs depends on the number of terms in the Fourier series; as the number of terms increases, the maximum overshoot moves closer to the discontinuity.

The power leakage leads to excitations outside of the desired mass band; however, at LEBIT, the radioactive ion must not be disturbed by the cleaning process. Gibb's oscillations can be minimized by a window or apodization function, $w(t)$ or w_k for continuous and discrete functions respectively. (Apodize is taken from the Greek word apod, meaning "to remove the feet" in reference to the side lobes or power leakage.) As the process is widely used not only in signal processing but also optics and radioastronomy, many apodization functions have been studied [109]. They differ by how quickly the function falls to zero and the size of the side lobes; and, they are often tailored to the specific use. Guan describes another method [105, 107], which smooths the original frequency (amplitude) spectrum before phase modulation and the inverse Fourier transform. The suggested apodization in [102], referred to in this work as the "quarter-wave sine" function, is given by

$$w_k = \begin{cases} +\sin(2\pi k/N) & \text{if } 0 \leq k \leq \frac{N}{8} \\ 1 & \text{if } \frac{N}{8} \leq k \leq \frac{7N}{8} \\ -\sin(2\pi k/N) & \text{if } \frac{7N}{8} \leq k \leq N \end{cases} \tag{4.3}$$

and was applied before the inverse Fourier transform. The Hann or Hanning window

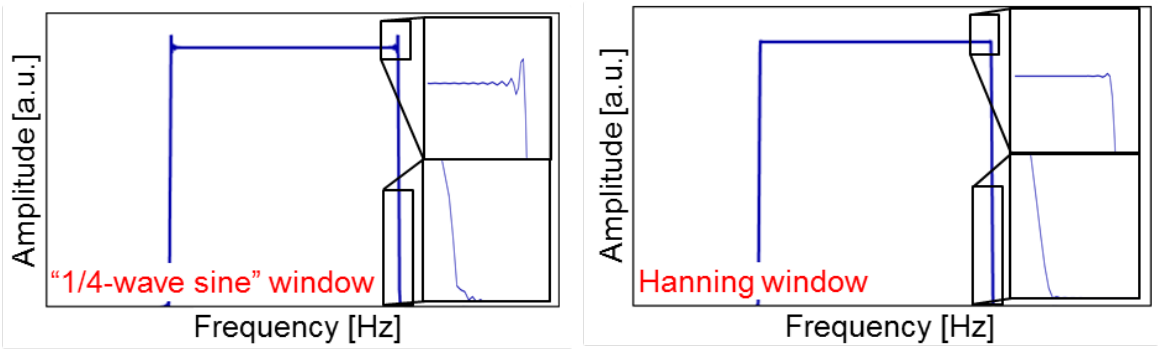

(a) "Quarter-wave sine" window function (b) Hanning window function

Figure 4.5: A comparison of frequency spectrum obtained by the Fourier transform of a rectangular excitation in the time domain multiplied by different window or apodization functions. Notice the side lobes are substantially reduced by the apodization functions, the "quarter-wave sine" window function [102] (left) and the Hanning window (right).

function is also common to digital signal processing,

$$w_k = \sin^2\left(\frac{\pi k}{N}\right) \text{ for } 0 \leq k < N. \tag{4.4}$$

It reaches zero so that the side lobes roll off at about 18 dB per octave. The effect of both apodization functions can be seen in Figure 4.5. The Gibb's oscillations are suppressed although not eliminated. The drawback of apodization is reduced amplitude near the edges of the excitation profile, which may reduce the efficacy of cleaning masses whose reduced cyclotron frequency $\nu_+ = \omega_+/2\pi$ lie at the edges of the cleaning band. However, suppressing power leakage *outside* the excitation band, to avoid possible ejection of the radioactive ion, is preferred to uniformity *inside* the excitation band.

4.4 SWIFT-based cleaning at LEBIT

To clean contaminant species from the Penning trap requires modifications to the rectangular excitation scheme discussed above and indicated in Figure 4.1a. To clean

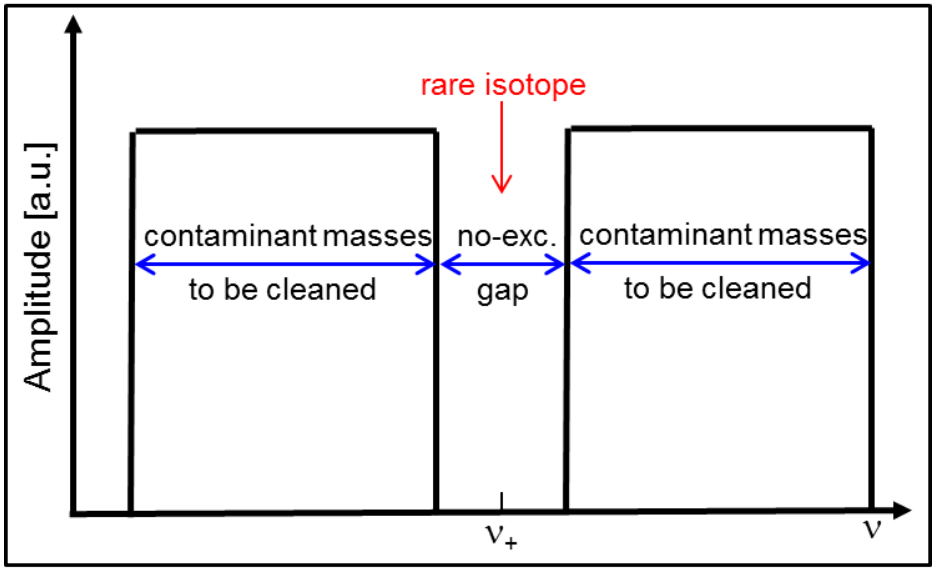

Figure 4.6: The desired excitation profile for beam purification at LEBIT. Two uniform rectangular excitations are separated by a gap of non-excitation. Ions whose ν_+ lay within the excitation bands are cleaned from the Penning trap. The ν_+ of the rare isotope is within the gap to prevent driving its reduced cyclotron radius.

mass or frequency bands around the ion of interest, a signal consisting of two rectangular excitations separated by a gap of non-excitation is required as sketched in Figure 4.6. Ions whose ν_+ are within the excitation bands are excited and driven from the Penning trap. The gap is centered on the ν_+ of the ion of interest in order to preserve its initial state. With SWIFT-based cleaning, only the reduced cyclotron frequency of the rare isotope must be known, and the no-excitation gap should exceed the uncertainty of ν_+.

Once the desired cleaning signal is defined, it is passed through the SWIFT signal preparation process described above: phase modulation, apodization, and the inverse Fourier transformation. Figure 4.7 shows how the quadratic phase modulation leads to an optimal power distribution. To illustrate the power leakage into the no-excitation gap, Figure 4.8 compares the cleaning excitation without apodization to excitations which use either the quarter-wave sine or the Hanning window functions. As was mentioned earlier, the prevention of undesired excitation of the ion of interest takes priority over uniformity in the excitation bands. The Hanning window function was

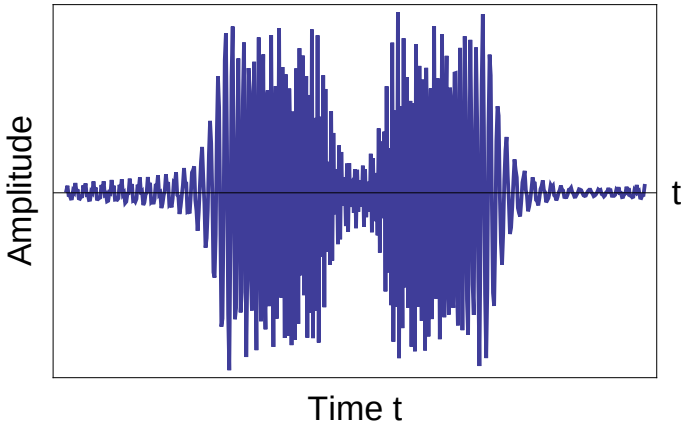

Figure 4.7: The time-domain waveform of the frequency excitation shown in Figure 4.6 with quadratic phase modulation. The power is zero at the edges of the excitation time and relatively evenly distributed through the middle. The dynamic range is smaller than if the phase modulation had been constant or linear.

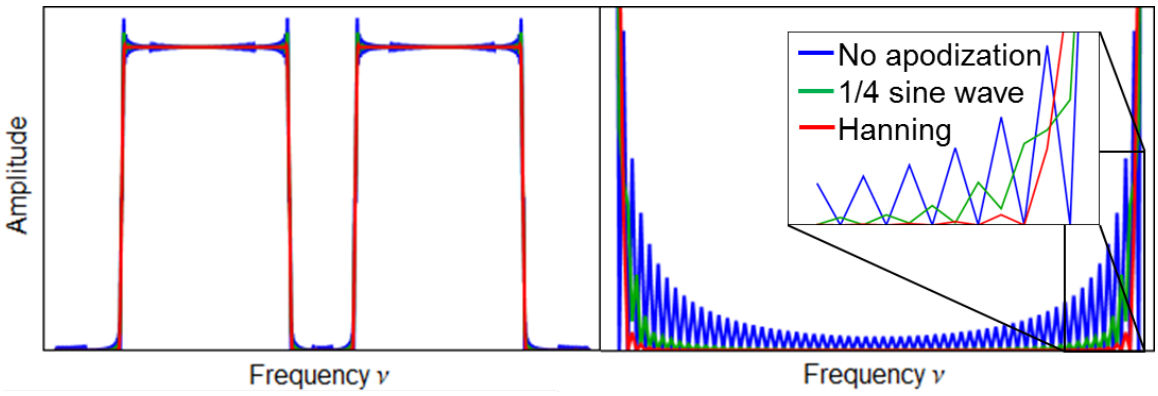

Figure 4.8: Comparison in frequency-space of apodized cleaning excitations. (a) The entire excitation profile is shown. (b) Closer examination of signal strength in the gap. The inset compares the size of the first side lobe. Apodization with the quarter-wave sine gives less Gibb's oscillations than the excitation without apodization. Use of the Hanning window minimizes the Gibb's oscillations and falls to zero amplitude fastest in the gap. Since the gap is centered on the rare isotope's ν_+, signal power in the gap leads to the undesired excitation of the radioactive ion.

found to best suppresses the Gibb's oscillations and featured the most well-defined gap.

Chapter 5

Implementation of SWIFT Cleaning at LEBIT

The mass measurement of ^{32}S which was heavily contaminated by molecular isobars provides a useful example for the motivation for the SWIFT technique. Other beam purification methods at LEBIT removed contaminant ions with other A/Q values. An attempt was made to identify each isobaric contaminant, and the identified ions were removed from the Penning trap by dipole excitation at the appropriate reduced cyclotron frequency ν_+, which drove each contaminant ion to a radius so large that the ion struck a trap electrode. Sidebands in the frequency spectrum, resulting from the finite cleaning time, were suppressed by amplitude modulation (AM) of the RF signals with a Gaussian window function. Table 5.1 lists the contaminants identified by dipole TOF resonance during the mass measurement of HSO_2^+ and SO_2^+ as well as two other examples of contamination during found during beam times. The reduced cyclotron frequency of molecular contaminant ions is typically a few kHz away from the ion of interest, and the difference increases the more exotic the ion of interest simply because the binding energy of radioactive nuclei decrease as one approaches the driplines.

The stored waveform inverse Fourier transform (SWIFT) technique circumvents

HSO_2^+	$\Delta\nu_+$ [Hz]	SO_2^+	$\Delta\nu_+$ [Hz]	$^{64}Fe^{2+}$	$\Delta\nu_+$ [Hz]	$^{26}Si^+$	$\Delta\nu_+$
$H_2CO_2F^+$	-1167	CNF_2^+	-1338	O_2^+	-2709	CN^+	-2290
$H_3C_2F_2^+$	-1726	$C_3N_2^+$	-1559	CH_4O^+	-7825	$C_2H_2^+$	-4969
		$H_2C_2F_2^+$	-1781	$C_2H_8^+$	-12931		

Table 5.1: A list of contaminants identified during different mass measurements and the separation of their ν_+ from the ion of interest. Top row indicates the ion of interest. During the measurement of HSO_2^+, two other contaminants were detected but were too weak to identify.

the need for individual contaminant identification by using a broadband excitation to drive out simultaneously a range of masses. The diagram in Figure 5.1 depicts the excitation profile labeled with the four parameters needed to generate it. This chapter will describe the implementation of SWIFT at LEBIT. To be considered successful, the SWIFT scheme must:

- Provide high resolution cleaning at short cleaning times, $T_{clean} \approx 30$ ms
- Excite a bandwidth of $b_L + b_R = 30$ kHz with a gap of non-excitation $g = 1000$ Hz centered at ν_+
- Suppress signal in the gap by a factor of 1000 compared to the amplitude of the excitation bands

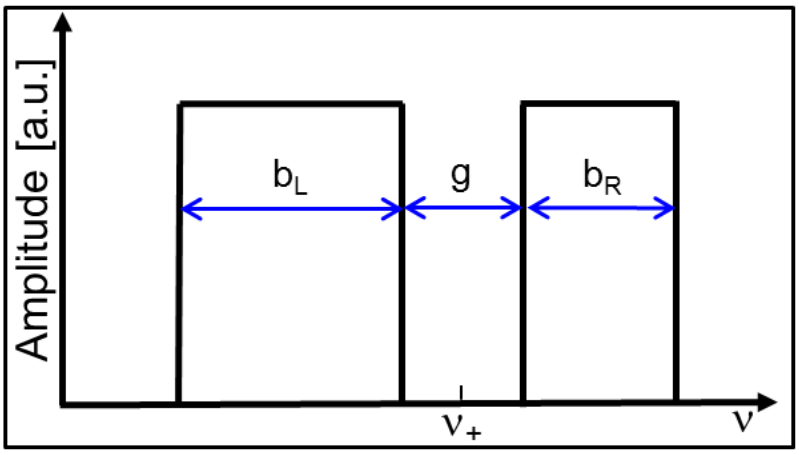

Figure 5.1: A cartoon of the desired SWIFT profile: two rectangular excitations of bandwidth b_L and b_R, separated by a gap g. The gap should be centered on the reduced cyclotron frequency ν_+ of the ion of interest.

N	10 ms	20 ms	50 ms	100 ms
16 kS	0.8	0.4	0.16	0.08
64 kS	3.2	1.6	0.64	0.32
100 kS	5	2.5	1	0.50
1 MS	50	25	10	5
4 MS	200	100	40	20
16 MS	800	400	160	80
$\Delta\nu$ [Hz]	100	50	20	10

Table 5.2: The maximum cleaning bandwidth in MHz for an AFG with memory N points for cleaning times T_{clean} = 10-100 ms. The reduced cyclotron frequency of singly charged ions at LEBIT ranges 1-10 MHz, which can be covered by either large N or amplitude modulation. The Agilent 33521 sample rate is 250 MS/s; should its full 16 MS memory be required, the shortest cleaning time is 64 ms. The last row indicates the frequency resolution in Hz.

As SWIFT requires relatively little equipment, a preliminary investigation was made with available hardware.

5.1 Signal Synthesis

The SWIFT waveform was calculated in Labview, software version 8.2. A GUI was developed that allowed the user to input the cleaning time T_{clean}, the bandwidth of the left and right bands, the size of the gap g, and the reduced cyclotron frequency ν_+. The cleaning time determines the frequency resolution, $\Delta\nu = 1/T_{clean}$, which combined with the memory of N samples limited the maximum cleaning bandwidth. Due to the Nyquist frequency, only $N/2$ points may be used. Table 5.2 tabulates the total bandwidth available for different cleaning times and memory sizes N.

At LEBIT, the reduced cyclotron frequency ranges from 7.5 MHz for A = 19 to 1.6 MHz for A = 85. To cover this bandwidth, either an AFG with a large memory ($N \geq 4$ mega-samples for T_{clean} = 100 ms) or amplitude modulation (to frequency shift the signal) must be used. If the latter is used, then a bandwidth of 30 kHz or less would be sufficient.

Amplitude modulation was carried out by multiplying the SWIFT waveform with

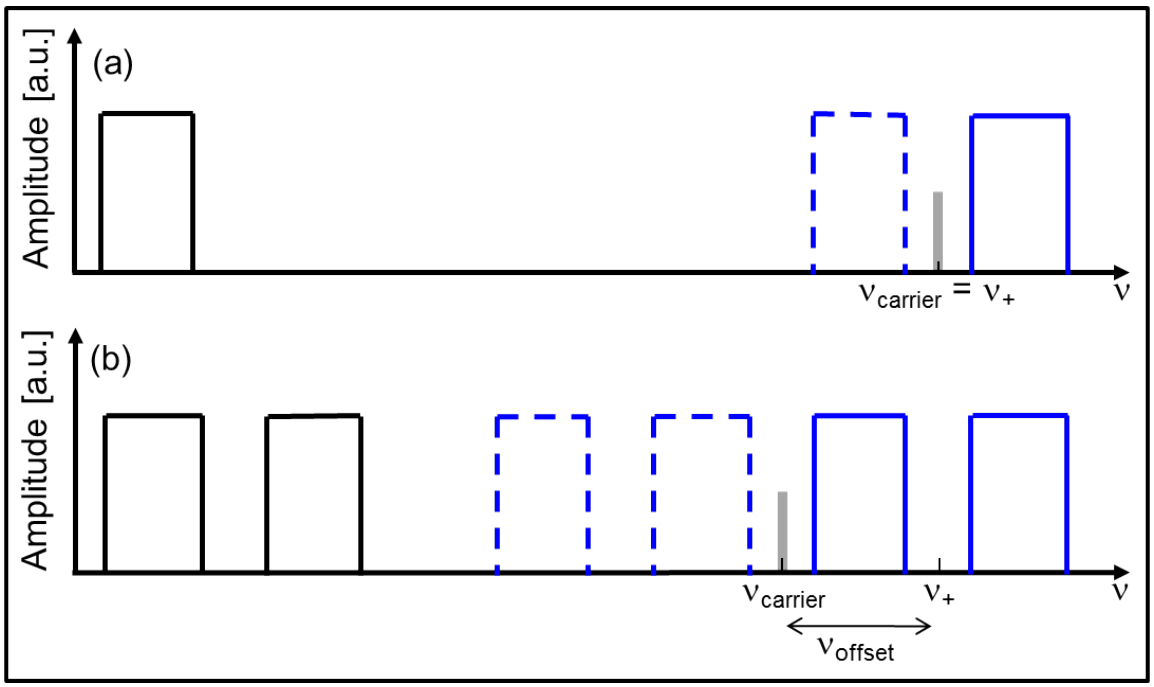

Figure 5.2: Amplitude modulation of the SWIFT signal: (a) Half of the excitation profile is defined at low frequencies (black, solid) and modulated at the carrier frequency $\nu_{carrier} = \nu_+$. The band is shifted to the frequency range of ν_+ (blue, solid) and reflected $\nu_{carrier}$ (blue, dashed). As there is typically some DC component from the AFG (shifted to $\nu_{carrier}$) and power leakage at $\nu_{carrier}$, the ion of interest may be excited by the residual signal at $\nu_{carrier}$. (b) Defining both excitation bands at low frequencies (black, solid) and then AM the signal avoids this potential noise at ν_+. The carrier frequency is chosen to position ν_+ in the center of the gap of the SWIFT excitation (blue, solid). The reflected signal (blue, dashed) is wasted.

a sine function, $\sin(2\pi\nu_{carrier}t)$, where $\nu_{carrier}$ is known as the carrier frequency. AM shifts the waveform and creates two signals at $\nu_+ \pm \nu_{carrier}$ as illustrated in Figure 5.2. Thus, only one band of the excitation needs to be generated by the SWIFT AFG and modulated at $\nu_{carrier} = \nu_+$, and its mate will also be created. However, if there is a DC component in the signal produced by the AFG, it, too, will be modulated to $\nu_{carrier}$ and could excite the ion of interest. Often, the carrier function bleeds through the AM device and results in some signal strength at $\nu_{carrier}$. To avoid these peaks, one generates a two excitation band waveform at low frequencies and then modulates that signal. An additional SWIFT waveform results but does not interfere with the desired excitation scheme.

The bandwidth (and cleaning time) should be chosen to ensure that the reduced cyclotron frequency of all contaminant ions lay within the bands b_L and b_R. The gap should be centered on the ν_+ of the ion of interest and must be wide enough not to excite it. The resolving power of SWIFT is approximately $R \approx \nu_+/(g/2)$, and the goal is to achieve a gap of 1000 Hz.

The signal must also be corrected for distortion due to digitization by the AFG. When an AFG outputs an arbitrary waveform of N points in the time T_{clean}, every output value is kept constant for a duration $\Delta t = T_{clean}/N$. This corresponds to the convolution of the signal with a rectangular function of duration Δt; that is, in the frequency domain, the excitation profile is multiplied by a sinc function. A sinc^{-1} function,

$$\mathrm{sinc}_i^{-1} = \frac{\pi i}{\sin(\pi i/N)}, \tag{5.1}$$

must be multiplied into the SWIFT amplitude profile before the inverse Fourier transformation to compensate for the effect of the digitization. This was later verified experimentally, and it was found to lower the noise floor by 5 dB.

To summarize the steps for SWIFT signal synthesis:

1. The user defines an excitation profile in frequency space of two rectangular excitation bands separated by a non-excitation gap.
2. The waveform is multiplied by a sinc^{-1} function to correct for the digitization process.
3. The waveform is phase-modulated and apodized as described in Chapter 4
4. The digital waveform is loaded into the AFG.

5.2 Preliminary Studies

For the initial investigation, two arbitrary function (waveform) generators (AFG) were used: Agilent 33250 and Agilent 33120. Both have 12 bit amplitude resolution

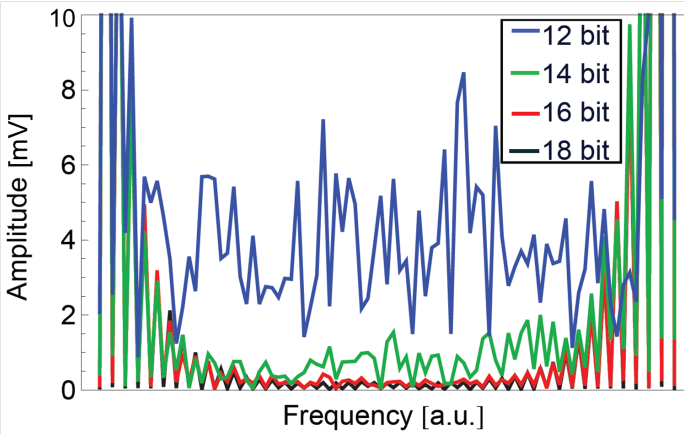

Figure 5.3: Unwanted signal power in the gap of a typical SWIFT signal due to digitization with different amplitude resolution. The amplitude of excitation is 1 V, and the desired noise suppression in the gap is a factor of 1000 or better. The Tektronix 3102 AFG, for the first implementation of SWIFT, has 14 bit resolution; the Agilent 33521, for the final and successful implementation of SWIFT, has 16 bit resolution.

for the output amplitude. The Agilent 33250 has a 64000-point memory and a 200 MS/s (mega-samples/second) sample rate while the Agilent 33120 has only 16000 points and 40 MS/s. Thus the former was used for the SWIFT signal synthesis and the latter reserved for the amplitude modulation. The carrier sine wave was generate with the Agilent 33120 sine wave generator which produces superior sine waveforms compared to the arbitrary function generator feature. Amplitude modulation only shifts the SWIFT signal to the desired frequency range (Equation B.8) and avoids the need for large AFG memory. The modulation was carried out with an Analog Devices AD835 "multiplier" chip. Various tests were performed using the LEBIT system with stable ^{85,87}Rb isotopes from the test ion source.

The initial tests indicated that SWIFT held great promise at LEBIT: ions separated by two mass units could be individually cleaned. It was also noticed that distortion from the digitization of the SWIFT signal could pose a problem, arising from the round off errors in the integer representation in the AFG memory. In Figure 5.3, SWIFT signals are calculated with different amplitude resolution. To ensure that the ion of interest was unaffected by the SWIFT excitation, the amplitude in the gap should be at least 1000 times smaller than the excitation amplitude. An amplitude

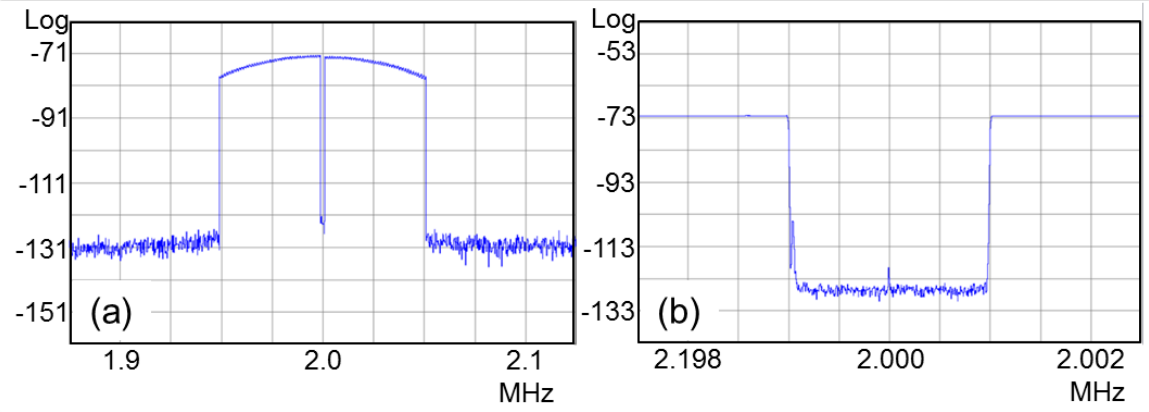

Figure 5.4: SWIFT waveform output by Tektronix 3102 AFG and captured on an Agilent EXA Signal Analyzer N9010A. (a) A SWIFT signal amplitude modulated (b = 124 kHz, g = 2 kHz, $\nu_{carrier}$ = 2.25 MHz) and captured on the Agilent spectrum analyzer. (b) The gap of the same SWIFT waveform. The peak at 2 MHz is a "cross-term" from the amplitude modulation process.

resolution of 14 bits or higher can achieve this level of noise suppression.

5.3 First implementation of SWIFT

Following the initial studies, a dedicated AFG, Tektronix 3102, was purchased. It features 14 bit amplitude resolution, N = 101 kS, a sample rate up to 250 MS/s for $N >$ 16 kS, and two output channels. It provides the minimum amplitude resolution needed and offers more flexibility than the Agilent 33250 for longer cleaning times. The SWIFT signal outputted by the Tektronix 3102 was first thoroughly investigated off-line with an Agilent EXA Signal Analyzer N9010A (frequency range 9 kHz - 3.6 GHz). These studies demonstrated that amplitude-modulated SWIFT signals fail the third criterion for success: a factor of 1000 signal suppression in the gap. An example of a SWIFT signal can be seen in Figure 5.4. The gap can be seen, and the noise floor is ≈60 dB (a factor 1000) below the amplitude of the excitation bands. The SWIFT waveforms generated by the Tektronix AFG thus met the criteria outlined above and can even produce frequency gaps smaller than 1000 Hz.

The next step was to shift the SWIFT signal into the frequency range of interest.

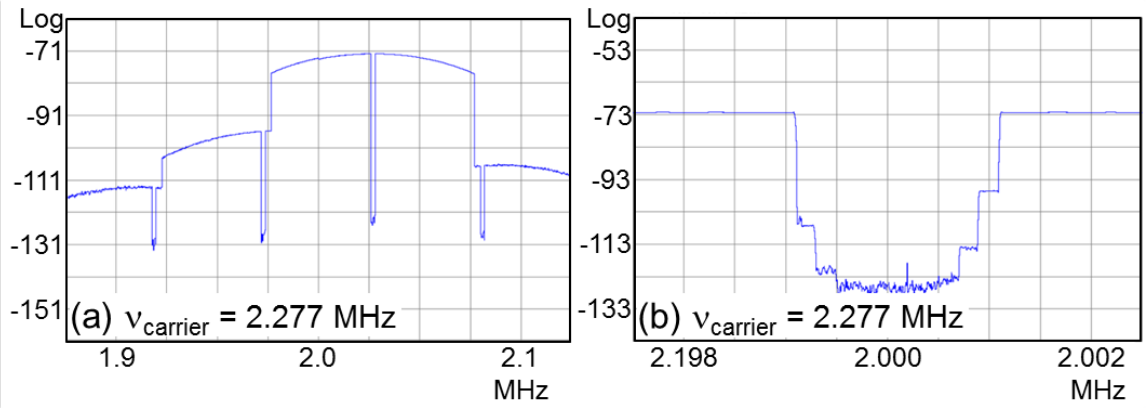

Figure 5.5: Amplitude-modulated SWIFT signals (b = 124 kHz, g = 2 kHz) captured on the Agilent spectrum analyzer: (a) $\nu_{carrier}$ = 2.277 MHz. (b) $\nu_{carrier}$ = 2.2501 MHz. The gap of the same SWIFT waveform. The Tektronix AFG produces harmonics of the fundamental SWIFT and of the modulating sine signals, all of which mix. The result is a SWIFT "family," of which at least five members are visible.

To amplitude modulate the signal, two devices were tested: the AD835 multiplier chip mentioned earlier and a Mini-Circuit ZAD-3H+ mixer. At certain $\nu_{carrier}$, a peak was seen in the gap with either AM device (see Figure 5.4b). When no source of noise could be found, the peak was traced back to the amplitude modulation process itself.

The Tektronix AFG is linear to -50 dBc in the MHz regime, i.e. it suppresses higher order harmonics of its signal by at least -50 dB. For example, there is the fundamental SWIFT signal at ν_{SWIFT}, and smaller SWIFT harmonics occur at $2\nu_{SWIFT}$, $3\nu_{SWIFT}$, etc. and similarly for the modulating sine function. Thus, the fundamental SWIFT signal is modulated by sine waveforms at $\nu_{carrier}$, $2\nu_{carrier}$, $3\nu_{carrier}$, etc. as is each of the SWIFT harmonics; thus, so-called "cross terms" are created and may interfere with the desired SWIFT signal. For certain values of $\nu_{carrier}$, the harmonic SWIFT signals constructively add with the fundamental signal, as in Figure 5.4. For other values of $\nu_{carrier}$, the cross terms fill the gap of the fundamental SWIFT waveform as shown in Figure 5.5. Furthermore, AM devices are generally nonlinear and may introduce noise themselves which may also hinder the creation of the desired SWIFT profile.

Various attempts to make the AM process more linear failed. Most RF mixers are designed for frequency ranges higher than the 1-10 MHz needed at LEBIT. To balance the mixer, the typical amplitudes had to be so high they would overload the average RF amplifier. The number of harmonic SWIFT and sine tones prevents centering an amplitude-modulated SWIFT at any given frequency. Consequently, the decision was made to abandon AM entirely in favor of simply using a very large memory AFG.

5.4 Second implementation of SWIFT

The recently issued Agilent 33521-02 offers the most memory of bench-top AFGs, 16 MS. Even for the longest cleaning time anticipated at LEBIT, T_{clean} = 100 ms, the Agilent 33521-02 can cover a frequency range up to 80 MHz. Its specifications for harmonic distortion and spurious noise are on par with other top-rated AFGs on the market, ≈-50 dBc in the MHz regime. Moreover, the amplitude resolution is 16 bits, which further improves the signal suppression in the gap of the SWIFT waveform.

5.4.1 Characterizing the SWIFT waveform

The capabilities of the Agilent 33521 AFG were explored with the same Agilent spectrum analyzer as used with the Tektronix AFG. Particular attention was paid to the two built-in filters to smooth the transition between points of an arbitrary waveform. The effects of filtering in time and frequency space can readily be seen for the test function $\sin(k/2)$ at a sample rate of 500 kS/s (see Figure 5.6). Without a filter, the transition between points is abrupt and takes ≈10 ns; in frequency space, the noise floor is higher than with the filters. The step filter response is -3 dB at 13% of the sample rate and intended to minimize ringing and overshooting on (time-domain) step functions. It provides smooth transitions between points and yields the narrowest peak in frequency space; however, the filter reduces the amplitude. The normal filter response is -3 dB at 27% of the sample rate; with this filter option, the

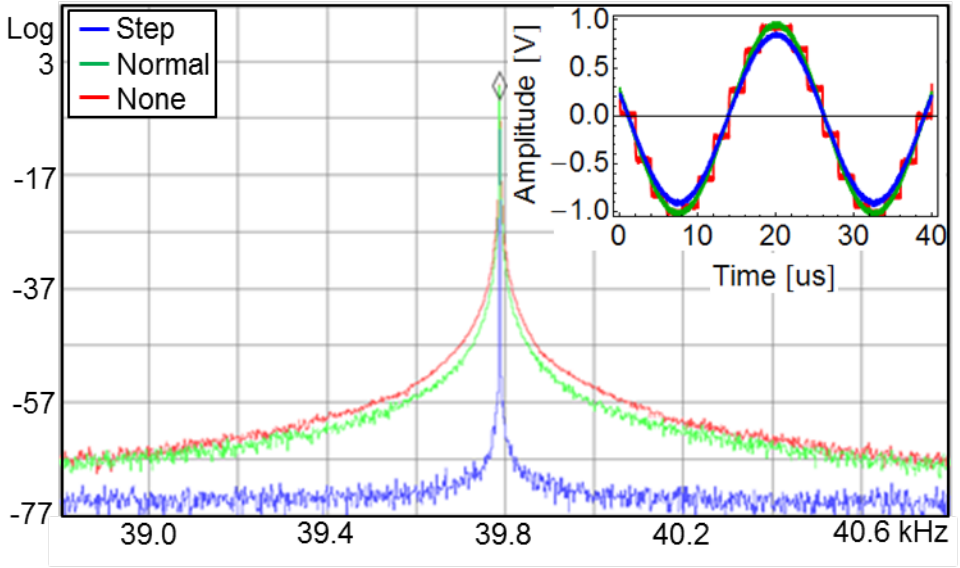

Figure 5.6: Sine waveform captured with the Agilent spectrum analyzer. The effects of the Agilent 33521 AFG built-in filters on $\sin(i/2)$ at a sample rate of 500 kS/s on the fundamental tone are compared. The spectrum analyzer time-averaged the waveforms. The inset depicts the time-domain signal.

Parameter	Symbol	Typical value
Cleaning time [ms]	T_{clean}	20
Bandwidth of left and right band [Hz]	b	1000
Gap bandwidth [Hz]	g	1000
Cleaning amplitude [V_{pp}]		180
Apodization function		Hanning
Ion species		$^{23}Na^{+}$

output is smooth in the time domain and and broad and flat in frequency space.

The effect of the two filters was also examined with a sample SWIFT signal, as shown in Figure 5.7. The typical parameters used for the SWIFT waveforms studied in this chapter are listed in Table 5.4.1. The gap was intentionally chosen to be very small ($g = 5/T_{clean}$ Hz $= 50$ Hz) to investigate if the filters offered an advantage in gap size. The step filter waveform had a very shallow slope although its measured gap was equal to the gap of the normal filter waveform. The normal and unfiltered waveforms appeared nearly identical when time-averaged, but the unfiltered waveform contained more noise. The normal filter was chosen to minimize noise and to have the most well-defined gap.

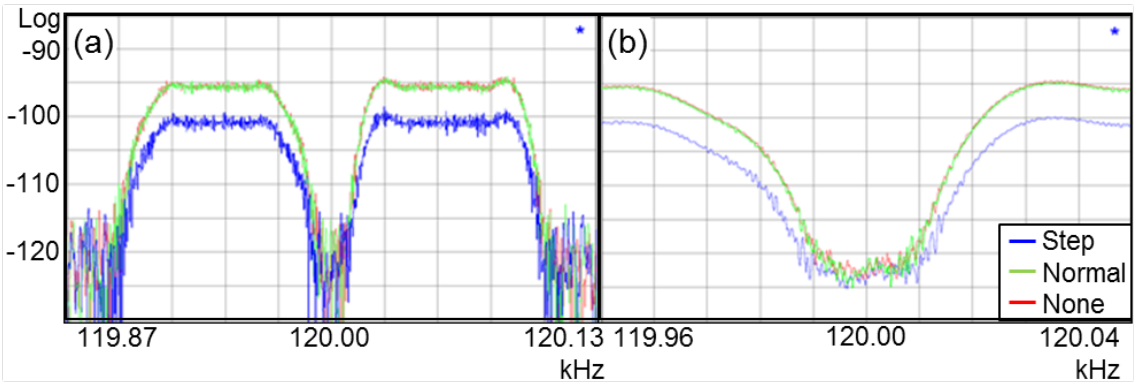

Figure 5.7: Effect of Agilent 33521 AFG built-in filters on the SWIFT signal as captured on the Agilent spectrum analyzer. The waveform was created using parameters as listed in Table 5.4.1 except T_{clean} = 100 ms and g = 50 Hz. The amplitude was 1 V_{pp} not to overload the spectrum analyzer. (a) The entire SWIFT profile. (b) The gap of the same SWIFT waveforms and time-averaged. Unfiltered signals suffer more noise than filtered signals.

By itself, the Agilent AFG output was superior to the SWIFT waveform output by the Tektronix AFG and amplitude modulated to MHz frequency range. No harmonics were found to interfere with the fundamental tone. There are no AM devices needed to raise the noise floor. But how well would SWIFT clean ions?

5.4.2 Determining the cleaning amplitude

The output of the Agilent AFG 33521 was sent to an RF amplifier (T&C Power Conversion AG1021 at 100% voltage gain), and then applied to one of the ring segment electrodes of the Penning trap. Tests of the SWIFT excitation scheme were first performed with $^{23}Na^{+}$ and $^{39}K^{+}$ produced by heating the tungsten filament of the test ion source.

To find the required cleaning amplitude for a given cleaning time and bandwidth, one excitation band was generated and centered on the reduced cyclotron frequency ν_{+} of the ^{23}Na (determined earlier by a dipole time-of-flight measurement) and the amplitude scanned. Figure 5.8 shows the relative number of ions detected after ejection from the Penning trap as a function of the cleaning amplitude. The cleaning

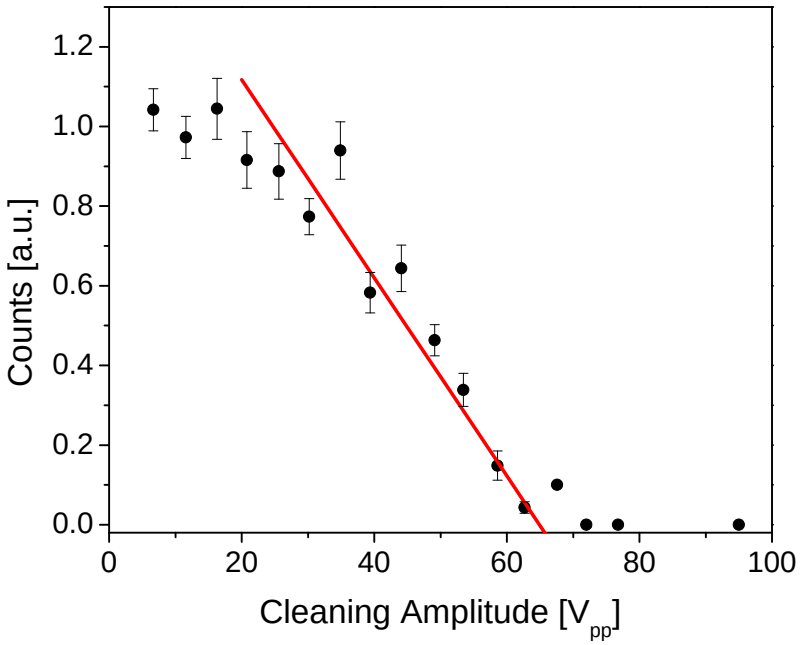

Figure 5.8: Scan of the SWIFT amplitude determined with $^{23}Na^{+}$. The red line is a linear fit to determine the amplitude needed to clean ions. The cleaning amplitude scales as $1/T_{clean}$ and increases with the bandwidth. The fluctuations are due to the ion source. (SWIFT waveform parameters are listed in Table 5.4.1 except here a single 1 kHz-wide band was used.)

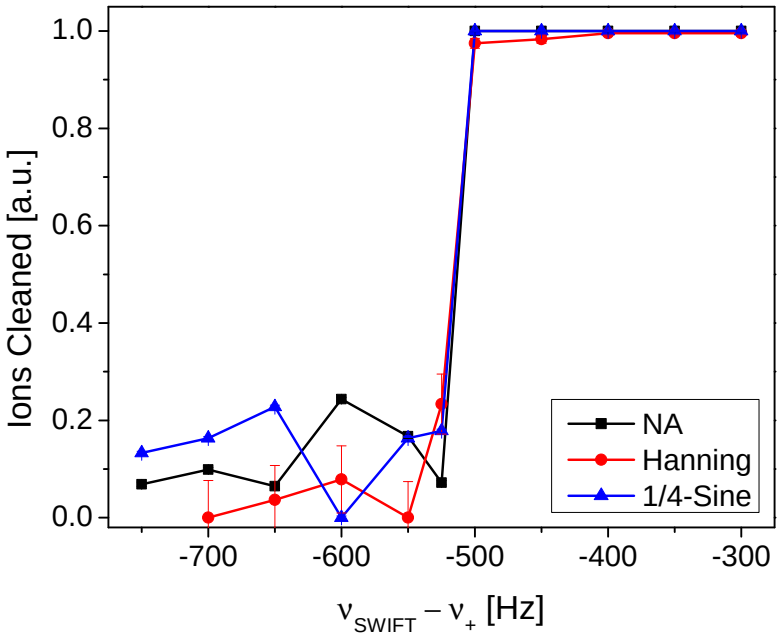

Figure 5.9: Measured side lobes of different apodization windows. The edge of a rectangular excitation band was scanned over ν_+ of $^{23}Na^+$. The Hanning wave function was chosen to minimize power leakage into the gap. (Parameters are listed in Table 5.4.1 except here only one 1 kHz band was used.)

amplitude was determined by a linear fit to the slope in the counting rate distribution. It increases with the bandwidth, b, and with the inverse of the cleaning time, $1/T_{clean}$.

5.4.3 Measurement of the SWIFT waveform with ions

The apodization window was checked by scanning the position of the edge of an excitation band over the reduced cyclotron frequency of $^{23}Na^+$. Three cases were considered: the Hanning (Equation 4.4), the "quarter-wave sine" (Equation 4.3), and no apodization functions. Figure 5.9 displays the results of the scans. All cases still contained Gibb's oscillations. The Hanning window features the smallest side lobe although it reduces the amplitude at the edge of the excitation band. Since the biggest concern is power leakage into the gap and less so the uniformity of the excitation bands, the Hanning window was chosen for apodization just as it was in Section 4.3.

Sub-figure	Ion	T_{clean} [ms]	b [Hz]	g [Hz]	Amp. [V_{pp}]	Apodization
a,b	$^{39}K^{+}$	20	500	100	95	Hanning
c,d	$^{39}K^{+}$	20	500	300	95	Hanning
e,f	$^{23}Na^{+}$	20	1000	500	180	Hanning

Table 5.3: Parameter values used to generate the excitation profiles depicted in Figure 5.10

To determine the effect of the full SWIFT excitation scheme on the ions, the excitation bands were shifted across ν_+ of $^{23}Na^{+}$ and $^{39}K^{+}$; this was accomplished by increasing the center of the gap in 25 Hz increments. Ions were injected into the Penning trap on axis, and the number detected at BOB6 was recorded as a function of the center or SWIFT frequency. Figure 5.10 compares the expected response (as calculated by a forward Fourier transform) to the counting rate distribution. Table 5.3 summarizes the parameter values used to generate the SWIFT excitations. The distribution of the number of ions cleaned from the Penning trap as a function of the SWIFT frequency closely resembles the excitation profile. The distributions of cleaned ions are flatter than the calculated waveforms because the amplitude used for the SWIFT excitation exceeded that needed to clean ions (indicated by the red dashed line) and to a lesser extent from fluctuations in the ion source. Side lobes can be seen at the edges of the excitation band. With the cleaning time held constant, $T_{clean} = 20$ ms ($\Delta\nu = 50$ Hz), the gap size was varied for the three excitation schemes shown in Figure 5.10. The gap is clearly visible. In examining the, one notices that power leakage reduces the gap by about 50 to 100 Hz on either side. Figure 5.11 shows an expanded view of the the gap shown in Figure 5.10d. Small fluctuations in counts within the gap indicate the variation in the signal power. The gap set to 500 Hz measures ≈375 Hz; the gap set to 300 Hz measures ≈200 Hz; and, the gap set to 100 Hz is filled in with its amplitude above the noise floor. From Figures 5.10 and 5.11, one can quickly ascertain that when $T_{clean} = 20$ ms the smallest gap that can be set is 300 Hz and hence obtained is ≈200 Hz.

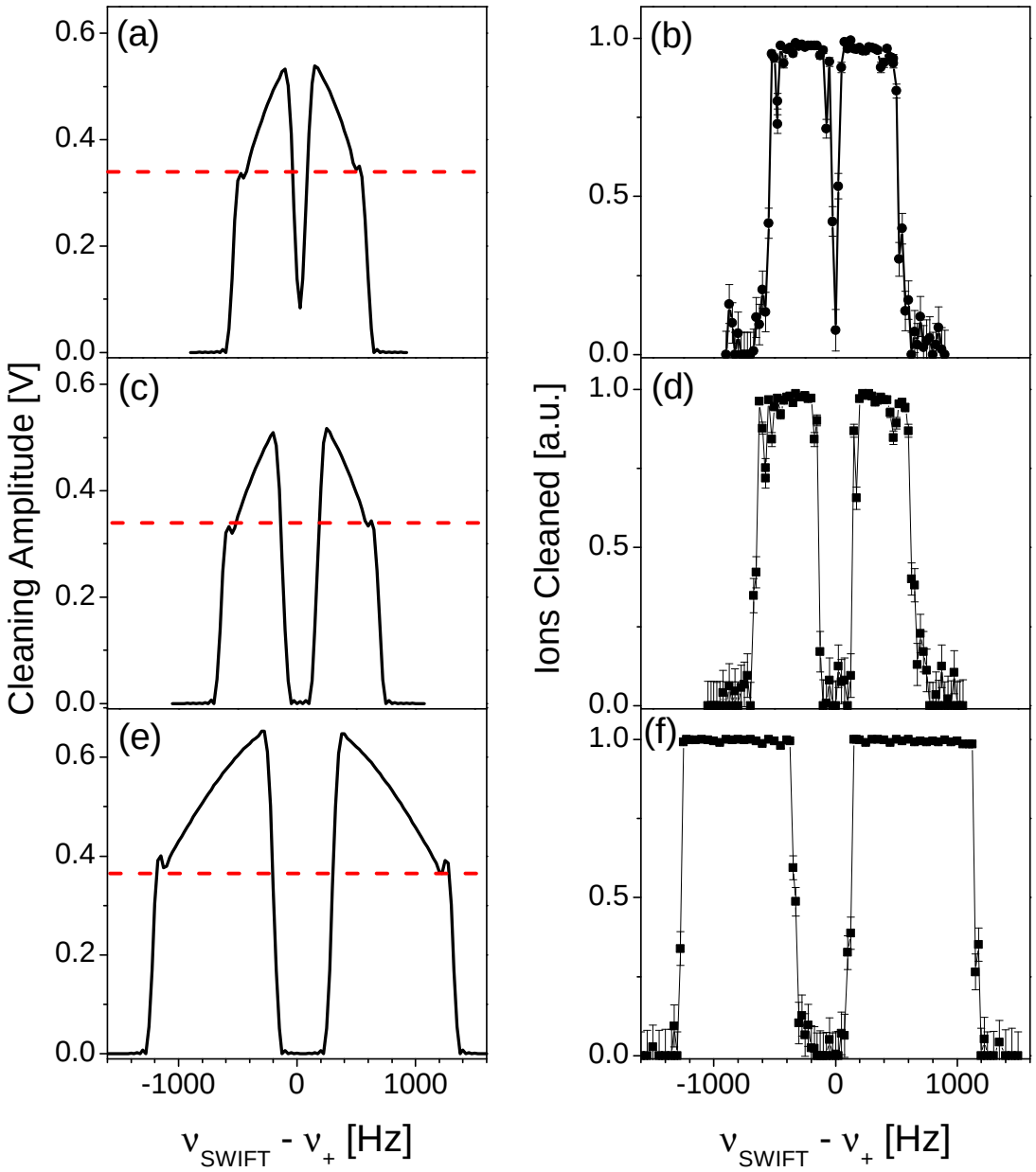

Figure 5.10: Comparison of expected SWIFT excitation profiles and observed ion profiles. The red dashed line indicates the amplitude required to remove ions. *Left:* The forward Fourier transform of the SWIFT signal. *Right:* Ions cleaned defined as (1 - normalized counts detected at BOB6) as the SWIFT signal was shifted over ν_+ in frequency space. The gap size was set as follows (a,b) g = 100 Hz, (c,d) g = 300 Hz, and (e,f) g = 500 Hz. (b,d) were experimentally determined with $^{39}K^+$ and (f) was measured using $^{23}Na^+$. (The parameter values to generate the SWIFT waveforms can be found in Table 5.3.)

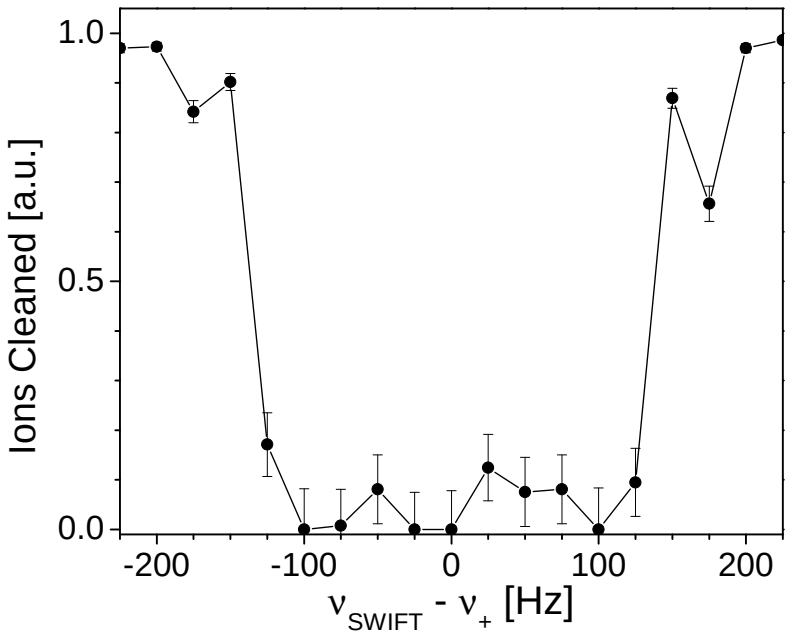

Figure 5.11: A closer look at the gap of the SWIFT excitation profile experimentally determined with $^{39}K^{+}$ shown in Fig 5.10c. Ions cleaned is the difference of one and the normalized, detected count rate. The gap was set to 300 Hz and measures ≈200 Hz. At T_{clean} = 20 ms, gaps are 100-200 Hz smaller than their set value. Generalized to any cleaning time, the gap is $2/T_{clean}$ - $4/T_{clean}$ smaller than its set value. (All other parameter values can be found in Table 5.4.1.)

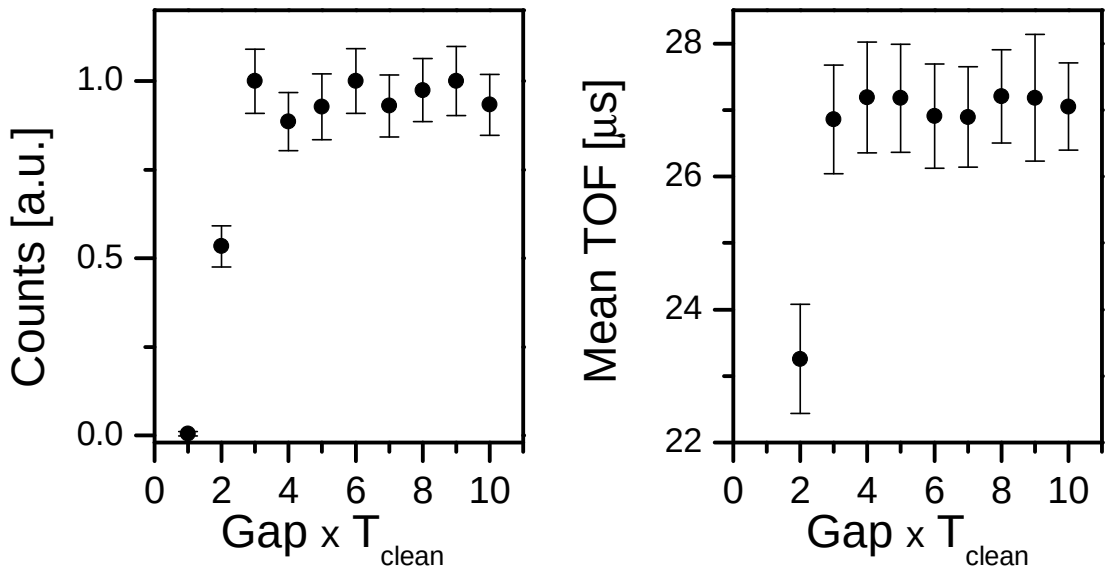

Figure 5.12: (a) Detected $^{23}Na^{+}$ ions as the gap size was varied from 0 to 500 Hz. (b) Mean TOF of $^{23}Na^{+}$ ions as a function of gap width. Although these measurements were done with T_{clean} = 20 ms, the results are identical with other cleaning times. (The parameter values used to generate the SWIFT waveform can be found in Table 5.4.1.)

5.4.4 Isobaric separation

Two quantities were measured to determine the narrowest gap achievable: the mean time of flight of the ions from the trap to the ion detector and the number of detected ions. Ions were injected on axis; the SWIFT excitation was applied, and then a quadrupole excitation followed. If the gap is too small, the ion will be excited by the SWIFT signal. If the amplitude is high enough, the ion will be cleaned. If the amplitude is small, then the ion is only driven off axis, and then during the quadrupole excitation at ν_c, its magnetron motion will be converted to cyclotron motion as described in Section 2.4.2 resulting in a shorter time of flight. Figure 5.12 shows the distribution of counts and mean time of flight as the gap was varied with T_{clean} = 20 ms. The scan was repeated for T_{clean} = 10 ms and 50 ms with identical results. Conservatively, the gap must be at least $6/T_{clean}$ wide, which corresponds to 120 Hz, 300 Hz, and 600 Hz for T_{clean} = 50 ms, 20 ms, and 10 ms respectively, to avoid disturbing the ion of interest. The findings shown in Figure 5.12 match those found

in the previous section and illustrated in Figure 5.11.

The measurements just described demonstrate the cleaning capabilities of the SWIFT technique; however, as easily seen in Figure 5.11, residual power leaks into the gap in spite of the apodization and the 16 bit amplitude resolution of the Agilent AFG. There *will* be some dipolar excitation of the ion of interest; so one is left with the question, how much will the residual dipolar excitation effect the accuracy of mass measurements?

5.4.5 Mass measurement with SWIFT

A mass measurement was performed with $^{39}K^+$ following the method described in Section 2.4.2. "Measurements" with $^{39}K^+$ performed with SWIFT cleaning were interleaved with calibrations with $^{39}K^+$ performed without cleaning. Ions were injected into the Penning trap with a non-zero magnetron radius whereas all of the measurements described above were performed with the ions injected on axis. The parameters used to generate the SWIFT waveform can be found in Table 5.4.1. The measured frequency ratios are shown in Figure 5.13. As expected, the mean ratio was found to be 1.000 000 002 7(48), or a relative deviation from unity by $2.7(48) \times 10^{-9}$; the uncertainty corresponds to 176 eV. The Birge ratio [110] is 1.02(13), which indicates extremely good agreement. The use of SWIFT does not affect the accuracy of the high precision mass measurement.

5.4.6 Measurements with CO and N_2

The ultimate test of SWIFT was to trap simultaneously two isobaric species, to clean one, and to obtain a resonance of the other. For this purpose, a mixture of carbon monoxide (CO) and nitrogen (N_2) was ionized in the test ion source operated in plasma-mode and delivered to the Penning trap, where the SWIFT cleaning was applied. The ratio of N_2^+ to CO^+ in the Penning trap was roughly 1 to 2. The CO-N_2

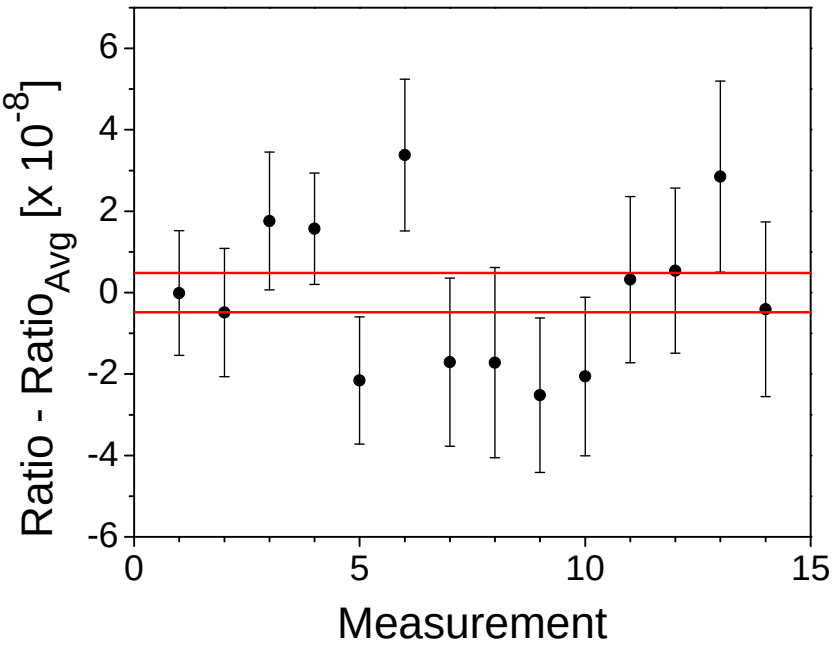

Figure 5.13: Deviations from the mean value of the mass measurement of $^{39}K^{+}$ with SWIFT-based cleaning. Calibrations were performed without cleaning. Measurements were performed with SWIFT cleaning. (SWIFT waveform parameters are listed in Table 5.4.1.) The mean ratio is 1.000 000 002 7(48); and, the Birge ratio [110] is 1.02(13).

pair, whose reduced cyclotron frequencies are separated by only 2061 Hz, simulates a typical rare isotope measurement at LEBIT; isobaric contaminants are usually a few kHz away from the radioactive ion. First, a resonance was taken with both species in the trap; with an excitation time of 7 ms and a 2700 Hz range; a resonance for each species was observed, see Figure 5.14a. Next, a SWIFT signal was generated with a 1 kHz gap and 5 kHz bands; see Table 5.4.1 for the other parameters. First the gap was centered on the reduced cyclotron frequency ν_+ of N_2^+; that is, the SWIFT excitation cleaned CO^+ from the Penning trap. As evidenced in Figure 5.14b, only the resonance for N_2^+ ions can be seen. Similarly, when the gap was centered on $\nu_+(CO^+)$ and N_2^+ was cleaned, only a resonance from CO^+ ions developed (Figure 5.14c) of CO^+. The measurements were performed over 3.5 hours, during which time the decay of the magnetic field caused a shift of 7 Hz in the measured ν_c. The simultaneous presence of contaminant ions reduced the signal strength; in Figures 5.14, the resonances in (b) and (c) clearly look better than those in (a). The resonance dip is deeper, and the sidebands are more pronounced.

5.5 Final Remarks

The measurements described in this chapter demonstrate the efficacy of SWIFT cleaning. Its successful implementation at LEBIT relied on high amplitude resolution to lower the noise floor, a large AFG memory to avoid amplitude modulation, and sufficient amplification to drive the ions. Not only has the SWIFT cleaning scheme met the criteria outlined above, but also the minimum gap size is a mere $6/T_{clean}$ (600 Hz at $T_{clean} = 10$ ms, the shortest time envisioned at LEBIT). The resolving power $R \approx \nu_+/(g/2) = \nu_+ \cdot T_{clean}/3$. For the case of $^{23}Na^+$ explored here, the resolving power ranges from $R = 4.2 \times 10^4$ for the typical LEBIT cleaning time $T_{clean} = 20$ ms to $R = 2.1 \times 10^5$ for $T_{clean} = 100$ ms. The standard or benchmark of mass spectrometry is the separation of the CO-N_2 mass doublet, which was demonstrated in Figure 5.14.

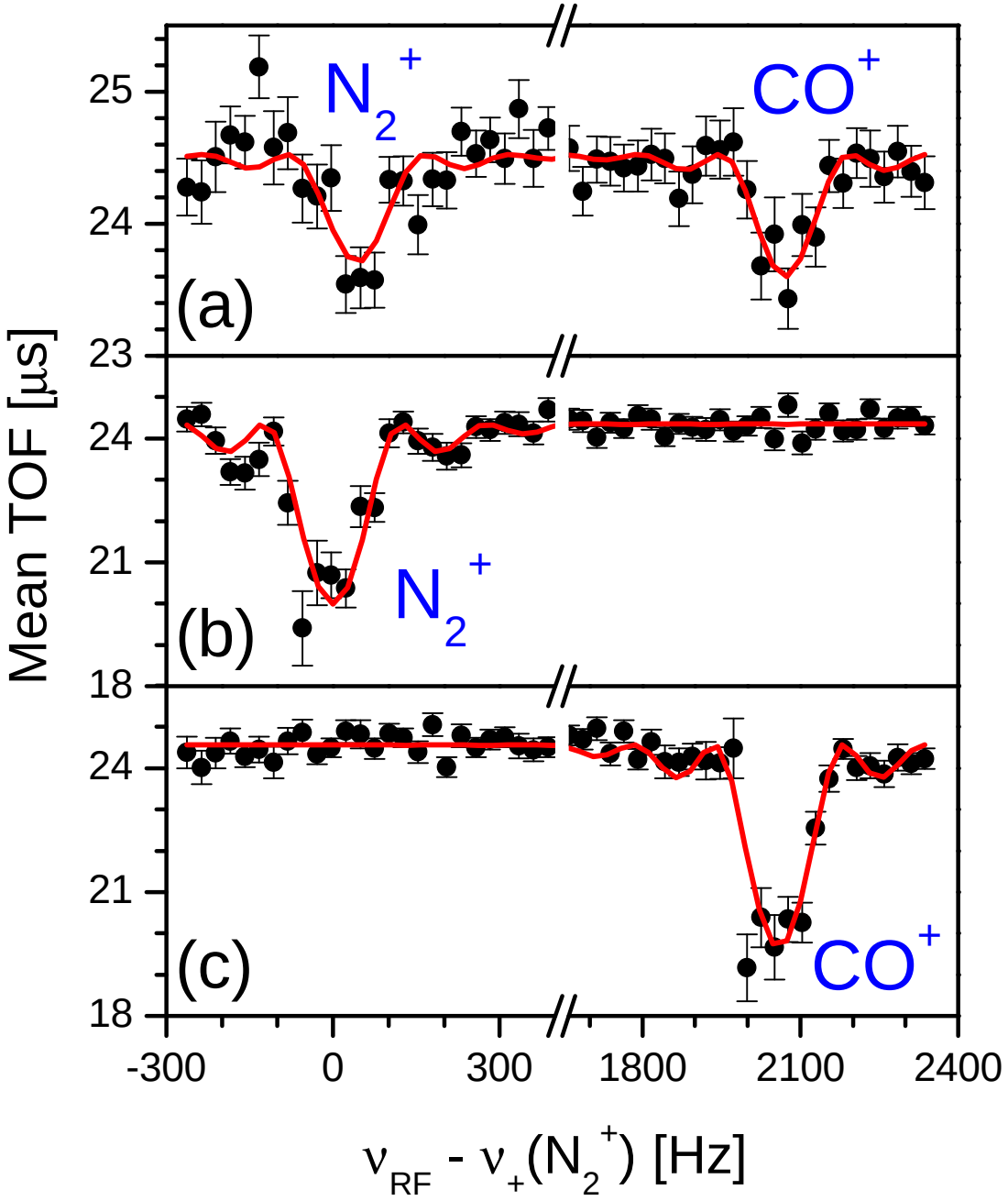

Figure 5.14: Quadrupole resonances (T_{RF} = 7 ms) with CO^+ and N_2^+ simultaneously loaded in the Penning trap. (a) SWIFT off. A small resonance is visible for each species. (b) SWIFT cleaning CO^+. Only the N_2^+ resonance is observed. (c) SWIFT cleaning N_2^+. Only the CO^+ resonance is seen. The red curves are theoretical line shapes [49] to data. The resonances were measured over 3.5 hours, during which time the decay in the magnetic field caused a shift of 7 Hz in the measured ν_c of CO^+. Note that the scale of the y-axis in (a) differs from that in (b) and (c). (SWIFT waveform parameters are as listed in Table 5.3 with b = 5 kHz here.)

Unfortunately, SWIFT could not be tested with rare isotope beams within the time frame of this work. The upgrades to the gas stopping station, which began two years ago, are still underway. Nonetheless, one can be confident of its success during future experimental work.

In comparison to other methods of isobaric purification, SWIFT has many advantages. The traditional dipole cleaning used at LEBIT requires the exact identification of each contaminant species; SWIFT cleaning eliminates this time-consuming process and allows more beam time to be devoted to the measurement of rare isotopes. Mass-selective buffer gas cooling developed at ISOLTRAP [48–50] necessitates much more hardware, occupies a significant amount of space, and most importantly is slow. At JYFLTRAP [111], for example, the best resolution $R = 1.5 \times 10^5$ was achieved with a total cleaning time of 100 ms; to reduce the total cleaning time to 54 ms dropped the resolution to $R = 2.0 \times 10^4$. SWIFT cleaning is fast ($T_{clean} = 20$ ms) and efficient (no contaminant identification), and it provides excellent isobaric purification.

Chapter 6

Summary and Outlook

In this thesis, the high precision mass measurement of ^{32}Si and its contribution to the test of the isobaric multiplet mass equation (IMME) are described. The 3 keV reduction in binding energy amplified the breakdown of the quadratic form of IMME in the A = 32, T = 2 quintet. Recent mass measurements of ^{32}Cl [97, 98] have confirmed the findings published first in [112] and updated in this work. The wealth of recent data on the A = 32, T = 2 quintet requires a large cubic coefficient, of order 1 keV, for a good fit. The newly achieved precision supports theoretical predictions for IMME from models dating from the 1970's [79, 80] to the first detailed calculations in the *sd*-shell [101] of today. The possibility of an erroneous mass has not been eliminated, and only three of the five ground state energies, ^{32}Si, ^{32}S (this work and [34]), ^{32}Ar [29] have been measured with directly. Given that this quintet is the most stringent test of IMME, it behooves the Penning trap mass spectrometry community to measure the ground state masses of ^{32}P and ^{32}Cl as well.

The history of the A = 32, T = 2 quintet offers another lesson, namely the importance of direct mass measurements. The measurements of ^{32}Si presented here shifted the mass value by 4σ. The LEBIT mass values for ^{32}S and ^{31}P agree with other Penning trap mass measurements [34, 88] and confirm a more than 1σ shift from indirect mass measurements [76]. The latter mass value in turn shifted the mass determination

of radioactive ^{32}P, a member of the A = 32, T = 2 quintet.

LEBIT would be an excellent facility to measure ^{32}P and ^{32}Cl, which can be more difficult to produce at ISOL facilities. The LEBIT mass measurement campaign will resume shortly following upgrades to the gas stopping station and the installation of the NSCL 3 MeV/u re-accelerator, ReA3. The upgrades include linear gas stopping with improved efficiency and cleaner beams and, eventually, a cyclotron stopper [113] with shorter extraction times and improved stopping of light ions.

In parallel to its mass campaign and then the NSCL developments, the LEBIT collaboration has pursued upgrades of its own, including improved beam purification. SWIFT cleaning reduces the systematic uncertainty in mass measurements. Compared to dipole cleaning, it eliminates the need for individual identification of contaminant ions. Compared to mass=selective buffer gas cooling, SWIFT provides high resolution cleaning at short cleaning times, occupies less space, and requires less hardware. The criteria for successful implementation were met. Noise suppression in the gap is a factor of 1000 compared to the excitation band amplitude. Gaps narrower than 1 kHz were demonstrated. When CO^+ and N_2^+ ions were simultaneously trapped, SWIFT removed one species without disturbing the other. A resolving power in better than 10^7 was achieved. SWIFT cleaning is certain to become a heavily used tool in future LEBIT mass measurements.

APPENDICES

Appendix A

Experimental Data of the A = 32, T = 2 Quintet

This appendix supplements the data and text in Chapter 3. The most recent and most precise measurements available for each nuclei are reviewed and compared to the accepted literature values in the Atomic Mass Evaluation 2003 (AME'03) [76] and the preview of the Atomic Mass Evaluation 2013, released earlier this year (referred to as AME'11) [91]. (As AME'11 is in a preliminary form, the evaluation and references are undocumented.) This appendix is not a comprehensive review of all experimental data relevant to the quintet. The ground states of the interior members ^{32}P, ^{32}S, and ^{32}Cl have isospin T = 1, 0, 1 respectively; since the first T = 2 state is of interest, measurements of its excitation energy are also described.

A.1 Mass Value of the Ground State of ^{32}Si

The AVOGADRO group measured the masses of $^{29-32}$Si via thermal neutron capture on ^{28}Si [89]. This measurement is the basis for the AME'03 compiled value -24080.81(05) keV [76] although the authors themselves republished the data in 2001, with ME = -24080.86(77) [90] without explanation for the larger uncertainty. The

A	AVOGADRO	IAEA	AME'11	Δ
29	8473.551(05)	8473.537(23)	8473.6(0)	-0.048(5)
30	10609.18(1)	10609.23(03)	10609.20(2)	-0.02(2)
31	6587.40(3)	6587.39(03)	6587.39(4)	0.01(5)
32	9203.22(6)		9199.97(30)	3.25(31)

Table A.1: Comparison of neutron separation energies S_n (in keV) for several Si isotopes from the AVOGADRO project [89, 90], the IAEA database [100], and the preview of the next Atomic Mass Evaluation (AME'11) [91]. Since the IAEA database and AME'11 agree, only the difference of the AVOGADRO project and the AME'11 (Δ = $\mathrm{ME}_{AVOGADRO}$ - $\mathrm{ME}_{AME'11}$) is provided.

values of γ-ray energies were unchanged although their uncertainties were an order of magnitude higher than originally documented. Propagation of the new error does not result in $\sigma = 0.77$ keV.

Since then, the mass of ^{28}Si was measured with a precision of 0.6 eV at the Florida State University (FSU) Penning trap mass spectrometer [88]. Although a small discrepancy was found with AME'03 (2.3 $\pm$ 1.9 eV), it is negligible for this discussion. The newly adopted mass value in AME'11 is used to recalculate the neutron separation energies S_n from the AVOGADRO-measured γ-ray energies. Table A.1 compares the neutron separation energies from AME'11, IAEA, and the recalculated AVOGADRO values. AME'03 (and subsequently AME'11) also compiled measurements performed at McMaster University [114,115] and Los Alamos National Laboratory [116], which deliver precise ($\sigma \leq 140$ eV) and mutually consistent measurements. The IAEA [100] tracks thermal neutron capture data, including neutron separation energies, from the Lone database, the Reedy and Frankle database, ENSDF, and the Budapest reactor; unfortunately, it does not include the S_n of ^{32}Si. Nonetheless, its S_n values for ^{29}Si, ^{30}Si, and ^{31}Si are in excellent agreement with AME'03 and AME'11. The AVOGADRO S_n data agrees with the IAEA compilation for ^{29}Si and ^{31}Si but not for ^{30}Si, 51(31) eV. With respect to the compilation in AME'11, agreement is found for ^{30}Si and ^{30}Si, while for ^{29}Si deviation is significant, 48(5) eV, and for ^{32}Si 3.25(31) keV. The latter is essentially the discrepancy in the mass of ^{32}Si

Ref.	Method	ME [keV]
[95][a]	^{30}Si(t,p)	-24078.(1.3)
[90]	^{28}Si(n,γ)	-24080.86(77)
this work	PTMS	-24077.68(30)
AME'11 [91]		-24077.687(297)
[88, 90][b]		-24080.87(77)

[a] Published only in a conference abstract
[b] ME value of ^{28}Si [88] and the S_n values of $^{29-32}$Si [91]

Table A.2: Recent ground state mass measurements and values of ^{32}Si: the reference, the technique, and the mass excess value are given in chronological order.

given that the AME'11 adopted value is the LEBIT mass value. The mass values are compared in Table A.2. The LEBIT mass value agrees with an undocumented (t,p) measurement [95].

Ground State Mass Excess		
Ref.	Method	ME [keV]
AME'03 [76]		-24305.218(187)
AME'11 [91]		-24304.874(040)
[91, 100][a]		-24304.82(23)
First T = 2 Excitation Energy		
Ref.	Method	E_x [keV]
[117]	^{30}Si(^{3}He,pγ)	5072.9(1.5)
[118]	^{30}Si(^{3}He,pγ)	5073.4(1.5)
[119]	^{31}P(p,γ)	5072.42(06)
[120]	^{31}P(p,γ)	5072.535(123)
NNDC [87]		5072.44(06)

[a] ME value of ^{31}P [91] and proton separation energy S_p of ^{32}P [100]

Table A.3: Recent ground state and excited state energy values of ^{32}P: the reference, the technique, and the mass excess value are given in chronological order.

A.2 Mass Value of Isobaric Analog State of ^{32}P

The ground state mass of ^{32}P has been measured at several institutions through β-decays of ^{32}P [121] and of ^{32}Si [122] and via ^{31}P(n,γ) [100,119,120]. The latter requires accurate knowledge of the mass of ^{31}P. The Penning trap mass measurement of ^{31}P in this thesis and at FSU [88] agree extremely well and achieve a higher precision than the compiled value in AME'03 [76] and shift the mass value by about 300 eV. The AME'03 value of ^{31}P was based on several ^{31}P(p,γ) reactions, but AME'11 appears to adopt the weighted average of the Penning trap mass measurements for ^{31}P. The average ^{31}P value can be combined with the ^{32}P neutron separation energy for a high precision mass excess value for ^{32}P.

The excitation energy of ^{32}P was first explored via charge exchange [117,118] and later by neutron capture [119, 120]. Measurements are mutually consistent. In this thesis, the accepted literature value [86] of E_x is adopted.

Ground State Mass Excess		
Ref.	Method	ME [keV]
AME'03 [76]		-26015.70(14)
[34]	PTMS	-26015.5344(15)
this work	PTMS	-26015.34(32)
AME'11 [91]		-26015.53374(133)
First T = 2 Excitation Energy		
Ref.	Method	E_x [keV]
[96]	^{31}P(p,p), ^{31}P(p,α)	12049(2)
[95][a]	^{31}P(p,γ)	12045..0(4)
[33]	^{31}P(p,γ)	12047.96(28)

[a] Published only in a conference abstract

Table A.4: Recent ground state and excited state energy values of ^{32}S: the reference, the technique, and the mass excess value are given in chronological order.

A.3 Mass Value of the Isobaric Analog State of ^{32}S

A stable isotope, ^{32}S is highly accessible. Despite this, the uncertainty of the AME'03 value for the ground state energy is 140 eV. The precision in the AME'11 value is improved by the Penning trap mass measurements of this work and in [34]. The latter finds a small but acceptable deviation of 166(140) eV from the AME'03 value. The LEBIT mass value exhibits a similar, acceptable deviation from AME of 360(349) eV. AME'11 appears to incorporate the two Penning trap measurements, for an uncertainty of ≈1 eV.

Surprisingly, few measurements have been made of the first T = 2 excitation energy [33, 95, 96]. Unfortunately, the authors of [95] did not document their work further than a conference abstract, and their measured E_x disagrees with the more recent measurements. The (p,p) and (p,α) measurement [96] suffers from a large uncertainty, 2 keV. The (p,γ) measurement [33] offers the smallest uncertainty, 0.28 keV. In this work, the ground state mass excess is taken from AME'11 and the excited state energy is the weighted average of [33, 96].

A.4 Mass Value of the Isobaric Analog State of ^{32}Cl

The AME'03 mass value for the ground state of ^{32}Cl was based on charge exchange measurements made more than 25 years earlier [123–125] and suffered a large ≈7 keV uncertainty. Within the past year, two high precision measurements have been made [97, 98]. As there is a small difference in the values of the weighted average of [97, 98] and the AME'11 value, both are used to fit IMME although the difference was found to be insignificant. The NNDC [87] gives the first T = 2 excited state energy E_x = 5024(8) keV but has not been updated to include the most recent measurement [99], which found E_x = 5046.3(4) keV. The difference of 22 keV most likely arises from

Ground State Mass Excess		
Ref.	Method	ME [keV]
AME'03 [76]		-13329.771(6.593)
[97]	^{32}S(^{3}He,t)	-13333.8(1.2)
[98, 99][a]		-13334.88(65)
AME'11 [91]		-13335.115(939)
First T = 2 Excitation Energy		
Ref.	Method	E_x [keV]
[126]	^{32}Ar(β)	5057(12)[a]
[125]	^{32}S(^{3}He,t)	5018(10)
[127]	^{32}Ar(β)	5052(9)[a]
NNDC [87]		5045(8)[a]
[99]	^{32}Ar(β)	5046.3(4)

[a] 21 keV has been added for the newer mass measurement of ^{32}Ar [29]

Table A.5: Recent ground state and excited state energy values of ^{32}Cl: the reference, the technique, and the mass excess value are given in chronological order.

the 2003 direct mass measurement of ^{32}Ar, whose value changed by 21 keV. The measurement from [99] is used exclusively in this analysis.

A.5 Mass Value of the Ground State of ^{32}Ar

The only direct mass measurement of ^{32}Ar and the sole basis for the AME'03 [76] and AME'11 [91] values is a Penning trap mass measurement from the ISOLTRAP collaboration [29], ME = -2200.2(1.8) keV, a 21(50) keV shift from the previously accepted value. AME'11 updates the reference mass used to calibrate the magnetic field, yielding ME = -2200.369(1.770) keV, the value adopted in this analysis.

Appendix B

Fourier Transforms and Their Properties

Fourier analysis developed from the study of Fourier series, introduced by Joseph Fourier. The French physicist and mathematician was solving the problem of heat transfer through a metal plate; he proposed modeling heat sources as a linear sum of trigonometric functions. This superposition, known as the Fourier series, allows any complicated periodic function to be decomposed into sine and cosine functions.

This decomposition process led to the Fourier transform. The value of the transform is the dual perspective of a function in both time and frequency space. The forward Fourier transform (FT) permits the analysis of the amplitude and phase of each frequency component, while the inverse Fourier transform (IFT) allows the synthesis of a time-domain signal from any arbitrary frequency signal.

Below is a brief introduction to Fourier transforms and the properties relevant to the stored waveform inverse Fourier transform (SWIFT) technique in Chapters 4 and 5. More comprehensive discussion of Fourier transforms can be found in, for example, [109, 128].

B.1 Definition

There are several common conventions to define the Fourier transform. In this work, the unitary transformation is taken here:

$$F(\nu) = \int_{-\infty}^{+\infty} f(t)\, e^{-2\pi i \nu t}\, \mathrm{d}\nu \quad \Longleftrightarrow \quad f(t) = \int_{-\infty}^{+\infty} F(\nu)\, e^{+2\pi i \nu t}\, \mathrm{d}\nu \tag{B.1}$$

The latter is the inverse Fourier transform. Here the independent variable t represents time and the transform variable ν frequency. Clearly the time-domain signal $f(t)$ and its Fourier transform $F(\nu)$ are complex. The Fourier transform can be written as a plane wave of amplitude $|F(\nu)|$ and with phase $\phi(\nu)$: $F(\nu) = |F(\nu)|\, e^{i\phi(\nu)}$. Or, using Euler's formula, $e^{i\theta} = \cos\theta + i \sin\theta$, it can be decomposed into its real part $R(\nu)$ and imaginary part $I(\nu)$, which relate to the amplitude and phase by

$$|F(\nu)|^2 = R(\nu)^2 + I(\nu)^2 \tag{B.2a}$$

$$\tan(\phi(\nu)) = I(\nu)/R(\nu). \tag{B.2b}$$

Perhaps the most intuitive example is a sine wave in the time domain at a frequency ν_0 and its transform a delta function in frequency spaced centered a ν_0.

$$f(t) = \sin(2\pi\nu_0 t) \quad \Longleftrightarrow \quad F(\nu) = \delta(\nu - \nu_0) + \delta(\nu + \nu_0) \tag{B.3}$$

Another common pair, including in the SWIFT waveforms, is the rectangle (or "top hat") function and the sinc function.

$$f(t) = \begin{cases} 1, & \text{if } |t| \leq \frac{T}{2} \\ 0, & \text{if } |t| > \frac{T}{2} \end{cases} \quad \Longleftrightarrow \quad F(\nu) = \mathrm{sinc}_T(\nu) = \frac{\sin(\pi\nu T)}{\pi\nu}. \tag{B.4}$$

B.1.1 Basic Properties

To describe the properties of Fourier transforms relevant to SWIFT, let $F(\nu)$, $G(\nu)$, and $H(\nu)$ be the Fourier transforms of the integrable functions $f(t)$, $g(t)$, and $h(t)$ respectively.

Linearity: For any complex number a and b,

$$h(t) = a\,f(t) + b\,g(t) \quad \Longleftrightarrow \quad H(\nu) = a\,F(\nu) + b\,G(\nu) \tag{B.5}$$

Scaling: For any non-zero, real number a,

$$g(t) = f(at) \quad \Longleftrightarrow \quad G(\nu) = \frac{1}{|a|} F\left(\frac{\nu}{a}\right) \tag{B.6}$$

Translation: A linear translation in time t_0 shifts the phase in the frequency domain.

$$g(t) = f(t - t_0) \quad \Longleftrightarrow \quad G(\nu) = e^{-2\pi i t_0 \nu}\, F(\nu) \tag{B.7}$$

Modulation: Similarly, for any real number ν_0,

$$g(t) = e^{2\pi i t \nu_0}\, f(t) \quad \Longleftrightarrow \quad G(\nu) = F(\nu - \nu_0) \tag{B.8}$$

Complex conjugation:

$$g(t) = f^*(t) \quad \Longleftrightarrow \quad G(\nu) = F^*(-\nu) \tag{B.9}$$

Convolution:

$$h(t) = \int_{-\infty}^{+\infty} f(\tau) g(t - \tau)\, \mathrm{d}\tau f(t) * g(t) \quad \Longleftrightarrow \quad H(\nu) = F(\nu) \cdot G(\nu) \tag{B.10}$$

Similarly, $h(t) = f(t) \cdot g(t) \iff H(\nu) = F(\nu) * G(\nu)$.

Parseval's theorem: If $f(t)$ and $g(t)$ are square integrable, then

$$\int_{-\infty}^{+\infty} f(t) g^*(t)\, \mathrm{d}t = \int_{-\infty}^{+\infty} F(\nu) G^*(\nu)\, \mathrm{d}\nu \tag{B.11}$$

Perhaps the most important physical consequence of Parseval's theorem is the conservation of energy. That is, the total energy stored in the time-domain spectral density $|f(t)|^2$ equals that in the frequency-domain density $|F(\nu)|^2$.

B.2 The Discrete Fourier transform

Often in experiment, N data points are collected at times separated by Δt into the data set f_n where $n = 0, 1, \ldots, \mathrm{N}$. The total measurement time T is their product $N\,\Delta t$ and results in a frequency resolution of $1/T$. Since frequency and time are reciprocal, if the duration T is decreased while N stays constant, the frequency bandwidth increases while the frequency resolution drops. The discrete Fourier transform (DFT) F_m and its inverse f_n replace their continuous counterparts:

$$F_m = \tfrac{1}{N} \sum_{n=0}^{N-1} f_n e^{2\pi i n m/N} \iff f_n = \sum_{m=0}^{N-1} F_m e^{-2\pi i m n/N} \tag{B.12}$$

The definition implies the functions in the time and frequency are periodic over the intervals $[0,\ T]$ and $\left[-\frac{N/2}{T},\ \frac{N/2}{T}\right]$ respectively. In this sense, negative frequencies "wrap around" to the interval $\left[\frac{N/2}{T},\ \mathrm{N}\right]$. Another way to look at the DFT is to consider the data set $[f_n]$ as a vector multiplied by an $n \times n$ square matrix of the exponentials to obtain another vector $[F_m]$ of length n. Properties of the continuous transform can also be applied to the discrete transform.

B.3 Fast Fourier transform

Calculation of the discrete Fourier transform requires N^2 operations. The invention of the Fast Fourier Transform (FFT) [129] reduces the number of operations to $2N \log_2 N$, a substantial savings in time. If N is divisible by 2, $[a_n]$ could be broken into two vectors, each of length $N/2$ and subjected to a Fourier transform of only half the length to give two vectors, which when multiplied by the so-called exponential "twiddle parameters" and re-combined to yield $[F_m]$. This process can be repeated until only trivial 2×2 matrices are left. Furthermore, N can be any non-prime number; the FFT relies on factorization of the Fourier transform matrix. More information on FFT algorithms can be found in [129, 130]

B.4 Sampling theorem

In digital signal processing, how frequently must a signal be measured to determine accurately its frequency spectrum? The sampling theorem supplies the answer: the Nyquist or folding frequency ν_N, which is twice the highest frequency component. The bandwidth of the spectrum is -$\frac{N/2}{T}$ to +$\frac{N/2}{T}$. The theorem is more easily understood schematically as illustrated in Figure B.1. If the signal is non-zero above the Nyquist frequency, the power will be "folded" back into the spectrum and appears at a lower frequency. A frequency at $\nu_N + \Delta\nu$ is mapped to ν_N - $\Delta\nu$. Aliasing, as it is called, is the result of beating between the frequency and the sampling rate.

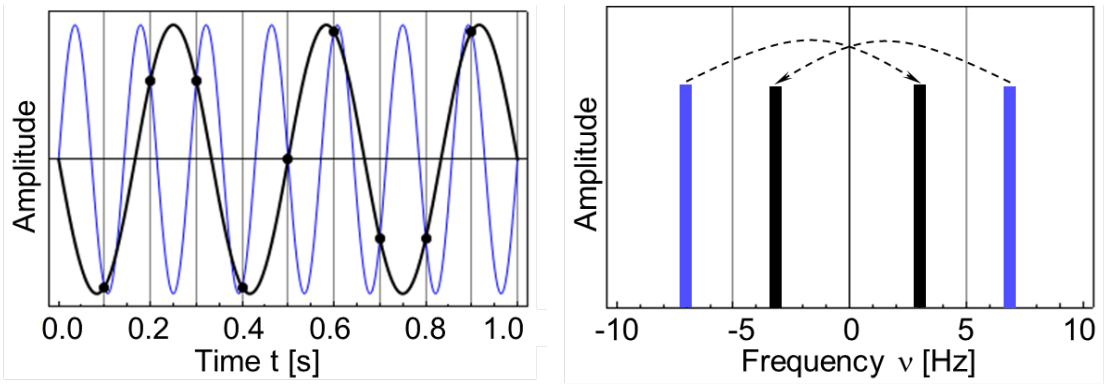

(a) In the time domain

(b) In the frequency domain

Figure B.1: Illustration of the sampling theorem. Left: A 7 Hz sine wave (blue) is sampled 10 times over 1 second (black dots). Since the Nyquist frequency $\nu_N = 5$ Hz, the measured function (black curve) is at 3 Hz. Right: In the frequency domain, the true frequency (blue) is mapped into the bandwidth [-5 Hz, 5 Hz] at 3 Hz (black).

Appendix C

Simulations of RFQ Mass Filter: Calculations of Transmission and Emittance

The RFQ ion guides were designed and constructed as part of Pete Schury's thesis work [45]; however, the emittance of the ion guides and in particular of the mass filter was not studied at the time. To my knowledge, there have been no published studies of the emittance as a function of mass filtering strength. This appendix presents the results of simulations performed in SIMION 8.0 of the emittance and transmission through the LEBIT RFQ mass filter; and, they complement experimental studies performed by and under analysis by Rafael Ferrer. The ion guides were described in Section 2.2, and their design was shown below in Figure C.1. The ion motion in an RFQ trap are well known [59, 60, 131]; hence, the equations of motion will be stated here without derivation.

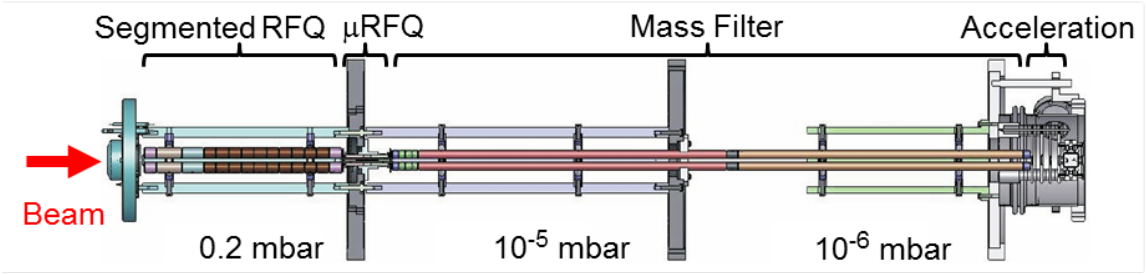

Figure C.1: Mechanical design of the RFQ ion guides. The three sections are followed by a 5 keV acceleration region and end at BOB1.

C.1 Ion Motion in an RFQ Ion Guide

In an RFQ, there are four rods, each phase-shifted 180° from its nearest neighbor. If the potential difference between the rods is $V_{DC} - U_{RF}\cos(\omega t + \phi)$, then the equations of motion are

$$\ddot{x} + \frac{e}{mr_0^2}(V_{DC} - U_{RF}\cos(\omega t))x = 0 \tag{C.1a}$$

$$\ddot{y} - \frac{e}{mr_0^2}(V_{DC} - U_{RF}\cos(\omega t))y = 0 \tag{C.1b}$$

$$\ddot{z} = 0 \tag{C.1c}$$

$$\tag{C.1d}$$

where the z-direction is taken along the beam axis. They can be rewritten using the dimensionless parameter $\xi = \omega t/2$ for the phase of the driving RF field and the Mathieu parameters a and q:

$$a_x = -a_y = \frac{4eV_{DC}}{m\omega^2 r_0^2} \tag{C.2a}$$

$$q_x = -q_y = \frac{2eU_{RF}}{m\omega^2 r_0^2} \tag{C.2b}$$

$$\tag{C.2c}$$

Then the transverse equations of motion may be written as

$$\frac{d^2u}{d\xi^2} + [a_u - 2q_u \cos 2\xi]u = 0 \tag{C.3}$$

where u represents x or y. Setting aside the trivial solution, the ion may follow either a stable oscillatory trajectory or an unstable exponentially increasing trajectory. This defines regions of stability in in the Mathieu parameter space (a, q) for the x- and y-directions, and where they overlap the ion motion is stable in the transverse plane. The first region of stable x- and y-trajectories is commonly referred to as the stability diagram and by convention is shown only for $a > 0$ since it is symmetric about a (see Figure C.2. The left edge of the stability diagram represent a heavy-mass cutoff and the right edge a light-mass cutoff. At the tip of the stability diagram, (a,q) = (0.237,0.706), only ions of a particular mass have stable trajectories. For $a \neq 0$, the RFQ ion guide becomes a bandpass mass filter. The mass filter strength at LEBIT is measured by the ratio $\alpha = V_{DC}/U_{RF}$. As ions enter the mass filter ($a \neq 0$), they pass through a region of stability as indicated in Figure C.2. If V_DC is slowly increased, the ion always stays within the stable region; a Brubaker or delayed DC-field [71] accomplishes this and was implemented at LEBIT [45].

Two sets of ions were considered, an "ideal" case and a damped version for the masses A = 28, 45, and 85. In the ideal case, the ions were assumed to have been damped in the segmented RFQ (due to buffer gas leaking from the gas cell) and to have reached thermal equilibrium in the μRFQ; i.e. their initial conditions were ideal. Following the discussion in [131], the equilibrium density distribution of the ions was a Gaussian distribution in the x- and y-directions with standard deviations σ_u and σ_v in phase space.

$$\sigma_u = \frac{1}{\omega_u}\sqrt{\frac{k_BT}{m}}, \quad \sigma_v = \sqrt{\frac{k_BT}{m}} \tag{C.4}$$

where k_B is the Boltzmann constant, T is the temperature at 20° C, and ω_u is the eigenfrequency of the macromotion. For sufficiently small Mathieu parameter q, ω_U

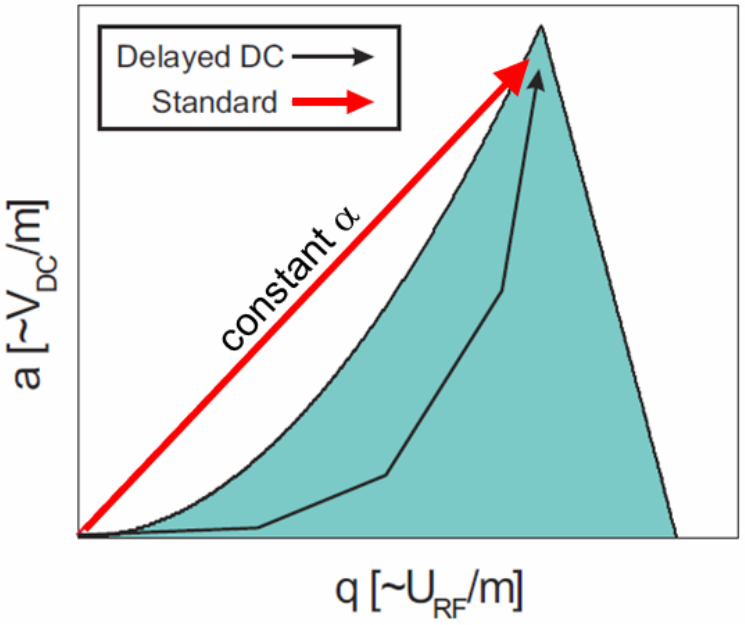

Figure C.2: Stability diagram in the Mathieu parameter space (a,q). The red line corresponds to a constant α. As the ion enters the mass filter, it passes through a region of instability. By slowly increasing the DC-quadrupole or mass filter strength α (black line), the ion always stays within the stable region.

may be approximated by $q_u\omega_{RF}/\sqrt{8}$. The RF phase was randomly sampled; the RF drive is a periodic transformation of the initial phase-space distribution into another of the same area.

$$\begin{pmatrix} u \\ v \end{pmatrix} = \begin{pmatrix} \gamma_u & 0 \\ \gamma_u \frac{\omega_{RF}}{2} \tan\theta_r & \frac{1}{\gamma_u} \end{pmatrix} \cdot \begin{pmatrix} u \\ v \end{pmatrix}_{macro} \tag{C.5}$$

where the stretch and rotation parameters γ and θ_r are complicated functions of the RF phase and the operating parameters. The following parameterizations of γ and θ_r [132], valid for $|q| \lesssim 0.7$, were used:

$$\gamma_u = 1 + p_0 e^{p_1|q|} - p_2\, q \cos(2\xi)\ (1 + p_3\,|q|^{p_4}) \tag{C.6a}$$

$$\tan\theta_r = q\,(1 + r_0\,|q|^{r_1}) \cdot \sin(\,2\xi + r_2\, q \sin(2\xi)\,). \tag{C.6b}$$

The parameters p_i are listed in Table C.1. For any given RF phase, the ion trajectory

i	p_i	r_i
0	0.00371	1.02035
1	5.53052	2.74320
2	0.51347	0.45510
3	1.44023	
4	3.27271	

Table C.1: Fit parameters for Equations C.6.

	P [mbar]
Cross A	1.610^{-1}
Cross B	1.010^{-5}
Cross C	4.010^{-7}

Table C.2: Typical pressures P measured along the RFQ ion guides. Cross A housed the segmented RFQ. Cross B was just downstream of the μRFQ. The mass filter lay between Cross B and Cross C.

touches the same ellipse in phase space; to achieve this in SIMION simulations, a trajectory quality ("TQual") of at least 120 is required. For each mass 3000 ions were generated.

In the damped case, the damping in the segmented RFQ and the μRFQ was modeled with hard-sphere collisions [131]. Typical pressures in the three sections of the ion guides are listed in Table C.2. I received ion distributions for 5000 ions which had begun at rest in the segmented RFQ and flown through the μRFQ from Stefan Schwarz [132]. The transmission from the segmented RFQ to the beginning of the mass filter is provided in Table C.3. The transmissions I calculated through the mass filter are normalized to Table C.3.

A	T [%]
28	59.7
45	80.7
85	83.5

Table C.3: Transmission from the segmented RFQ to the mass filter using hard-sphere collisions [132].

	r_0 [mm]	$U_{RF}(28)$ [V_{0p}]	$U_{RF}(45)$ [V_{0p}]	$U_{RF}(69)$ [V_{0p}]
Seg. RFQ	7.8	79.5	114.5	196.5
μRFQ	3.0	18.0	29.0	55.0
Mass Filter	6.2	77.0	125.0	235.0

Table C.4: The inter-rod distance r_0 and the RF amplitudes for A = 28, 45, 85 of the segmented RFQ, the μRFQ, and the mass filter. The electrostatic potentials are listed in Table C.5.

Seg. RFQ	DC1	DC2	DC3		
Potential [V]	60	43	38.5		
μRFQ	μplate1	μDC1	μDC2	μplate2	
Potential [V]	0	22.5	22.5	0	
Mass Filter	DC4	DC5	DC6	DC7	DC8
Potential [V]	20	10	10	0	-350
Acceleration	Acc1	Acc2	Acc3	Acc4	
Potential [kV]	-0.35	-3	-1.25	-5	

Table C.5: The electrostatic potentials for the electrodes in the ion guides. The RF amplitudes are listed in Table C.4.

C.2 Simulation parameters

The inter-rod spacing or inscribed radius and the RF amplitudes are given in Table C.4. The RF amplitudes for the μRFQ and the mass filter correspond to q = 0.706 for the masses used in this study; for the segmented RFQ, values used in experiment were taken. The voltages for the electrostatic potentials based on voltages typically used for the RFQ ion guides and the acceleration region directly downstream from the RFQ ion guides are summarized in Table C.5. Although the transmission and emittance were recorded immediately downstream of the DC8 electrode, the accelerating field penetrated DC8.

C.3 Transmission through the Mass Filter

The transmission T is plotted as a function of mass filter strength α in Figure C.3 for the three masses under both conditions. For ions with ideal initial conditions,

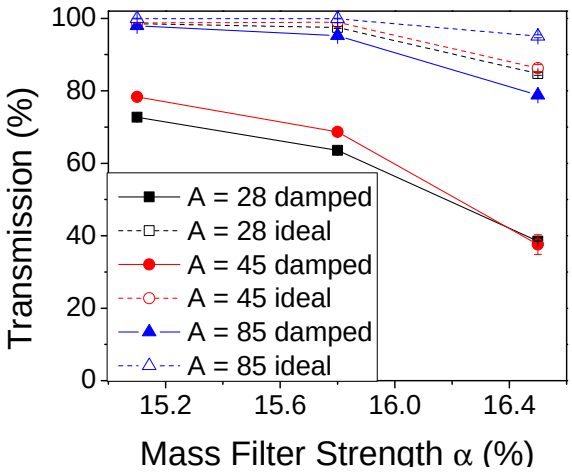

Figure C.3: Simulated transmission as a function of mass filter strength $\alpha = V_{DC}/U_{RF}$. Solid curves correspond to ions which underwent damping in a hard-sphere collision model. The dashed lines correspond to ions whose initial conditions were defined with the Mathieu equations.

the transmission is almost 100% until high mass resolving power is achieved; at $\alpha \approx \alpha_{max}$, the transmission drops to $\approx 85\%$ for A = 24, 45 and 95% for A = 85. In general lighter masses are more difficult to transport than heavier masses as a consequence of the Mathieu equations C.3. Similarly for the damped case, more A = 85 ions are transported than A = 28 or 45 ions. However, the difference in transmission between heavy and light masses is exacerbated relative to the ideal case. Transmission for A = 28 drops from 73% at $\alpha = 15.1\%$ to 39% at $\alpha = 16.5\%$ (normalized to the value in Table C.3). Damping leads to extraordinary losses especially for light ions. Most losses for ions with ideal or damped initial conditions occurred at the exit of the mass filter; the ions with damped initial conditions also frequently hit an electrode at the beginning of the mass filter. In general, the ion trajectories of the ions with damped initial conditions had larger motional amplitude as can be seen in Figure C.4

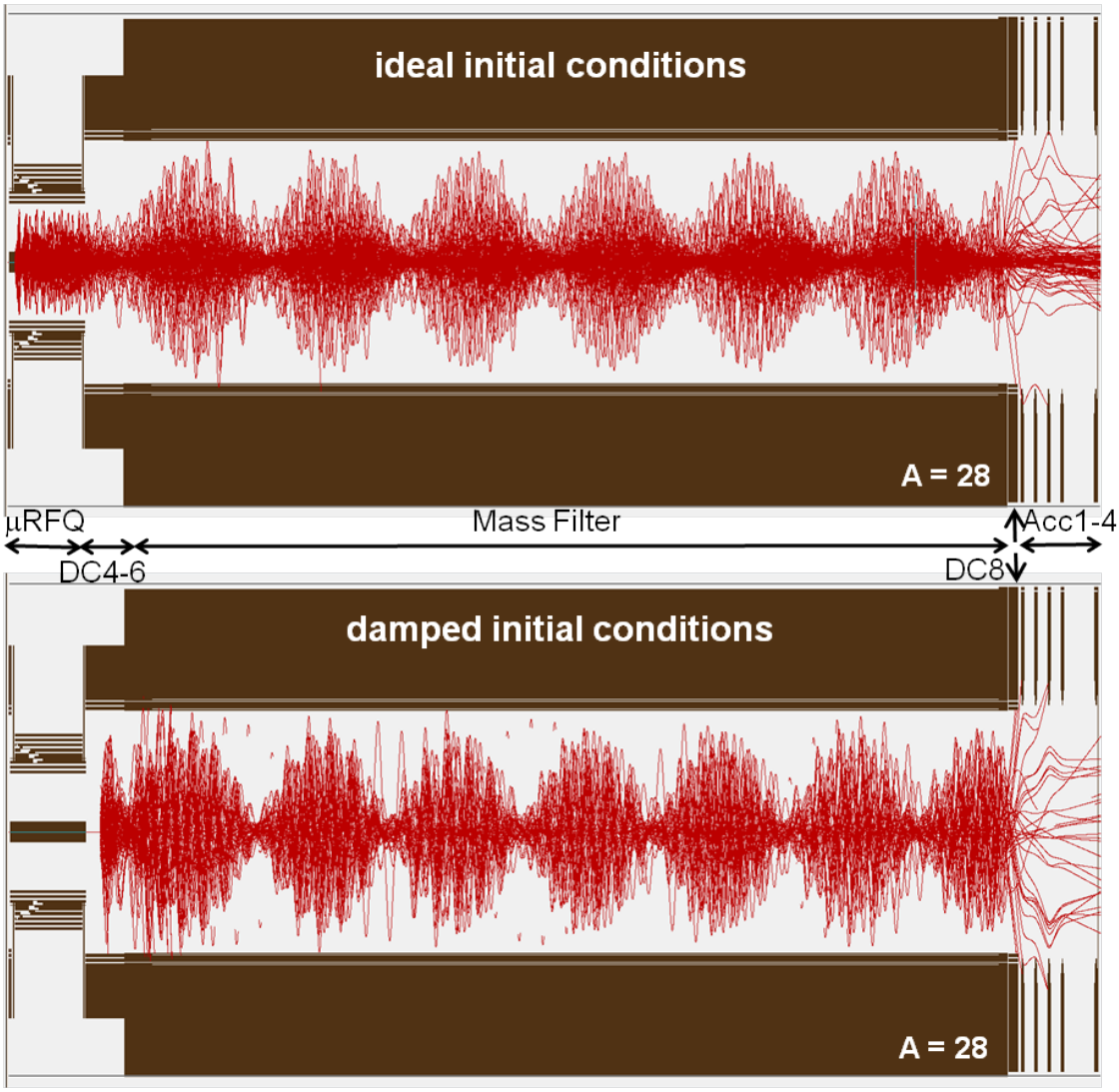

Figure C.4: Ion trajectories of A = 28 ions in the mass filter. Above "ideal" initial conditions; below damped initial conditions.

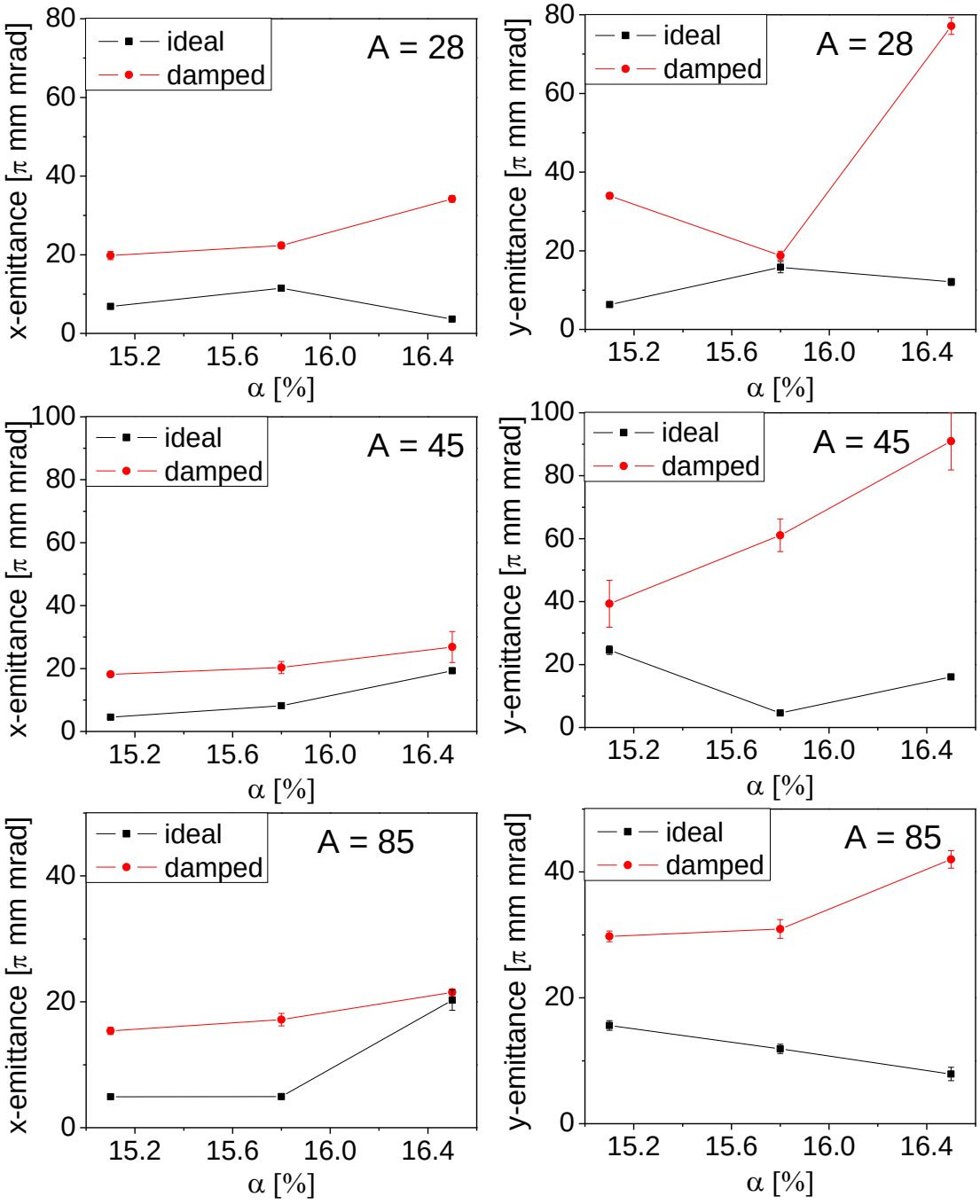

Figure C.5: Simulated x- and y-RMS emittances as a function of mass filter strength α. Emittance is normalized to 5 keV.

C.4 Emittance and Beam Profile of Mass-filtered Beams

One would expect that as α increases, the emittance grows. Figure C.5 plots the RMS emittance for the three masses as a function of α. The emittance of the damped ions steadily increases with α, except for the y-emittance of A = 28. The emittance of ions with ideal initial conditions does not follow the expected trend; moreover no general trend can be observed for the x- or y-emittance or for a particular mass in the ideal case. To some extent, this may be explained by the falling transmission. As α increases, the ion trajectories resemble more unstable trajectories. Ions lost were those with the largest motional amplitude and highest velocity. Given that the y-emittance is larger than the x-emittance for all cases indicates that the pseudo-potential (confining the ions in the radial direction) is elongated in the y-direction; that is, the restoring force is weaker in the y-direction. Examination of the beam area in phase space supports this hypothesis.

Figures C.6-C.11 show the x- and y-emittance for A = 28, 45, 85. The outline of the beam area in phase space is roughly the same between the ideal and damped cases although the latter has more diffuse edges. To first order, the orientation of the areas (the direction along which the area is longest) is 90° out of phase between the x and y phase-space plots as expected from the Mathieu equations. Ions are clustered in a small phase space area with fewer ions far from the origin; however, there is sufficient "scatter" to enhance the emittance. The size of the high density cluster and of the overall scatter is generally larger for the phase space in the y-direction. The enhancement in the y-direction is also visible in the beam profiles shown alongside the emittances in Figures C.6-C.11. The profile is always star-shaped, as was observed in experiment.

These simulations demonstrate that transmission through the mass filter falls off drastically for lighter masses as the mass filter strength α increases. The emittance

may increase because the ion trajectories more resemble unstable trajectories or fall if the ions farthest from the origin in phase space are lost. If the beam encounters heavy damping and is mass filtered at single mass resolving power, its emittance is larger than the acceptance of the beam cooler and buncher (41.5 π mm mrad at 5 keV [132]; even for ions with ideal initial conditions, high α causes the emittance for light ions to be larger than the acceptance of the cooler and buncher. Further simulations are needed to confirm the elongated pseudo-potential hypothesis.

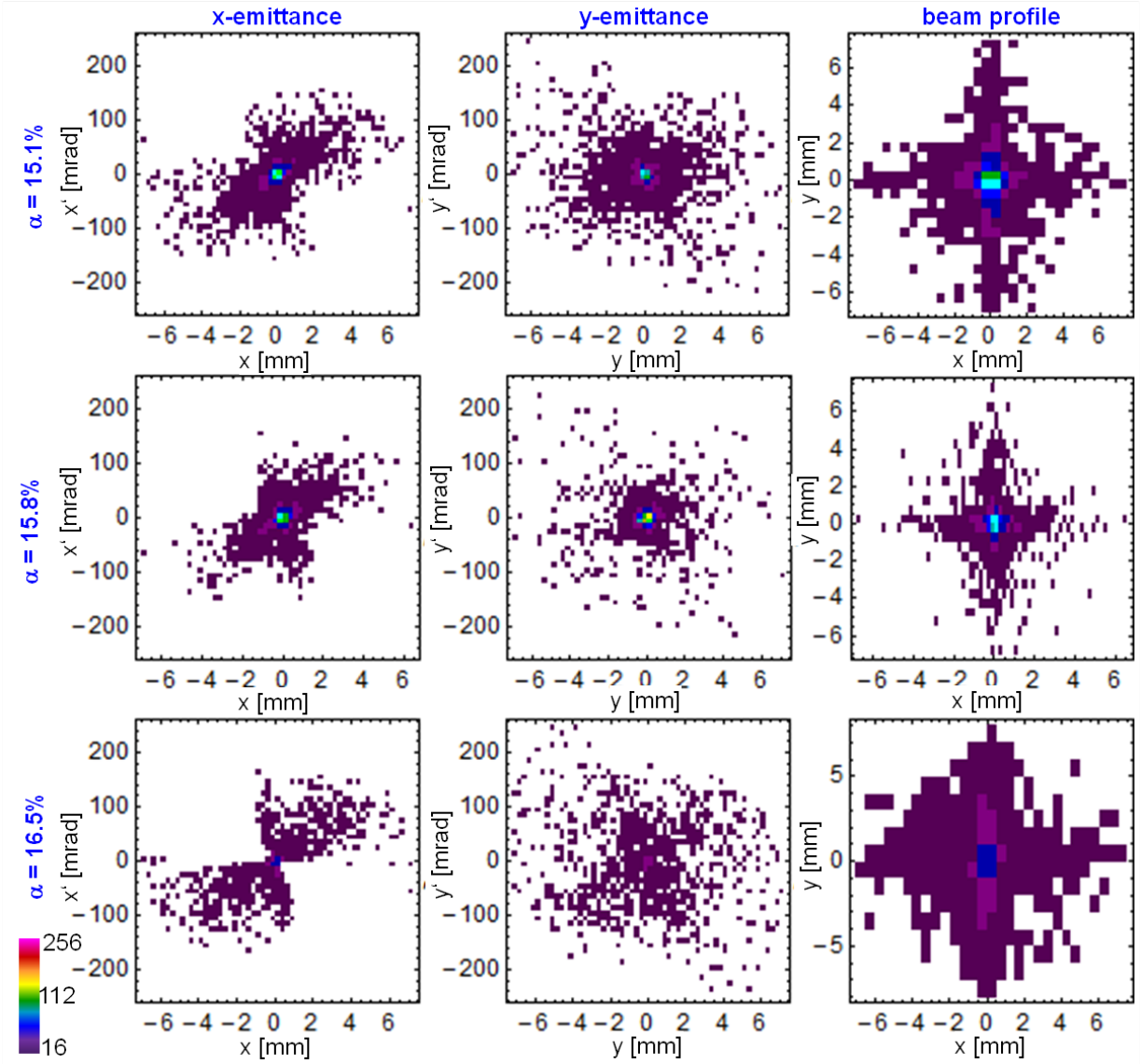

Figure C.6: Simulated x- and y-emittance and beam profile for A = 28 ions with damped initial conditions.

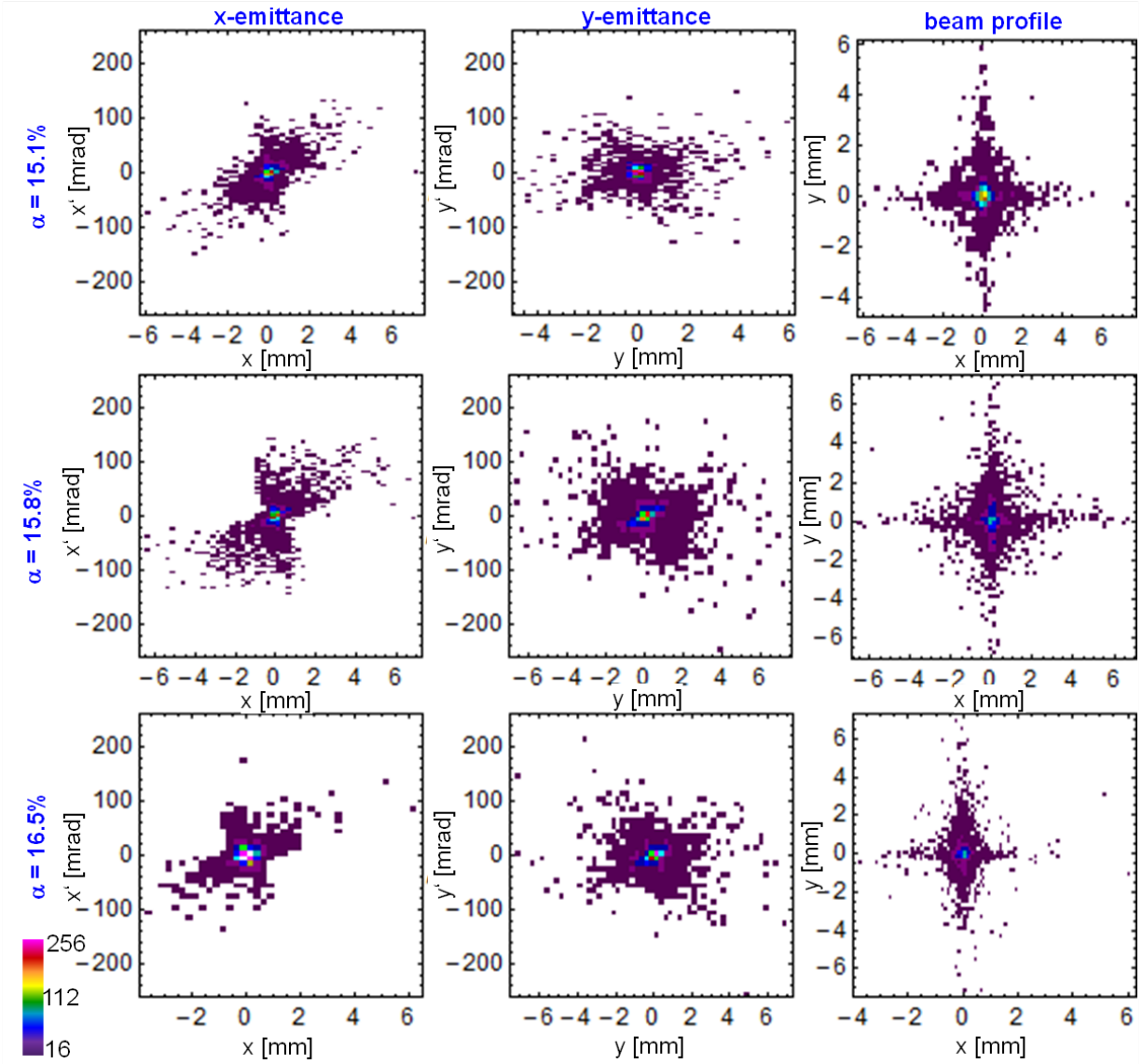

Figure C.7: Simulated x- and y-emittance and beam profile for A = 28 ions with "ideal" initial conditions.

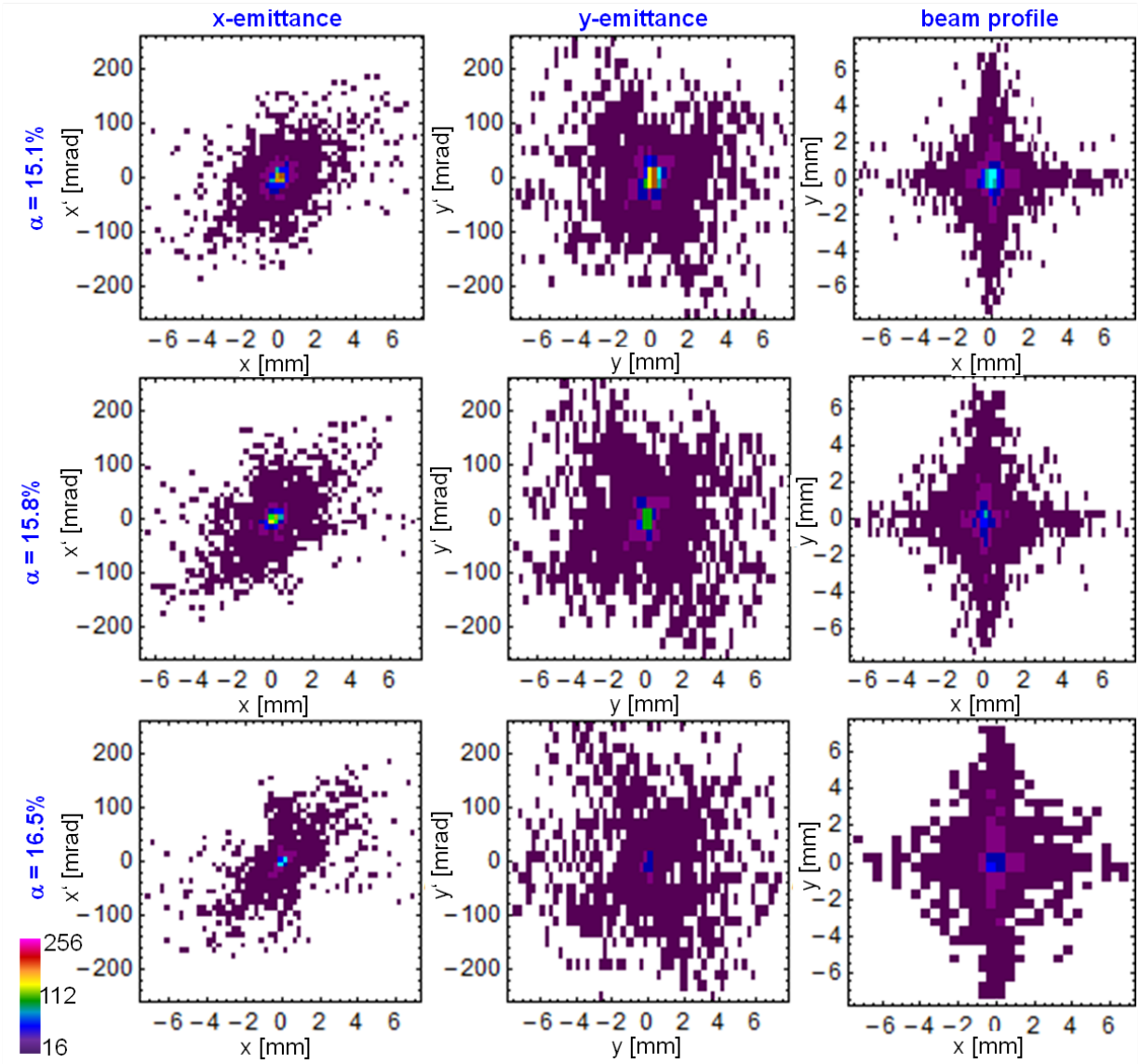

Figure C.8: Simulated x- and y-emittance and beam profile for A = 45 ions with damped initial conditions.

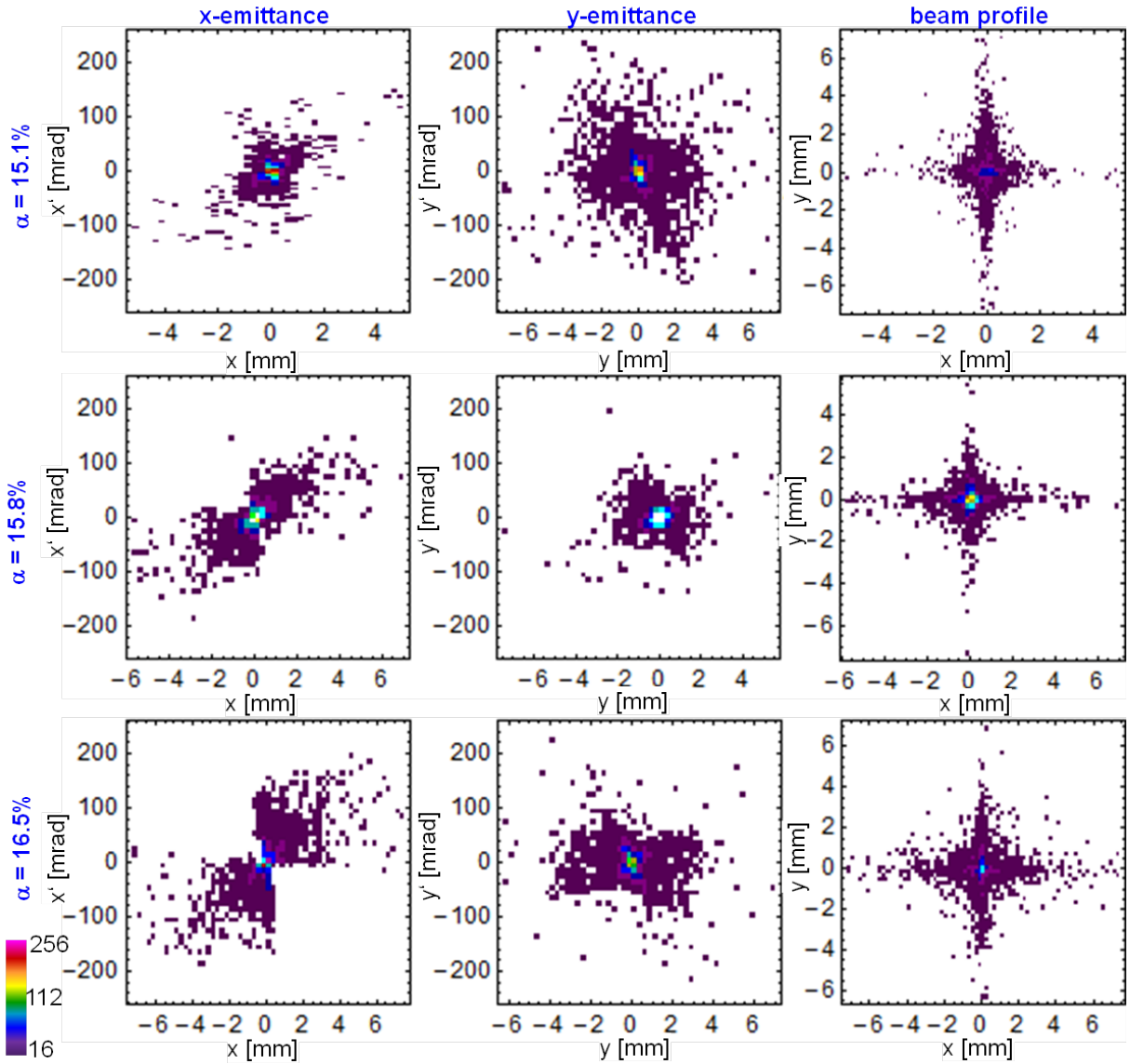

Figure C.9: Simulated x- and y-emittance and beam profile for A = 45 ions with "ideal" initial conditions.

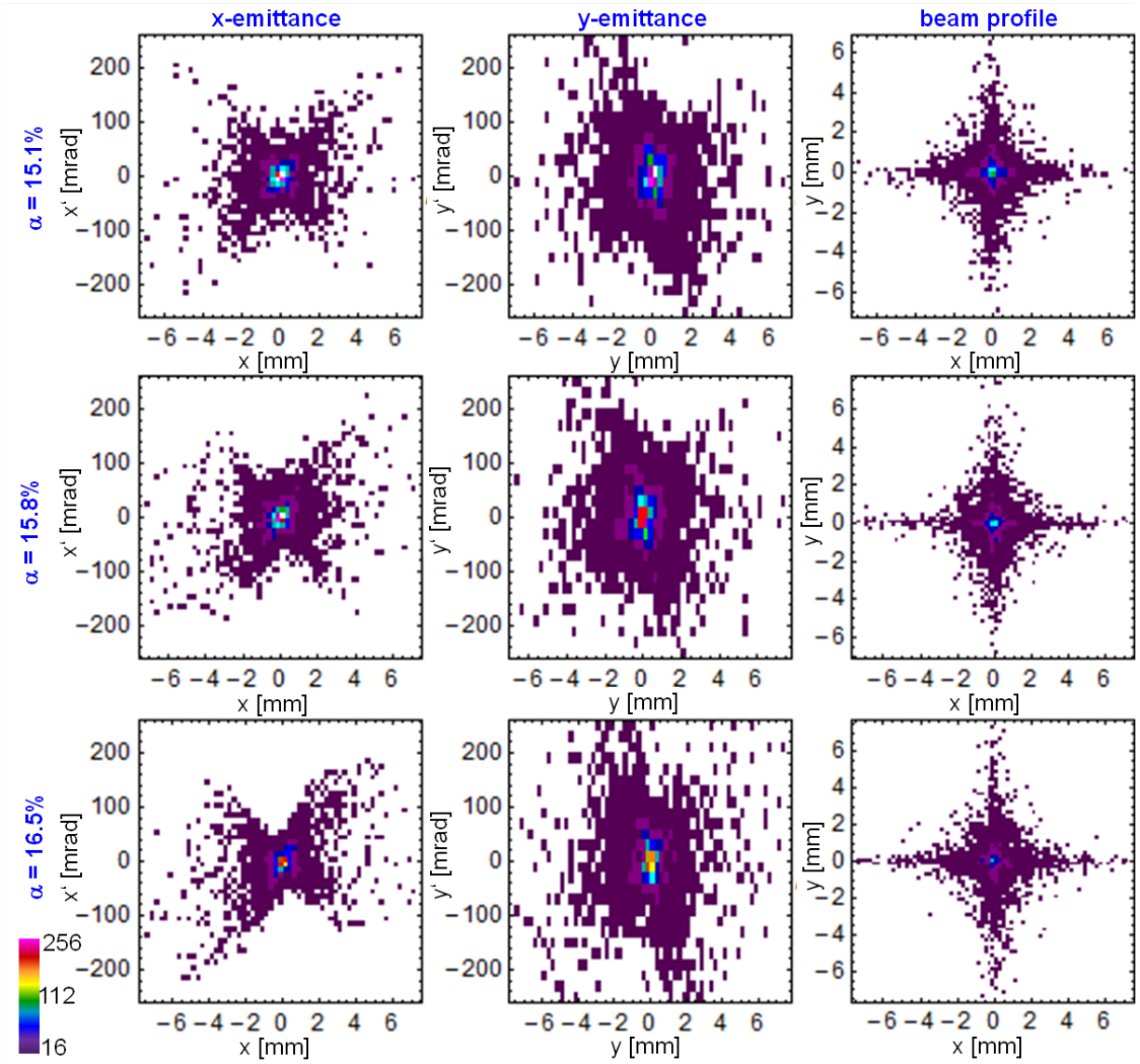

Figure C.10: Simulated x- and y-emittance and beam profile for A = 85 ions with damped initial conditions.

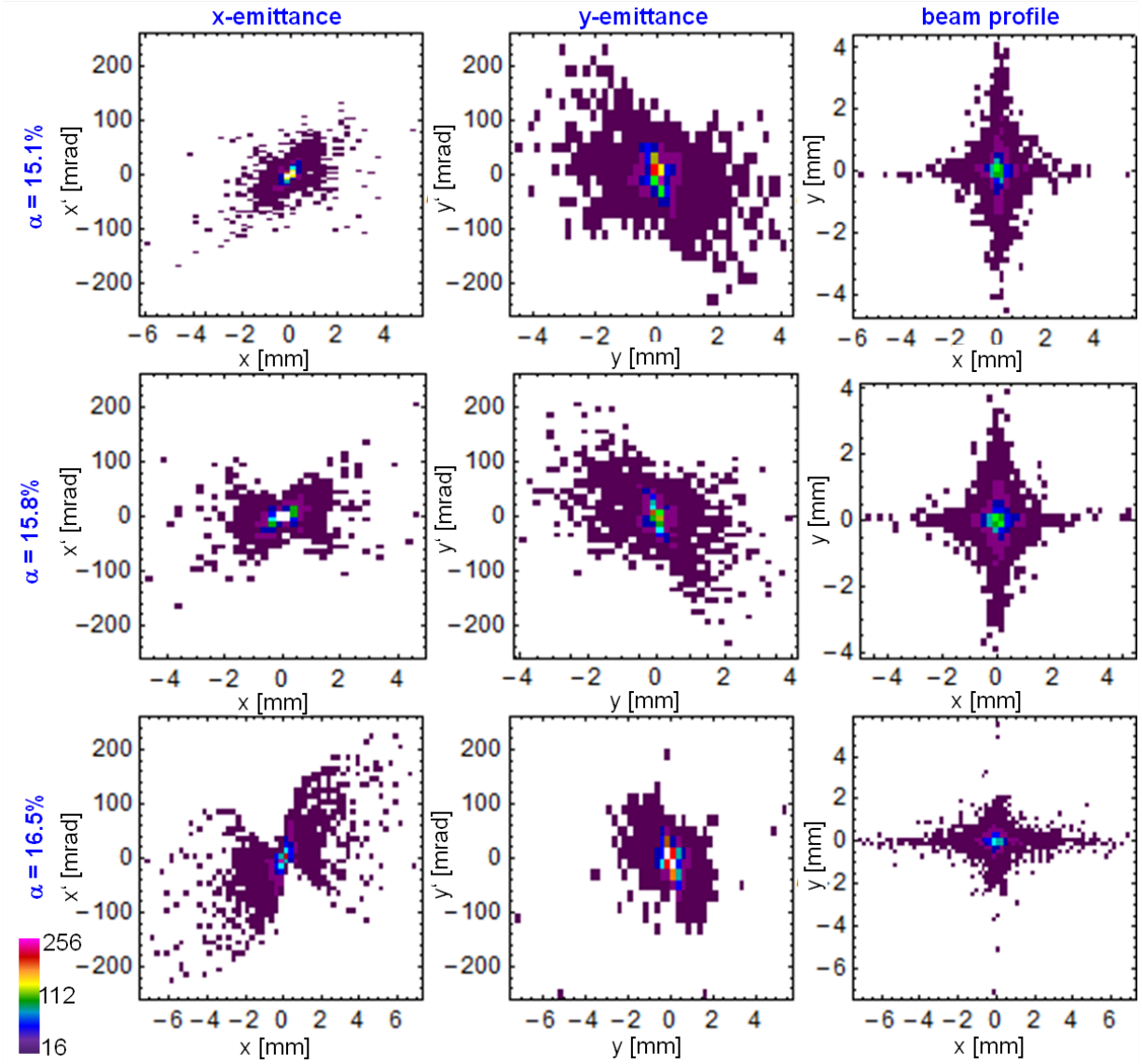

Figure C.11: Simulated x- and y-emittance and beam profile for A = 85 ions with "ideal" initial conditions.

BIBLIOGRAPHY

Bibliography

[1] K. Enders, E. Stachowska E, G. Marx, et al. Ground-state hyperfine-structure measurements of unstable Eu^+ isotopes in a Paul ion trap. *Phys. Rev. A*, 56:265, 1997.

[2] T. W. Hänsch and H. Walther. Laser spectroscopy and quantum optics. *Rev. Mod. Phys.*, 71:S242, 1999.

[3] H. Walther. Phase-transitions of stored laser-cooled ions. *Adv. At. Mol. Opt. Phys.*, 31:137, 1993.

[4] H. J. Kluge, K. Blaum, F. Herfurth, and W. Quint. Atomic and nuclear physics with stored particles in ion traps. *Phys. Scr. T*, 104:167, 2003.

[5] S. Schwarz, G. Bollen, D. Lawton, et al. A second-generation ion beam buncher and cooler. *Nucl. Instr. and Meth. B*, 204:474, 2003.

[6] K. Blaum. High-accuracy mass spectrometry of stored ions. *Phys. Rep.*, 425:1, 2006.

[7] R. S. Van Dyck, P. B. Schwinberg, and H. G. Dehmelt. New high-precision comparison of electron and positron g factors. *Phys. Rev. D*, 59:26, 1987.

[8] http://nobelprize.org/nobel_prizes/physics/laureates/1989/.

[9] G. Gabrielse. Antiproton mass measurements. *Int. J. Mass Spectrom.*, 251:273, 2006.

[10] K. Blaum, Yu. Novikov, and G. Werth. Penning traps as a versatile tool for precise experiments in fundamental physics. *Contem. Phys.*, 51:149, 2010.

[11] M. Beck, S. Coeck, V. Yu. Kozlov, et al. First detection and energy measurement of recoil ions following beta decay in a Penning trap with the WITCH experiment. *Eur. Phys. J. A*, 47:45, 2011.

[12] E. Haseltine. The 11 greatest unanswered questions of physics. *Discover Magazine*, 2:37, 2002.

[13] S. R. Elliot and P. Vogel. Double beta decay. *Annu. Rev. Nucl. Part. Sci.*, 52:115, 2002.

[14] J. C. Hardy and I. S. Towner. Superallowed $0^+ \rightarrow 0^+$ nuclear β decays: A new survey with precision tests of the conserved vector current hypothesis and the standard model. *Phys. Rev. C*, 79:055502, 2009.

[15] H. Savajols, B. Jurado, W. Mittig, et al. New mass measurements of the neutron drip-line. *Eur. Phys. J. A*, 25:23–26, 2005.

[16] E. Wigner. On the consequences of the symmetry of the nuclear hamiltonian on the spectroscopy of nuclei. *Phys. Rev.*, 51:106, 1937.

[17] P. Vogel. Pairing and symmetry energy in N = Z nuclei. *Nucl. Phys. A*, 662:148, 2000.

[18] P. Hansen, A. Jensen, and B. Jonson. Nuclear halos. *Annu. Rev. Nucl. Part. Sci.*, 45:591, 1995.

[19] P. G. Hansen and B. Jonson. The Neutron halo of extremely neutron-rich nuclei. *Europhys. Lett.*, 4:409, 1987.

[20] P. Schury, C. Bachelet, M. Block, et al. Precision mass measurements of rare isotopes near N = Z = 33 produced by fast beam fragmentation. *Phys. Rev. C*, 75:055801, 2007.

[21] J. Savory, P. Schury, C. Bachelet, et al. *rp* process and masses of $n \approx z \approx 34$ nuclides. *Phys. Rev. Lett.*, 102:132501, 2009.

[22] Kenneth S. Krane, editor. *Introductory Nuclear Physics*. John Wiley and Sons, 1988.

[23] W. S. C. Williams, editor. *Nuclear and Particle Physics*. Clarendon Press, 1991.

[24] K. Heyde, editor. *The Nuclear Shell-model*. Springer, 1994.

[25] D. Lunney, J. M. Pearson, and C. Thibault. Recent trends in the determination of nuclear masses. *Rev. Mod. Phys.*, 75:1021, 2003.

[26] E. P. Wigner. In W. O. Milligan, editor, *Proceedings of the Robert A. Welch Conferences on Chemical Research, Houston*. Robert Welch Foundation, Houston, 1957.

[27] S. Weinberg and S. B. Treiman. Electromagnetic corrections to isotopic spin conservation. *Phys. Rev.*, 116:465, 1959.

[28] J. Britz, A. Pape, and M. S. Antony. Coefficients of the isobaric mass equation and their correlations with various nuclear parameters. *At. Data and Nucl. Data Tables*, 69:125, 1998.

[29] K. Blaum, G. Audi, D. Beck, et al. Masses of ^{32}Ar and ^{33}Ar for fundamental tests. *Phys. Rev. Lett.*, 91:260801–1, 2003.

[30] R. Ringle, T. Sun, G. Bollen, et al. High-precision Penning trap mass measurements of ^{37}Ca, ^{38}Ca and their contributions to conserved vector current and isobaric mass multiplet equation. *Phys. Rev. C*, 75:055503, 2007.

[31] F. Herfurth, J. Dilling, A. Kellerbauer, et al. Breakdown of the isobaric multiplet mass equation at A = 33, T = 3/2. *Phys. Rev. Lett.*, 87:142501–1, 2001.

[32] C. Yazidjian, G. Audi, D. Beck, et al. Evidence for a breakdown of the isobaric multiplet mass equation: A study of the A = 35, T = 3/2 isospin quartet. *Phys. Rev. C*, 76:024308, 2007.

[33] S. Triambak, A. García, E. G.Adelberger, et al. Mass of the lowest T = 2 state in ^{32}s: A test of the isobaric multiplet mass equation. *Phys. Rev. C*, 73:054313, 2006.

[34] W. Shi, M. Redshaw, and E. G. Myers. Atomic masses of ^{32,33}S, ^{84,85}Kr, and ^{129,130}Xe with uncertainties $\leq$ 0.1 ppb. *Phys. Rev. A*, 72:022510, 2005.

[35] M. Smith, M. Brodeur, T. Brunner, et al. First Penning-trap mass measurement of the exotic halo nucleus ^{11}li. *Phys. Rev. Lett.*, 101:202501, 2008.

[36] G. Bollen, S. Becker, H. J. Kluge, et al. ISOLTRAP, a tandem Penning trap system for accurate on-line mass determination of short-lived isotopes. *Nucl. Instr. and Meth. A*, 368:675, 1996.

[37] V. S. Kolhinen, T. Eronen, J. Hakala, et al. Penning trap for isobaric mass separation at IGISOL. *Nucl. Instr. and Meth. B*, 204:502, 2003.

[38] S. Hofmann and G. Münzenberg. The discovery of the heaviest elements. *Rev. Mod. Phys.*, 72:733, 2000.

[39] M. Block, D. Ackermann, K. Blaum, et al. Direct mass measurements above uranium bridge the gap to the island of stability. *Nature*, 463:785, 2010.

[40] W. Mittig. The SPIRAL project at GANIL and future opportunities. *J. Phys. G*, 24:1331, 1998.

[41] H. Geissel, P. Armbruster, K. Behr, et al. The FSI projectile fragment separator (FRS): a versatile magnetic system for relativistic heavy ions. *Nucl. Instr. and Meth. B*, 70:286, 1992.

[42] T. Motobayash. RI beam factory project at RIKEN. *Nucl. Instr. and Meth. B*, 204:736, 2003.

[43] D. J. Morrissey, B. M. Sherrill, M. Steiner, et al. Commissioning of the A1900 projectile fragment separator. *Nucl. Instr. and Meth. B*, 204:90, 2003.

[44] G. Bollen, D. Davies, M. Facina, et al. Experiments with thermalized rare isotope beams from projectile fragmentation: A precision mass measurement of the superallowed β emitter ^{38}Ca. *Phys. Rev. Lett.*, 206:153501, 2005.

[45] P. H. Schury. *High Precision Mass Measurements near $N = Z = 33$.* PhD thesis, Michigan State University, 2007.

[46] K. Blaum. High-accuracy mass spectometry with stored ions. *Phys. Reports*, 425:1, 2006.

[47] G. Bollen, S. Becker, H. J. Kluge, et al. ISOLTRAP: a tandem Penning trap system for accurate on-line mass determination of short-lived isotopes. *Nucl. Instr. and Meth. A*, 368:675, 1996.

[48] G. Bollen, R. B. Moore, G. Savard, et al. The accuracy of heavy-ion mass measurements using time of flight-ion cyclotron-resonance in a Penning trap. *J. Appl. Phys.*, 68:4355, 1990.

[49] M. König, G. Bollen, H. J. Kluge, et al. Quadrupole excitation of stored ion motion at the true cyclotron frequency. *Int. J. Mass Spec.*, 142:95, 1995.

[50] G. Savard, S. Becker, G. Bollen, et al. A new cooling technique for heavy-ion cooling in a Penning trap. *Phys. Lett. A*, 158:247, 1991.

[51] A. G. Marshall, T. L. Wang, and T. L. Ricca. Tailored excitation for Fourier transform ion cyclotron resonance mass spectrometry. *J. Am. Chem. Soc.*, 107:7893, 1985.

[52] T. Sun. *High Precision Mass Measurement of ^{37}Ca and Developments for LEBIT.* PhD thesis, Michigan State University, 2006.

[53] L. Weissman, D. A. Davies, P. A. Lofy, and D. J. Morrissey. Stopping energetic heavy-ions in one-bar helium: broad incident momentum distribution. *Nucl. Instr. and Meth. A*, 531:416, 2004.

[54] L. Weissman, D. J. Morrissey, G. Bollen, et al. Conversion of 92 MeV/u ^{38}Ca/^{37}K projectile fragments into thermalized ion beams. *Nucl. Instr. and Meth. A*, 540:245, 2005.

[55] P. Schury, G. Bollen, M. Block, et al. Beam purificaton techniques for low energy rare isotope beams from a gas cell. *Hyperfine Interact.*, 173:165, 2006.

[56] T. Sun, S. Schwarz, G. Bollen, et al. Commissioning of the ion beam buncher and cooler for LEBIT. *Eur. Phys. J. A*, 25:61, 2005.

[57] R. Ringle, G. Bollen, D. Lawton, et al. The LEBIT 9.4 T Penning trap system. *Eur. Phys. J. A*, 25:59, 2005.

[58] R. Ringle, G. Bollen, A. Prinke, et al. The LEBIT 9.4 T Penning trap mass spectrometer. *Nucl. Instr. and Meth. A*, 604:536, 2009.

[59] Peter H. Dawson, editor. *Quadrupole Mass Spectrometry and its Applications.* Elsevier, 1995.

[60] Raymond E. March and John F. Todd. *Quadrupole Ion Trap Mass Spectrometry.* Wiley-Interscience, 2005.

[61] R. Ringle. *Design of LEBIT Penning trap and Mass Measurement of ^{38}Ca.* PhD thesis, Michigan State University, 2006.

[62] G. Gabrielse and J. Tan. Self-shielding superconducting solenoid systems. *J. Appl. Phys.*, 63:5143, 1988.

[63] R. Ringle, G. Bollen, A. Prinke, et al. A 'Lorentz' steerer for ion injection into a Penning trap. *Phys. Rev. C*, 263:38, 2007.

[64] N. R. Daly. Scintillation type mass spectrometer ion detector. *Rev. Sci. Instr.*, 31:264, 1960.

[65] G. Graff, H. Kalinowsky, and J. Traut. A direct determination of the proton-electron mass ratio. *J. Appl. Phys.*, 68:4355, 1990.

[66] L. S. Brown and G. Gabrielse. Geonium theory - physics of a single electron or ion in a Penning trap. *Rev. Mod. Phys.*, 58:233, 1986.

[67] L. S. Brown and G. Gabrielse. Precision spectroscopy of a charge particle in an imperfect Penning trap. *Phys. Rev. A*, 25:2423, 1982.

[68] G. Gabrielse. The true cyclotron frequency for particles and ions in a Penning trap. *Int. J. Mass Spectrom.*, 279:107, 2009.

[69] G. Bollen. Mass measurements of short-lived nuclides with ion traps. *Nucl. Phys. A*, 693:3, 2001.

[70] G. Bollen, H. J. Kluge, M. König, et al. Resolution of nuclear ground and isomeric states by a Penning trap mass-spectrometer. *Phys. Rev. C*, 46:R2140, 1992.

[71] W. M. Brubaker. An improved quadrupole mass analyzer. *Adv. Mass Spectrom.*, 4:293, 1968.

[72] J. Roithova, C. L. Ricketts, and D. Schroder. Reactions of the dications $c_7h_6^{2+}$, $c_7h_7^{2+}$, and $c_7h_8^{2+}$ with methane: Predominance of doubly charged intermediates. *Int. J. Mass Spectrom.*, 280:32, 2009.

[73] A. V. Jesseph, J. D. Fox, and G. F. Verbeck. Ion isolation and collision-induced dissociation in a 0.5 mm r_0 cylindrical ion trap. *Int. J. Mass Spectrom.*, 295:149, 2010.

[74] Y. M. Ibrahim, D. C. Prior, E. S. Baker, et al. Characterization of an ion mobility-multiplexed collision-induced dissociation-tandem time-of-flight mass spectrometry approach. *Int. J. Mass Spectrom.*, 293:34, 2010.

[75] J. Savory. *High Precision Mass Measurements of $N \approx Z \approx 34$ Nuclides for rp-process Simulations and Developments for the LEBIT Facility.* PhD thesis, Michigan State University, 2006.

[76] G. Audi, A. H. Wapstra, and C. Thibault. The AME2003 atomic mass evaluation (II). Tables, graphs and references. *Nucl. Phys.*, A729:337, 2003.

[77] T. Sun, S. Schwarz, G. Bollen, et al. Commisioning of the ion beam buncher and cooler for LEBIT. *Eur. Phys. J. A*, 25(S1):61, 2005.

[78] W. Heisenberg. Über den bau der atomkerne. *Z. Physik*, 77:1, 1932.

[79] E. M. Henley and C. E. Lacy. Simple model for corrections to isobaric multiplet mass equation. *Phys. Rev.*, page 1228, 1969.

[80] J. Jänecke. The quartic isobaric multiplet mass equation. *Nucl. Phys.*, A128:632, 1969.

[81] G. Bertsch and S. Kahana. T_z^3 term in isobaric multiplet equation. *Phys. Lett. B*, 33:193, 1970.

[82] W. Benenson and E. Kashy. Isobaric quartets in nuclei. *Rev. Mod. Phys.*, 51:527, 1979.

[83] W. E. Ormand. Mapping the proton drip line up to A=70. *Phys. Rev. C*, 55:2407, 1997.

[84] S. Ettenauer, M. Brodeur, T. Brunner, et al. Precision ground state mass of ^{12}Be and an isobaric multiplet mass equation (IMME) extrapolation for 2^+ and 0_2^+ states in the t = 2, a = 12 multiplet. *Phys. Rev. C*, 81:0243114, 2010.

[85] E. G. Adelberger, C. Ortiz, A. García, et al. Positron-neutrino correlation in the $0^+ \rightarrow 0^+$ decay of ^{32}Ar. *Phys. Rev. Lett.*, 83:1299, 1999.

[86] P. M. Endt. Supplement to energy levels of A = 21-44 nuclei (vii). *Nucl. Phys.*, A633:1, 1998.

[87] http://www.nndc.gov.

[88] M. Redshaw, J. McDaniel, and E. G. Myers. Dipole moment of ph^+ and the atomic masses of ^{28}si and ^{31}p by comparing cyclotron frequencies of two ions simultaneously trapped in a Penning trap. *Phys. Rev. Lett.*, 100:093002, 2008.

[89] S. Röttger, A. Paul, and U. Keyser. Prompt (n,γ)-spectrometry for the isotopic analysis of silicon crystals for the Avogadro project. *IEEE Trans. Instr. Meas.*, 46:560, 1997.

[90] A. Paul, S. Röttger, A. Zimbal, and U. Keyser. Prompt (n,γ) mass measurements for the AVOGARDO project. *Hyperfine Interact.*, 132:189, 2001.

[91] G. Audi and W. Meng, April 2011. private communication.

[92] W. A. Mayer, W. Henning, R. Holzwarth, et al. Mass excess and excited-states of neutron-rich silicon, phosphorus, and sulfur isotopes. *Z. Physik A*, 319:287, 1984.

[93] L. K. Fifield, C. L. Woods, R. A. Bark, et al. Masses and level schems of ^{33}Si and ^{34}Si. *Nucl. Phys.*, A440:531, 1985.

[94] D. R. Goosman, C. N. Davids, and D. E. Alburger. Accurate masses and β-decay schemes for ^{34}P and ^{32}Si. *Phys. Rev. C*, 8:1324, 1973.

[95] M. S. Antony, A. Huck, G. Klotz, et al. Mass measurements for the first T = 2 state in ^{32}S and ^{32}Si: Test of the imme. In *Proceedings of the International Conferences on Nuclear Physics, Berkeley, 1980*, volume 1. Lawrence Berkeley Laboratory, Berkeley, CA, 1980.

[96] J. F. Wilkerson, T. M. Mooney, R. E. Fauber, et al. Isospin-nonconserving particle decays in light nuclei. *Nucl. Phys.*, A549:223, 1992.

[97] C. Wrede, J. A. Clark, C. M. Deibel, et al. Toward precise $q_e c$ values for the superallowed $0^+ \rightarrow 0^+$ β decays of of T = 2 nuclides: The masses of ^{20}Na, ^{24}Al, ^{28}P, and ^{32}Cl. *Phys. Rev. C*, 81:055503, 2010.

[98] A. Kankainen, T. Eronen, D. Gorelov, et al. High-precision mass measurement of ^{31}S with the double Penning trap JYFLTRAP improves the mass value for ^{32}Cl. *Phys. Rev. C*, 82:052501R, 2010.

[99] M. Bhattacharya, D. Melconian, A. Komives, et al. ft value of teh $0^+ \rightarrow 0^+$ β^+ decay of ^{32}Ar: A measurement of isospin symmetry breaking in a superallowed decay. *Phys. Rev. C*, 77:065503, 2008.

[100] H. D. Choi, R. B. Firestone, R. M. Lindstrom, et al. Database of prompt gamma rays from slow neutron capture for elemental analysis. database STI/PUB/1263, IAEA, 2007. http://www-nds.iaea.org/reports-new/tecdocs/.

[101] A. Signoracci and B. A. Brown. Effects of isospin mixing in the A = 32 quintet. *ArXiv e-prints*, 1012.2402, 2010. http://adsabs.harvard.edu/abs/2010arXiv1012.2402S.

[102] L. Chen, T. C. L. Wang, T. L. Ricca, et al. Phase-modulated stored waveform inverse Fourier transform excitation for trapped ion mass spectrometry. *Anal. Chem.*, 59:449, 1987.

[103] S. Guan. General phase modulation method for stored waveform inverse Fourier transform excitation for Fourier transform ion cyclotron resonance mass spectrometry. *J. Chem. Phys.*, 91:775, 1989.

[104] S. Guan. Optimal phase modulation in stored waveform inverse Fourier transform excitation for Fourier transform mass spectroscopy. i. basic algorithm. *J. Chem. Phys.*, 92:5841, 1990.

[105] S. Guan. Optimal phase modulation in stored waveforn inverse Fourier transform excitation for Fourier transform mass spectrometry. ii. magnitude spectrum smoothing. *J. Chem. Phys.*, 93:8442, 1990.

[106] A. G. Marshall, C. L. Hendrickson, and G. S. Jackson. Fourier transform ion cyclotron resonance mass spectrometry: A primer. *Mass Spectrom. Rev.*, 17:1, 1998.

[107] S. Guan and A. G. Marshall. Stored waveform inverse Fourier transform (SWIFT) ion excitation in trapped-ion mass spectrometry: theory and applications. *Int. J. Mass Spec. Ion Processes*, 157/158:5, 1996.

[108] B. L. Tomlinson and H. D. W. Hill. Fourier synthesized excitation of nuclear magnetic resonance with application to homonuclear decoupling and solvent line suppression. *J. Chem. Phys.*, 59:1775, 1973.

[109] J. F. James. *A student's guide to Fourier transforms with applications in physics and engineering.* Cambridge Unversity Press, 1998.

[110] R. T. Birge. The calculation of errors by the method of least squares. *Phys. Rev.*, 40:207, 1932.

[111] V. S. Kolhinen, S. Kopecky, T. Eronen, et al. JYFLTRAP: a cylindrical Penning trap for isobaric beam purification at IGISOL. *Nucl. Instrum. Meth. A*, 528:776, 2004.

[112] A. A. Kwiatkowski, B. R. Barquest, G. Bollen, et al. Precision test of the isobaric multiplet mass equation for the A = 32, T = 2 quintet. *Phys. Rev. C*, 80:051302, 2009.

[113] G. Bollen, C. Campbell, S. Chouhan, et al. Manipulation of rare isotope beams - from high to low energies. *Nucl. Instrum. Meth. B*, 266:4442, 2008.

[114] M. A. Islam, T. J. Kennett, S. A. Kerr, and W. V. Prestwich. Self-consistent set of neutron separation energies. *Can. J. Phys.*, 58:168, 1980.

[115] M. A. Islam, T. J. Kennett, and W. V. Prestwich. Thermal neutron capture in silicon. *Phys. Rev. C*, 41:1272, 1990.

[116] S. Raman, E. T. Jurney, J. W. Starner, and J. E. Lynn. Thermal-neutron capture by silicon isotopes. *Phys. Rev. C*, 46:972, 1992.

[117] E. G. Adelberger and D. P. Balamuth. Electromagnetic decays of the lowest T = 2 state in ^{32}P. *Phys. Rev. Lett.*, 27:1597, 1971.

[118] S. Fortier, H. Laurent, J. M. Maison, et al. First T = 2 level in ^{32}P. *Phys. Rev. C*, 6:378, 1972.

[119] T. J. Kennett, W. V. Prestwich, and J. S. Tsai. Level structure and $e2$ strength from the ^{31}P(nγ)^{32}P reaction. *Phys. Rev. C*, 32:2148, 1985.

[120] S. Michaelsen, Ch. Winter, K. P. Lieb, et al. High-resolution spectroscopy of ^{32}P (ii). level density and primary transition strengths observed after thermal neutron capture in ^{31}P. *Nucl. Phys.*, A501:437, 1989.

[121] H. J. Fischbeck. Intensities of inner beta groups in ^{47}Ca and shapes of nonstatistical allowed outer groups in ^{47}Ca and ^{32}P. *Phys. Rev.*, 173:1078, 1968.

[122] P. Polak and L. Lindner. Liquid scintillation beta spectroscopy on 632si. *Radiochimica Acta*, 35:23, 1984.

[123] J. C. Overley, P. D. Parker, and D. A. Bromley. The energy calibration of tanden accelerators. *Nucl. Instr. and Methods*, 68:61, 1969.

[124] D. R. Goosman, K. W. Jones, E. K. Warburton, and D. E. Alburger. Masses and half-lives of ^{20}Na, ^{26}Al, ^{28}P, ^{32}Cl, and ^{36}K from the (p,n) reaction. *Phys. Rev. C*, 4:1800, 1971.

[125] C. Jeanperrin, L. H. Rosier, B. Ramstein, and E. I. Obiajunwa. Spectroscopy of ^{32}Cl nucleus via the ^{32}S(^{3}He,t)^{32}Cl reaction at 34.5 MeV. *Nucl. Phys.*, A503:77, 1989.

[126] T. Björnstad and the ISOLDE Collaboration. Study of the giant Gamow-Teller resonance in nuclear β-decay: The case of ^{32}Ar. *Nucl. Phys.*, A443:283, 1985.

[127] D. Schardt and K. Riisager. Beta-neutrino recoil braodening in β-delayed proton emission of ^{32}Ar and ^{33}Ar. *Z. Phys. A*, 345:265, 1993.

[128] Alan G. Marshall and Francis R. Verdun. *Fourier Transforms in NMR, Optical, and Mass Spectrometry.* Elsevier, 1990.

[129] J. W. Cooley and J. W. Tukey. An algorithm for the machine calculation of the complex Fourier series. *Math. Computation*, 19:297, 1965.

[130] J. F. James. *The Fast Fourier Transform.* Prentice-Hall, 1974.

[131] Stefan Schwarz. *Simulations for Ion Traps - Buffer Gas Cooling*, volume 749 of *Lect. Notes Phys.*, page 97. Springer-Verlag, 2008.

[132] S. Schwarz. Private Communication.